OPG's DEEP GEOLOGIC

REPOSITORY

FOR LOW & INTERMEDIATE LEVEL WASTE

Supporting Technical Report

Phase I Long-Term Cavern Stability

November 30, 2008

Prepared by:
Branko Damjanac,
Itasca Consulting Group, Inc.

OPG 00216-REP-01300-00005-R00

ITASCA Consulting Group, Inc.

111 Third Avenue South, Suite 450
Minneapolis, MN 55401 USA
phone: 1 612 371-4711 fax: 1 612 371-4717
email: hcitasca@hcitasca.com web: www.hcitasca.com

HCITASCA an company

OPG'S DEEP GEOLOGIC

REPOSITORY

FOR LOW & INTERMEDIATE LEVEL WASTE

Supporting Technical Report

Phase I Long-Term Cavern Stability

November 30, 2008

Prepared by:
Branko Damjanac,
Itasca Consulting Group, Inc.

OPG 00216-REP-01300-00005-R00

ITASCA Consulting Group, Inc.
111 Third Avenue South, Suite 450
Minneapolis, MN 55401 USA
phone: 1 612 371-4711 fax: 1 612 371-4717
email: hcitasca@hcitasca.com web: www.hcitasca.com
HCITASCA an company

DOCUMENT HISTORY

Title:	Phase I Long-Term Cavern Stability	
Subtitle:	OPG's Deep Geological Repository for Low and Intermediate Level Waste	
Client:	Ontario Power Generation Inc.	
Document Number:	OPG 00216-REP-01300-00005-R00	
Revision Number:	0	**Date:** November 30, 2008
Prepared by:	B. Damjanac	
Reviewed by:	T. Lam, D. McCreath, D. Martin, S. Usher	

Approved by: _____ **Accepted by:** _____

Robert Leech Mark Jensen

EXECUTIVE SUMMARY

Ontario Power Generation (OPG) has proposed the development of a deep geologic repository (DGR) for low- and intermediate-level waste (L&ILW) at the Western Waste Management Facility at the Bruce Site, located approximately 225 km west of Toronto, on the east shore of Lake Huron. The present site-specific geomechanical modelling study is a supporting technical study performed as a part of the Geosynthesis work program. This study aims to demonstrate DGR integrity and the long-term stability at a timeframe of 100,000 years.

The site-specific geomechanical modelling studies will be used to evaluate whether the proposed layout and geometry satisfy stability and safety requirements. The effects of different loading conditions expected during a timeframe of 100,000 years on repository performance, including the overall stability of the caverns, damage and deformation of the surrounding rock mass, are analyzed. The results of the cavern stability analysis due to long-term rock strength degradation and gas pressure inside the caverns, and during seismic ground shaking and glacial loading, are presented in this report. At this stage, while the site characterization investigations are ongoing, the analysis utilizes relevant available data on material properties and in-situ stress conditions. The analysis primarily was based on the mechanical properties determined from laboratory testing of samples retrieved from the Phase I deep exploratory boreholes, DGR1 and DGR2. Considering the uncertainty of some of the data, sensitivity analyses with respect to selected parameters are conducted to investigate the effect of their variability, within reasonable ranges, on repository performance.

The following are conservative assumptions used in the analysis.

- DGR cavern is considered to be unsupported with no backfilling.
- All waste packages are excluded from the analysis.
- Data from static fatigue tests of Lac du Bonnet granite (with relatively fast strength decay) were adopted for the long-term strength degradation prediction of the Cobourg limestone.
- No minimum threshold was set for the long-term Cobourg limestone strength. Thus, the rock strength eventually will reduce to zero with time.
- Arbitrary bedding planes of 1 m spacing are assumed in Cobourg limestone, intersected by the tunnel excavation.
- The vertical component of seismic ground motion is assumed to have the same intensity as horizontal components. Data for eastern North America indicate that the intensity of the vertical component of ground motion is 2/3 of the intensity of the horizontal component.
- Only 0.3% of the critical damping was used in the dynamic simulations of seismic ground shaking. Typical material damping in rocks is in the range between 2% and 5%.

The analysis was carried out using the numerical code UDEC, in which the Voronoi block model simulates the micro-cracking and time-dependent behaviour of the rocks. The preliminary long-term stability analysis undertaken in the present study is limited, but it provides an overall assessment of the effects of the considered loading scenarios within a 100,000 year time frame.

The results indicate, in the most conservative assumption based on the Lac du Bonnet static fatigue data and the zero long-term strength of Cobourg limestone, that damage due to time-dependent strength degradation propagates, at most, to 6 m above the cavern crown, while the greatest extent of damage in the walls is about 4 m. Under static conditions, the damage results in rockfall and breakouts of 2.5 m, at most, from the cavern boundary. Sensitivity of model predictions to the assumption of long-term rock strength was investigated by assuming the long-term strength of Cobourg limestone to be 0.4 UCS. The extent of damage is reduced considerably in the crown and the floor (3.5 m from the cavern crown, with only a 0.5 m thick slab resulting in rockfall), and is almost completely absent in the cavern walls. If the Yucca Mountain tuff static-fatigue data are adopted in the analysis, the result shows only very limited damage in the crown and floor, with no damage in the walls and no rockfall at all.

The cavern stability and containment of gas are analyzed for three selected gas pressure histories for a timeframe of 100,000 years. Gas pressure inside the cavern, and gas and water pressures in surrounding rock, increase the extent of damage in the Cobourg limestone, but not drastically compared to the time-dependent strength degradation under dry conditions. Although horizontal fracture propagation along the bedding partings up to 16 m behind the cavern walls is expected, the gas, in all analyzed cases, will not generate hydrofractures that can result in its release into biosphere.

The effect of the two seismic event scenarios, which match the target Uniform Hazard Spectra (UHS) at a 10^{-5} annual probability, on the stability of caverns at OPG DGR is analyzed numerically. Because it was expected that the response of the excavation would depend on the magnitude and extent of damage of the surrounding rock mass, the analysis was carried out for two different initial states when the model is subjected to dynamic loading: 1) immediately after cavern excavation, and 2) 100,000 years after excavation, which is the final state of time-dependent strength degradation considered. The analyses have shown that the response of the excavations to two different seismic events is almost identical. The considered seismic ground motions do not produce any additional damage or rockfall if they occur immediately after excavation. However, after damage due to time-dependent strength degradation has accumulated in the surrounding rock mass, a possible seismic event would shake down most of the damaged rock mass from the cavern crown. For the analyzed conditions, the predicted breakout extends approximately 5.5 m above the cavern crown.

The effect of glacial loads on cavern stability was analyzed by simulating the history of vertical stress expected during the glacial event with a maximum pressure of 29.7 MPa. The analysis indicates that the caverns and the pillar between the caverns remain stable throughout the glacial cycle, although the glacial load causes fracturing throughout the pillar width. Sufficient confining stresses mobilize the frictional strength of the pillar core, which carries significant stresses despite being fractured. Further modelling is warranted to determine the pillar behaviour when subjected to multiple glacial loading cycles.

CONTENTS

Page

LIST OF FIGURES

Page

LIST OF TABLES

Page

1. INTRODUCTION

Ontario Power Generation (OPG) is planning the development of a deep geologic repository (DGR) for low- and intermediate-level waste (L&ILW) at the Western Waste Management Facility at the Bruce Site, located approximately 225 km west of Toronto, on the east shore of Lake Huron. The present site-specific geomechanical modelling study is a part of the DGR geosynthesis work that is to provide the overall integration of all geoscientific project data and the development of a descriptive site geosphere model consistent with all the acquired data and information necessary for preparation of the DGR Environmental Assessment and the application for construction licenses (Intera, 2006). This study aims to demonstrate DGR integrity and the long-term stability during a timeframe of 100,000 years and beyond.

The site-specific geomechanical modelling studies will be used to evaluate whether the proposed layout and geometry satisfy stability and safety requirements. The effects of different loading conditions expected during a timeframe of 100,000 years on repository performance, including the overall stability of the caverns, damage and deformation of the surrounding rock mass, will be analyzed. At this stage, while the site characterization investigations are ongoing, the analysis utilizes relevant data on material properties and in-situ stress conditions. Considering the uncertainty of some of the data used in geomechanical modeling, sensitivity analyses with respect to selected parameters will be conducted to investigate the effect of their variability, within reasonable ranges, on repository performance.

The results of the cavern stability analysis due to long-term rock strength degradation (Section 4.1) and gas pressure inside the caverns (Section 4.2), and during seismic ground shaking (Section 4.3) and glacial loading (Section 4.4), carried out as a part of site-specific geomechanical numerical modelling and analysis (Geoscientific Studies for Deep Geological Repository — Geomechanical Modelling)[1], are presented in this report.

1. *Other site-specific numerical models, besides the geomechanical model, are the hydrogeologic and geochemical models*

2. MODEL DESCRIPTION

The cavern stability analyses were carried out using the commercially available numerical code *UDEC*, Version 4.00 (Itasca, 2004). *UDEC* is a two-dimensional distinct element code that can simulate the mechanical interaction of deformable polygonal blocks. The code is used widely and validated in the mining, petroleum, civil and nuclear waste industries for the simulation of deformation, heat transfer and fluid transport in rock masses.

2.1 Geometry and Boundary Conditions for Static Analyses

The typical geometry of the analyzed model for static calculations is shown in Figure 1. (Elevations in the figure are shown as depths and, therefore, are positive values.) The model geometry and boundary conditions for dynamic analysis are discussed in Section 4.3.2. The bottom of the cavern is at 683 m below the ground surface. The cavern is located in the high-strength upper Cobourg Formation, which could provide a competent roof for the cavern. The cavern design is based on Hatch (2007). The caverns are of rectangular shape. The low-level waste, LLW, will be emplaced in 8.1 m × 7.5 m caverns. The intermediate-level waste, ILW, will be emplaced in 8.1 m × 6.6 m caverns. Only the larger caverns for LLW are analyzed herein. The cavern lengths (90 m for ILW and 120 m for LLW), compared to characteristic dimensions in the cross-section, justify the use of two-dimensional approximation for the analysis. (When one dimension of an underground excavation is much greater than the other two, as, for example, in case of tunnels, the deformation field, which is a plane strain in the cross-sectional plane of the excavation, is two-dimensional.) The width of the pillar between the caverns (or cavern spacing) is 16 m. The model uses the symmetry plane between the caverns (Figure 1). Consequently, only one cavern is included in the model that extends laterally between two symmetry planes located halfway between the analyzed cavern and neighbouring caverns on the left and right. Although only one cavern is included explicitly, the model, with proper boundary conditions, represents typical conditions in the middle of the repository accurately.

The model does not extend vertically to the ground surface. It includes the total thickness of the Cobourg Formation, where the repository is located, plus the 30 m thickness of the overlying shales and the 30-m thickness of the underlying Sherman Fall Formation. The mechanical effect of the truncated portion of the rock mass above the top model boundary is represented as a dead weight, or stress boundary condition, and calculated conservatively assuming the saturated density of the entire column of rock to be 2700 kg/m^3. (The averages of the density measurements on a number of samples, as discussed in Section 3.1, are slightly less than 2700 kg/m^3.) The bottom of the model is fixed in the vertical direction. The vertical boundaries (along the symmetry planes) are fixed horizontally, but left free in the vertical direction.

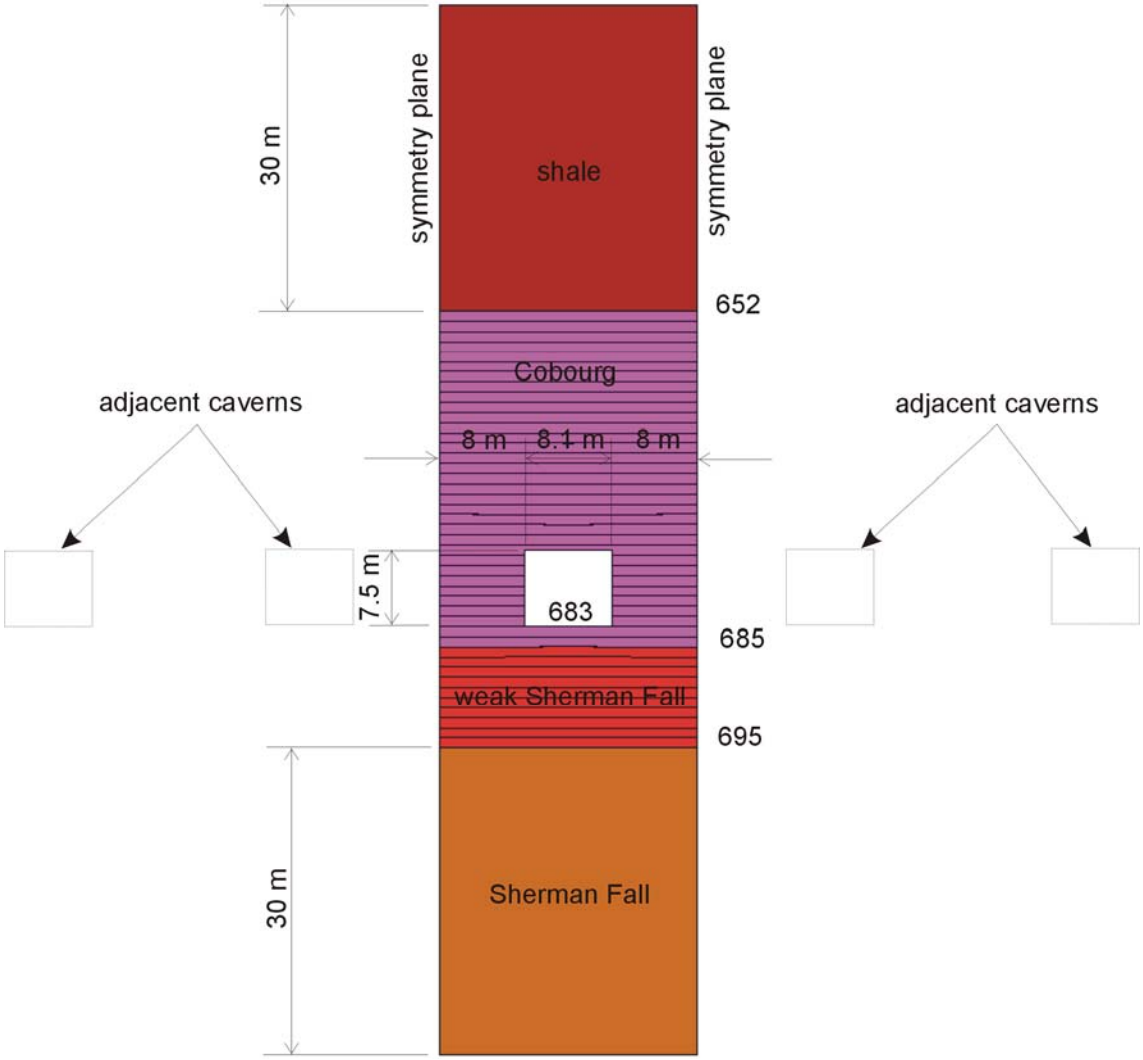

Figure 1. Geometry of the Model

The initial vertical stress, σ_z, is the minor principal stress with a magnitude equal to the overburden weight:

$$\sigma_z = \rho g z \tag{1}$$

where ρ is the rock mass density, g is acceleration due to gravity, and z is the vertical coordinate in the coordinate system, with origin at the ground surface and the positive z-axis oriented upward. Assuming that the rock mass density is 2700 kg/m^3, the vertical stress at the level of the cavern is 18.3 MPa. The initial horizontal stress state is assumed to be isotropic with a magnitude two times greater than the magnitude of the vertical principal stress. Thus, the magnitude of the horizontal stress at the repository level is 36.7 MPa.

3. GEOLOGY AND MATERIAL PROPERTIES

Three main geological units, shown in Figure 1, are included in the cavern stability model: the Cobourg limestone, the overlying Upper Ordovician shales and the underlying Sherman Fall limestone. The repository is designed to be located in the generally competent and massive Cobourg limestone (Itasca Consulting Canada, 2007). The locations of the units were determined from two exploratory boreholes: DGR-1 and DGR-2. Rock core samples from DGR-1 and DGR-2 were tested for their geomechanical properties as well. CANMET Mining and Mineral Sciences Laboratories, Natural Resources Canada, conducted a number of mechanical tests on samples taken from different depths and rock units (Intera, 2007). The tests included the compressional P-wave velocity test, Brazilian tensile strength test, uniaxial compressive strength test and direct shear test on bedding planes observed in shales, Cobourg limestone and Sherman Fall limestone. As indicated in Figure 1, the bedding planes are included explicitly as discontinuities in the model in the limestone only. The shales and part of the lower Sherman Fall units, being relatively far from the excavation where inelastic deformation is not expected, are represented as an equivalent continuum rock mass. The effect of the discontinuities, including the bedding planes, in those units is accounted for through the reduction of mechanical properties (i.e., the stiffness and strength). A relatively weak (compared to the lower Sherman Fall and, particularly, the upper Cobourg limestone) layer of rock, identified between depths of 685 m and 695 m, could be a transition between Cobourg and Sherman Fall limestones. In Figure 1, that layer, which is about 3 m below the cavern floor, is denoted as "weak Sherman Fall". Irrespective of its name and categorization, the layer is assigned mechanical properties based on testing results of representative samples taken from DGR-2 borehole.

3.1 Results of Geomechanical Tests

The average densities of the samples taken from DGR-1 and DGR-2 (Tables A-1 and A-2 of Intera, 2007) are 2620 kg/m^3 and 2680 kg/m^3, respectively. Conservatively, as mentioned in Section 2.1, a rock mass density of 2700 kg/m^3 was assumed for all units throughout the profile.

The strength and stiffness of the rock mass units in the model are determined from the uniaxial strength-test results listed in Table A-6 from Intera (2007). Table A-5 from Intera (2007) contains the results of the tests on samples taken from DGR-1. Those samples are not relevant for cavern stability, because they are taken at considerable distance from the cavern. The tests were carried out on the small-scale samples (75 mm in diameter) taken from different depths. The properties of different units were obtained by averaging the representative test results. Classification of the samples to different units represented in the numerical model (Figure 1) is shown in Table 1. The average values of the test results for Young's modulus, Poisson's ratio, unconfined compressive strength (UCS), crack initiation and crack damage stresses are listed in Table 2.

Table 1. Static elastic constants of DGR-2 specimens (taken from Table A-6 from Intera, 2007) with indication of their classification to different units shown in Figure 1

Specimen		Ultimate Uniaxial Strength	Transducers					Bonded Gauges				
Test	Depth		Peak Strain	E	Poisson's Ratio	Crack Damage Stress	Crack Initiation Stress	Peak Strain	E	Poisson's Ratio	Crack Damage Stress	Crack Initiation Stress
(No)	(m)	(MPa)	(%)	(GPa)	(v)	(σ_s=MPa)	(σ_d=MPa)	(%)	(GPa)	(v)	(σ_s=MPa)	(σ_d=MPa)
18	457.21	31.40	0.52	11.93	0.25	19.58	12.83	0.10	16.28	0.48	15.09	12.83
19	474.71	57.84	0.47	15.53	0.38	33.10	24.84	0.35	14.94	0.36	30.84	21.09
20	491.32	50.66	0.64	11.91	0.30	48.44	18.68	0.42	12.95	0.47	30.58	19.43
21	502.78	44.09	0.50	16.35	0.20	30.84	19.60	0.18	21.91	0.12	n/a	n/a
22	519.61	62.94	0.48	17.80	0.53	27.05	27.05	0.29	19.11	0.37	n/a	n/a
23	533.94	135.11	0.40	43.06	0.15	n/a	69.85	0.24	57.80	0.27	n/a	65.36
24	580.99	18.73	0.46	3.63	0.02	n/a	n/a	0.26	13.37	0.08	n/a	n/a
25	586.35	53.31	0.55	13.44	0.10	45.82	20.34	0.46	14.01	0.18	50.34	21.08
26	587.51	41.31	0.58	9.57	0.17	39.08	16.56	0.46	11.02	0.33	34.58	15.82
27	606.50	21.73	0.66	4.09	0.09	17.30	9.06	0.55	6.54	0.32	11.31	9.06
28	646.42	20.78	0.53	5.76	0.09	15.81	6.79	0.18	10.71	0.08	14.31	9.05
29	654.97	144.83	0.49	36.18	0.21	109.60	45.09	0.43	36.13	0.33	95.35	69.09
30	655.32	58.32	0.42	22.64	0.05	48.60	27.37	0.17	39.26	0.30	48.60	48.60
31	660.68	128.99	0.32	47.46	0.20	125.26	75.00	0.30	46.31	0.32	122.26	122.26
32	661.61	165.59	0.42	42.47	0.24	161.78	74.44	0.40	42.47	0.37	117.16	75.98
33	666.79	110.60	0.31	39.99	0.20	n/a	53.08	0.34	36.00	0.31	n/a	n/a
34	668.46	84.23	0.36	34.22	0.26	44.88	34.99	0.20	45.55	0.59	n/a	n/a
35	673.26	78.40	0.37	27.79	0.12	55.63	28.23	0.23	17.38	0.22	n/a	n/a
36	674.11	111.86	0.39	38.49	0.13	n/a	46.18	0.29	40.57	0.32	n/a	n/a
37	676.45	121.06	0.32	43.34	0.15	116.51	49.53	0.25	44.66	0.42	94.46	39.65
38	679.83	108.74	0.41	33.45	0.25	105.02	55.95	0.32	37.42	0.54	n/a	n/a
39	683.02	94.49	0.38	30.37	0.24	84.63	43.49	0.44	26.19	0.43	68.65	36.66
40	688.22	31.98	0.61	4.79	0.03	30.63	13.80	0.19	18.20	0.22	29.87	12.28
41	694.11	39.54	0.40	16.70	0.13	13.79	2.25	0.16	n/a	n/a	n/a	n/a
42	695.15	67.32	0.28	36.76	0.47	49.04	16.92	0.16	41.47	0.22	n/a	n/a
43	702.69	58.21	0.40	20.63	n/a	n/a	n/a	0.09	n/a	n/a	n/a	n/a
44	704.47	50.19	0.61	15.53	0.38	34.02	24.20	0.15	26.41	0.16	33.24	31.73
45	710.29	38.86	0.31	30.55	0.11	n/a	n/a	0.10	30.24	0.13	22.97	14.54
46	719.38	31.66	0.58	9.43	0.08	21.45	10.74	0.35	11.48	0.14	26.02	8.47
47	737.16	113.04	0.31	45.82	0.13	113.04	41.59	0.31	44.18	0.38	113.04	50.80

shales
Cobourg
weak Sherman Fall
Sherman Fall

Table 2. Average Test Results for the Model Units

	Elevation (m)	UCS (MPa)	E (GPa)	ν	σ_{cd} (MPa)	σ_{ci} (MPa)	σ_{cd}/UCS	σ_{ci}/UCS
shale	580.99	18.73	3.63	0.02				
		53.31	13.44	0.10	45.82	20.34	0.86	0.38
		41.31	9.57	0.17	39.08	16.56	0.95	0.40
		21.73	4.09	0.09	17.30	9.06	0.80	0.42
		20.78	5.76	0.09	15.81	6.79	0.76	0.33
	average	**31.17**	**7.30**	**0.09**	**29.50**	**13.19**	**0.84**	**0.38**
Cobourg	652	144.83	36.18	0.21	109.60	45.09	0.76	0.31
		58.32	22.64	0.05	48.60	27.37	0.83	0.47
		128.99	47.46	0.20	125.26	75.00	0.97	0.58
		165.59	42.47	0.24	161.78	74.44	0.98	0.45
		110.60	39.99	0.20		53.08		0.48
		84.23	34.22	0.26	44.88	34.99	0.53	0.42
		78.40	27.79	0.12	55.63	28.23	0.71	0.36
		111.86	38.49	0.13		46.18		0.41
		121.06	43.34	0.15	116.51	49.53	0.96	0.41
		108.74	33.45	0.25	105.02	55.95	0.97	0.51
		94.49	30.37	0.24	84.63	43.49	0.90	0.46
	average	**109.74**	**36.04**	**0.19**	**94.66**	**48.49**	**0.84**	**0.44**
weak Sherman Fall	685.6	31.98	4.79	0.03	30.63	13.80	0.96	0.43
		39.54	16.70	0.13	13.79	2.25	0.35	0.06
	average	**35.76**	**10.75**	**0.08**	**22.21**	**8.03**	**0.65**	**0.24**
Sherman Fall	695	67.32	36.76	0.47	49.04	16.92	0.73	0.25
		58.21	20.63					
		50.19	15.53	0.38	34.02	24.20	0.68	0.48
		38.86	30.55	0.11				
		31.66	9.43	0.08	21.45	10.74	0.68	0.34
	737.16	113.04	45.82	0.13	113.04	41.59	1.00	0.37
	average	**59.88**	**26.45**	**0.23**	**54.39**	**23.36**	**0.77**	**0.36**

Direct shear tests were conducted on the specimens containing the bedding planes. The first set of eight tests (Table A-8, Intera, 2007) did not contain any samples from the Cobourg limestone unit. Because the mechanical behaviour of bedding planes in the Cobourg limestone is of particular interest in this analysis, a direct shear test was conducted on three additional samples containing bedding planes from the Cobourg limestone (McCreath, 2007). The peak shear strength was measured for three samples in the original set of direct shear tests and for all three samples from the new set of direct shear tests. Because the peak shear strength could be measured only for one value of confining stress, the intact (peak) friction angle could not be obtained from the test results. The residual friction angles were calculated from the residual strength envelopes (e.g., Figures D-1 through D-8 in Intera, 2007). The average values of the residual friction coefficient and residual cohesion are calculated and listed in Table 3. Although the samples were taken from different geological units, the results are fairly consistent. The average friction angle of 31° ($\tan 31^\circ = 0.59$) is used in the analyses as both the intact and residual friction angle in the bedding planes. The residual cohesion is 0.57 MPa. The intact cohesion is estimated based on three additional direct shear tests in the Cobourg limestone.

Assuming that the intact friction angle is equal to the residual friction angle, the intact cohesion, c_p, is calculated from the Coulomb slip law, based on peak shear stress, τ_p, and the confining stress, σ_n:

$$c_p = \tau_p - \sigma_n \tan\phi \tag{2}$$

Table 3. Residual Friction Coefficients and Cohesions Calculated from the Direct Shear Tests (Intera, 2007; McCreath, 2007)

Depth (m)	tan ϕ	c (MPa)
613.37	0.57	0.16
616.59	0.58	0.20
646.72	0.47	0.46
692.00	0.28	0.30
697.86	1.51	1.29
702.23	0.48	0.31
705.86	0.42	1.57
708.57	0.68	0.40
664.94	0.36	0.47
673.06	0.83	0.33
684.00	0.36	0.75
average	**0.59**	**0.57**

Note: The results of the additional tests are shaded.

The calculated values for each of the three tests and the average value of 3.19 MPa are listed in Table 4. The intact tensile strength of the bedding planes was estimated to be 1/6 of cohesion, or 0.64 MPa.

Table 4. Peak Cohesion Calculated from the Direct Shear Tests (McCreath, 2007)

Depth (m)	Peak shear stress (MPa)	Normal stress (MPa)	ϕ (°)	c (MPa)
664.94	4.01	0.62	31.00	3.63
673.06	3.03	0.64	31.00	2.65
684.00	3.65	0.62	31.00	3.28
			average	3.19

The interpretation of the direct shear test results discussed in the previous paragraphs results in non-zero joint residual cohesion. However, sheared joints should have frictional strength only. Different interpretations of direct shear test results, in which residual cohesion is assumed to be zero, derivation of another set of bedding plane strength parameters and their effects on the model predictions are documented in Section 4.1.2.1.

The bedding plane normal stiffness is calculated from the condition that stiffness normal to the bedding planes of the Cobourg limestone rock mass, E_m, is 30 GPa. In the case of layered media, with uniform joint (bedding plane) spacing, the rock mass stiffness can be expressed in terms of intact rock stiffness, E, joint normal stiffness, k_n, and joint spacing, d, as follows:

$$\frac{1}{E_m} = \frac{1}{E} + \frac{1}{k_n d} \tag{3}$$

or

$$E_m = \frac{E k_n d}{k_n d + E} \tag{4}$$

From the previous expression, the joint normal stiffness is

$$k_n = \frac{E_m}{d\left(1 - \frac{E_m}{E}\right)} \tag{5}$$

For $E_m = 30$ GPa, the intact Cobourg Young's modulus, $E = 36$ GPa (Table 2), and an assumed bedding plane spacing of 1 m, the joint normal stiffness is calculated to be $k_n = 180$ GPa/m. The joint shear stiffness, k_s, is assumed to be 1/10 of the joint normal stiffness.

3.2 Material Models and Parameters

The shales and Sherman Fall limestone are represented as Mohr-Coulomb continuum materials. The mechanical properties used in this constitutive model are two rock-mass elastic properties (e.g., Young's modulus and Poisson's ratio) and rock mass strength properties (i.e., cohesion, friction angle and tensile strength). The mechanical properties obtained from laboratory tests on small samples, discussed in Section 3.1, have to be adjusted to be representative of the rock mass mechanical behaviour to account for scale effects and the effect of jointing of the rock mass. A standard approach in rock engineering to calculate rock mass properties uses the geological strength index (GSI) and Hoek-Brown failure criterion. The methodology implemented in the software program RocLab, Version 1.0 (RocScience, 2004), is used here to calculate rock mass mechanical properties for the shales and Sherman Fall limestone. Although detailed and proper rock mass classification is not available, the GSI was estimated (McCreath, 2007) for the shales and the Sherman Fall limestone to be 70 and 65, respectively. The results of the rock mass strength and deformability analysis are shown in Figure 2 and Figure 3. Values for m_i were selected as typical average values recommended for shale and limestone in RocLab (RocScience, 2004).

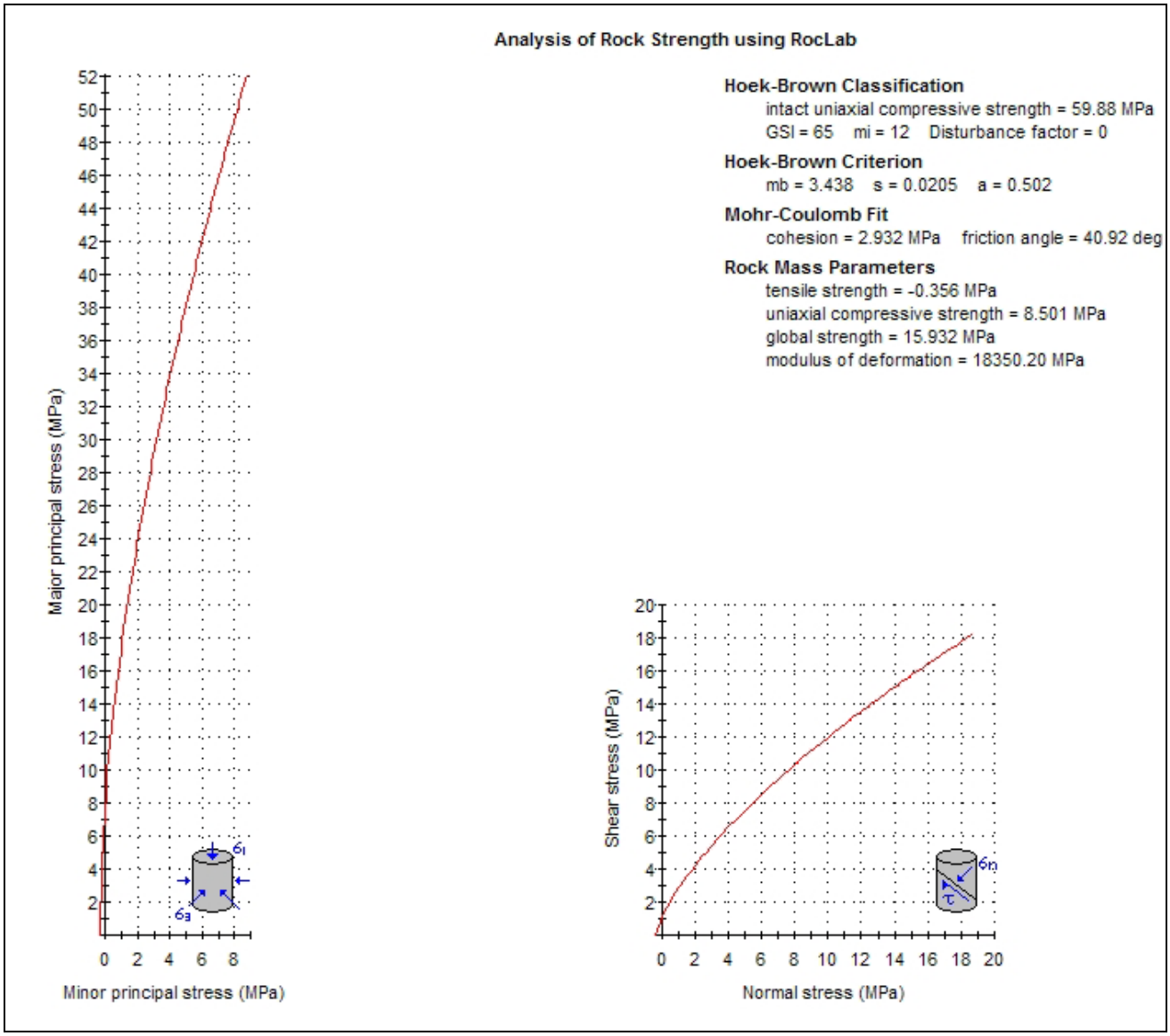

Figure 2. Rock Mass Strength for the Sherman Fall Limestone

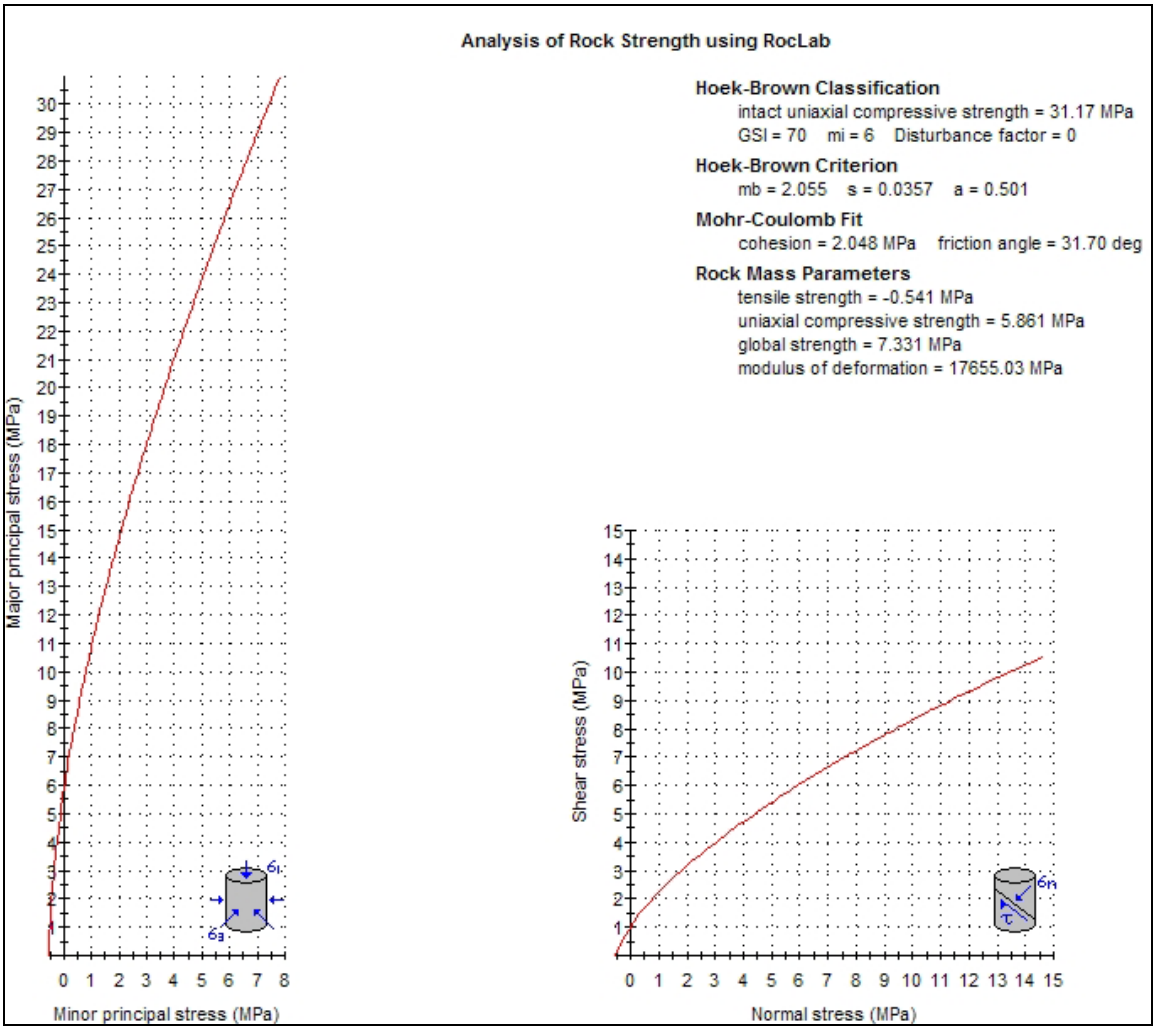

Figure 3. Rock Mass Strength for the Shales

The bedding planes, which are the main structures in the generally massive Cobourg limestone, are represented explicitly in the model in the Cobourg and weak Sherman Fall units (Figure 1). Therefore, and because there are no other large-scale joint sets, the mechanical properties for the Cobourg and weak Sherman Fall limestone, listed in Table 2, do not need to be reduced to account for the effect of rock mass jointing. However, the strengths of these two units were reduced to account for the size effect, because they were determined on the 75 mm diameter samples, while the characteristic dimension of massive rock is of the order of 1 m. Hoek and Brown (1980) developed an empirical relation for the influence of specimen size upon the strength of intact rock:

$$\left(\frac{\sigma_c}{\sigma_{cd_o}}\right) = \left(\frac{d_o}{d}\right)^{0.18} \tag{6}$$

where d_o is the specimen characteristic dimension for which strength, σ_{cd_o}, is measured, and d is the characteristic dimension for which rescaled strength, σ_c, is calculated. Rescaling the strengths of Cobourg limestone and weak Sherman Fall limestone (between 652 m and 695 m) from 75 mm to 200 mm, new strengths of 92 MPa and 30 MPa, respectively, are calculated. The reference value of 200 mm was used because the empirical data and Equation (6) are valid up to 200 mm. However, there should be no significant decrease in strength between 200 mm and 1 m.

Because only unconfined strength tests were conducted on the rock samples, the complete failure envelope could not be determined based on laboratory results. The empirical approach used to determine rock mass strength for the shales and Sherman Fall limestone provided an estimate of the Hoek-Brown failure envelope. (The friction angle is calculated by fitting the Mohr-Coloumb failure envelope to the Hoek-Brown failure envelope in the range of the confining stresses of interest.) On the other hand, the friction angle for the Cobourg limestone and the weak Sherman Fall limestone was assumed to be 45°. This assumption is probably conservative (i.e., underestimates the strength under confined conditions) for such a good quality rock mass.

The mechanical properties of the different rock units (on the small and rock-mass scales), as used in the cavern stability analysis, are listed in Table 5.

Table 5. Rock and rock mass properties used for the cavern stability analysis

Unit	ρ (kg/m^3)	E (GPa)	ν	K (GPa)	G (GPa)	UCS (MPa)	ϕ (°)	c (MPa)	T (MPa)*
shale	2700	7.30	0.09	2.97	3.35	31.17	45.00	6.46	
shale rock mass	2700	17.65	0.09	7.17	8.10		31.70	2.05	0.54
Cobourg	2700	36.04	0.19	19.38	15.14	92.16	45.00	19.09	
weak Sherman Fall	2700	10.74	0.08	4.26	4.97	30.08	45.00	6.23	
Sherman Fall	2700	26.45	0.23	16.33	10.75	59.88	45.00	12.40	
Sherman Fall rock mass	2700	18.35	0.23	11.33	7.46		40.92	2.93	0.36

** Although the tensile strength was measured in the Brazilian tests (Table A-7, Intera, 2007), those exact values were not used in the analyses. The tensile strength is estimated for the shales and Sherman Fall limestone based on the Hoek-Brown failure criterion. The tensile strength for the Cobourg limestone is approximated by the tensile strength of the Voronoi block approximation (Section 3.3).*

3.3 Voronoi Block Approximation of Cobourg Limestone

Voronoi block approximation is used for the representation of the Cobourg and weak Sherman Fall limestones. It is a micro-mechanical model in which the brittle rock is represented as an assembly of relatively small polygonal blocks. The blocks can be rigid or deformable, and if deformable, either elastic or elastic-plastic. The blocks interact with each other through the joints, which initially are elastic, when the stresses are relatively small. As the load in the joints increases, they can fail, either in tension or shear. Joint failure in tension is controlled by the joint tensile strength. The Coulomb slip criterion governs the onset of inelastic shear deformation, or slip of the joint. Joints between Voronoi blocks do not represent the actual internal structure of rocks. Instead, they are ubiquitous and randomly oriented at relatively short spacing, acting as possible locations and orientations of fractures within the rock. Failing of a joint in shear or tension represents fracturing of the rock mass. Fracturing initiates and evolves

as a function of rock mass strength and as dictated by stresses and forces in the rock mass. An example of the use of the Voronoi block approach for stability analysis of underground excavations at the Yucca Mountain Project, the U.S. program for high-level nuclear waste disposal, is described by Damjanac et al. (2007). The advantage of the Voronoi block approach is that it can simulate fracturing of a brittle rock mass, the formation of loose and unstable ground, and its rockfall. Continuum-based numerical models can be used to predict the redistribution of stresses, displacements and regions of inelastic deformation and damage, but they cannot predict rockfall. One small disadvantage of the Voronoi block approach is that micro-mechanical properties (of joints and blocks) are not measured directly in laboratories. Instead, they have to be determined indirectly through the calibration process, in which micro-mechanical properties are adjusted until the macro-mechanical behaviour measured in laboratories is matched by the response of the Voronoi block model in the numerical simulation of that laboratory experiment.

The model is discretized into Voronoi blocks in the region around the cavern where damage due to in-situ stresses and analyzed loads is expected. The average Voronoi block size (width) is selected to be 0.3 m. The ratio of the block size to the cavern span, which is $0.3/8.0 = 0.0375 \ll 1$, is sufficiently small that the block size, an artificial model parameter, does not affect the model results. Discretization of the model region into the Voronoi blocks as used in the analysis is illustrated in Figure 4. Discretization of the entire analyzed domain in the Voronoi blocks would result in a large (in terms of computer memory required for execution of the numerical model) and slow model. If the analyses had shown that damage extends to the boundary of the region discretized into Voronoi blocks, the analysis would have been repeated with a larger region discretized into the Voronoi blocks.

3.4 Voronoi Model Calibration

The Voronoi block model is calibrated to the mechanical properties of the Cobourg limestone and the weak Sherman Fall limestone. The calibration is conducted by simulating the laboratory experiments used to determine the macro properties of the rocks. The most important mechanical parameters that control stability of the underground excavation are unconfined compressive strength (UCS) and stiffness. The micro-mechanical parameters of the Voronoi block model are adjusted in order to match the stiffness and strength of the Cobourg limestone and weak Sherman Fall limestone (as listed in Table 5).

The following are the micro-mechanical parameters that need to be determined in the calibration process:

joint normal stiffness ..... k_n
joint shear stiffness ..... k_s
block Young's modulus ..... E
block Poisson's ratio ..... ν
joint peak cohesion ..... c_p
joint peak friction ..... ϕ_p
joint peak tensile strength ..... T_p
joint residual friction ..... ϕ_r

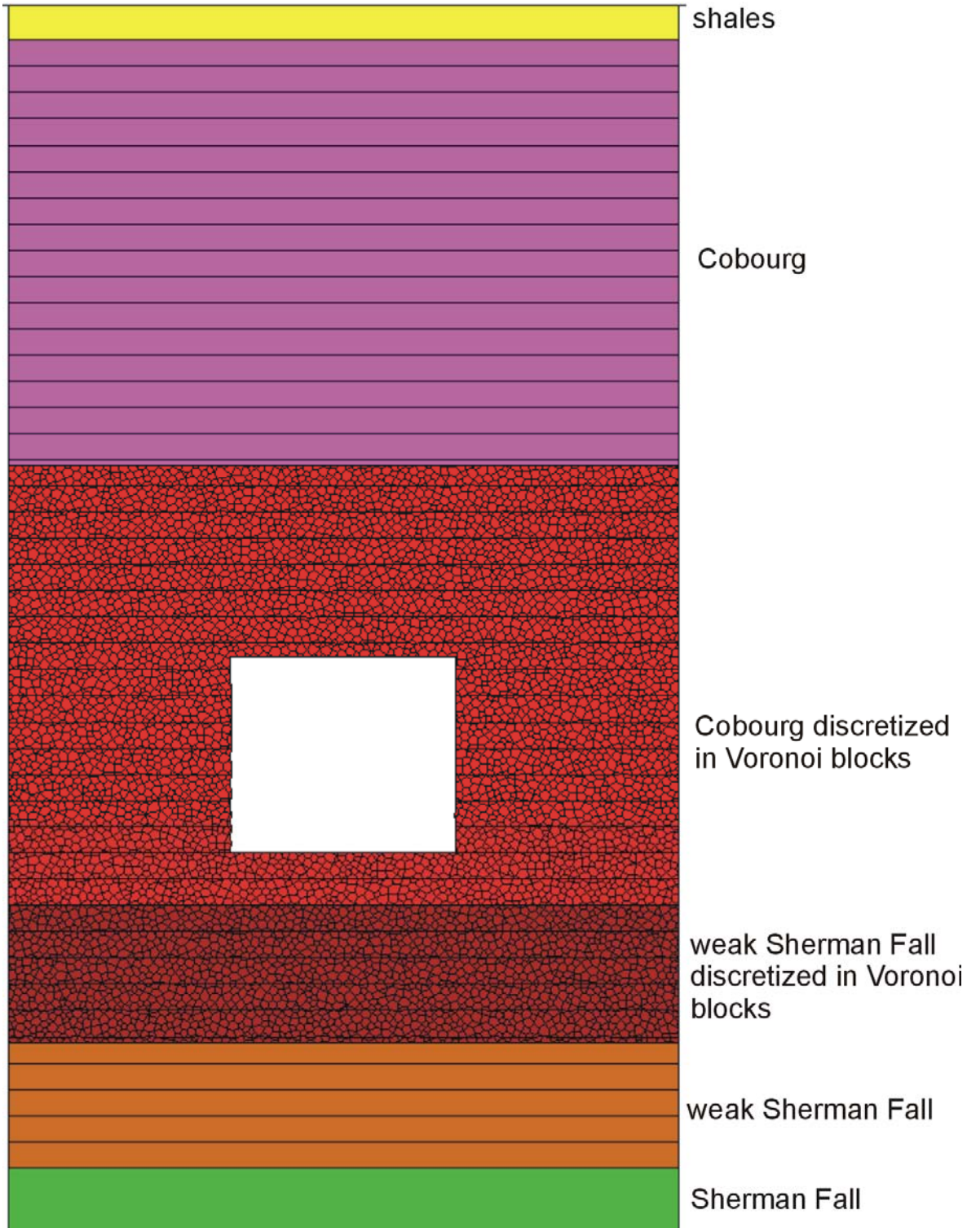

Note: Units are coloured differently than in Figure 1 because of the greater number of units included in this figure.

Figure 4. Discretization of the Region of the Model into Voronoi Blocks

Instead of block Young's modulus and Poisson's ratio, another two elastic constants can be used—such as bulk modulus, K, and shear modulus, G. The model parameters also include residual cohesion and tensile strength. In all of the analyses discussed here, both of those parameters were considered to be zero in order to simulate Cobourg limestone as a brittle material.

To match two macro elastic constants (e.g., Young's modulus and Poisson's ratio), and the macro failure strength envelope defined by three constants (e.g., cohesion, friction angle and tensile strength), the problem is underdetermined, because there are more micro-mechanical constants than constraints. For example, four micro-mechanical elastic constants need to be adjusted to match only two macro-mechanical elastic constants. The problem is resolved by assuming that the stiffness of the Voronoi blocks is much greater (>10) than the stiffness of the joints, meaning that the joints are the main contributors to the compliance of the model. The other extreme, when the joints are much stiffer than the blocks, is also analyzed, and the results of the two approximations are found to be quite similar. In the case of the calibration of micro-mechanical strength parameters, additional qualitative constraints were used to define the problem including mode of failure and its evolution as a function of confinement, and post-peak behaviour (e.g., post-peak softening strain and residual strength). It was observed in unconfined laboratory tests that the Cobourg limestone fails predominantly by axial splitting. Although the post-peak behaviour was not recorded during the experiments, this rock also exhibited a quite brittle response after failure (McCreath, 2007). Therefore, the micro-mechanical strength parameters used in the Voronoi block model were adjusted to result in a brittle sample failure.

The results of the numerical simulation of unconfined compression, direct tension and bi-axial compression tests (for 1 MPa and 3 MPa confinements) are shown in Figure 5 and Figure 6. The tests were carried out on 5 m edge square samples. Because perfectly frictionless boundary conditions were applied in the numerical tests on the loaded ends of the sample, it was not necessary to have a 2:1 height-to-width ratio for the tested samples. Axial stress-strain curves are shown in Figure 5 for each test, together with sample configuration and the displacement vector field in the final failure state. Red lines in the sample plots indicate the locations of micro fractures. The sample fails by axial splitting in the compression tests. The Young's modulus of 33.6 GPa, indicated in the figure, and the UCS of 91.7 MPa are in a good agreement with the target values of 36.04 GPa and 92.16 MPa, respectively, for the Cobourg limestone listed in Table 5. The post-peak behaviour in all three compression tests is brittle.

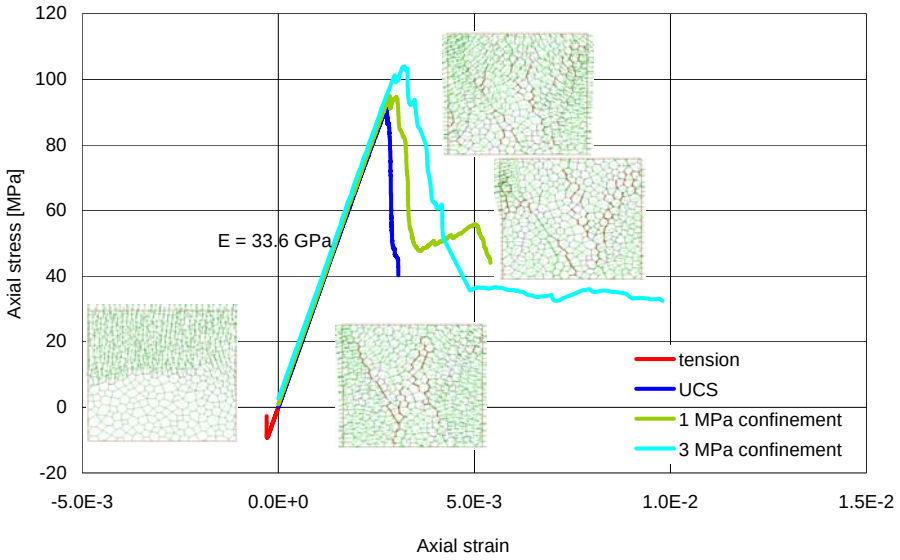

Figure 5. Axial response obtained from the numerical tests on calibrated Voronoi block model of Cobourg limestone (compression positive)

The volumetric strain as a function of the axial strain is shown in Figure 6. The Poisson's ratio and average dilation angles are indicated in the plot. The dilation angles vary as a function of confinement, being greatest for unconfined loading conditions.

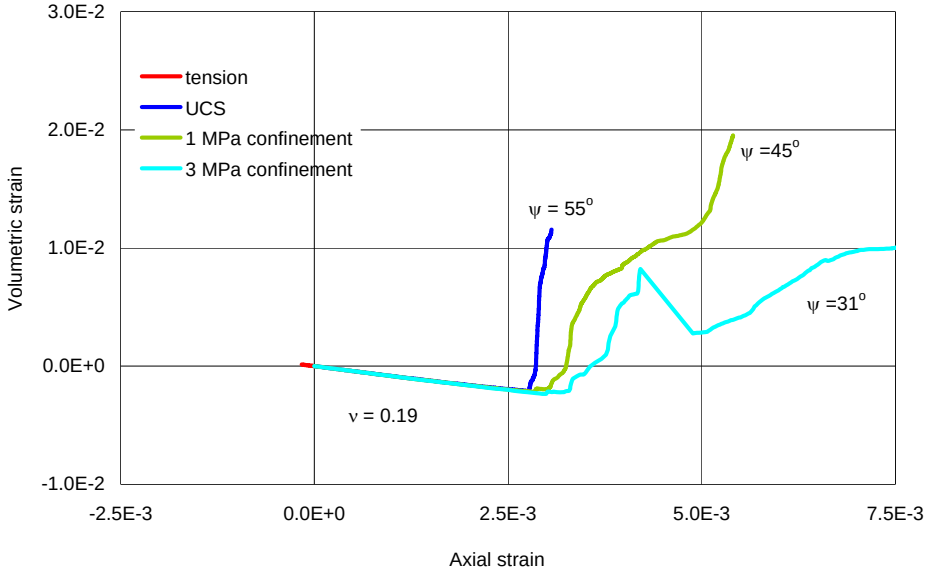

Figure 6. Volumetric response obtained from the numerical tests on the calibrated Voronoi block model of Cobourg limestone

The failure envelope in principal stress space of the Voronoi block model of the Cobourg limestone, constructed based on the results of numerical tests, is shown in Figure 7. It indicates approximately a 10:1 ratio between compressive and tensile strengths. Although that ratio is typically in the range of 15:1 or 20:1 for rock masses, 10:1 is reasonable for the generally massive Cobourg limestone. Tensile strength obtained from Brazilian tests (samples at depths of 670.15 m and 677.37 m in Table A-7 from Intera, 2007) is in the range of 8 MPa to 9 MPa.

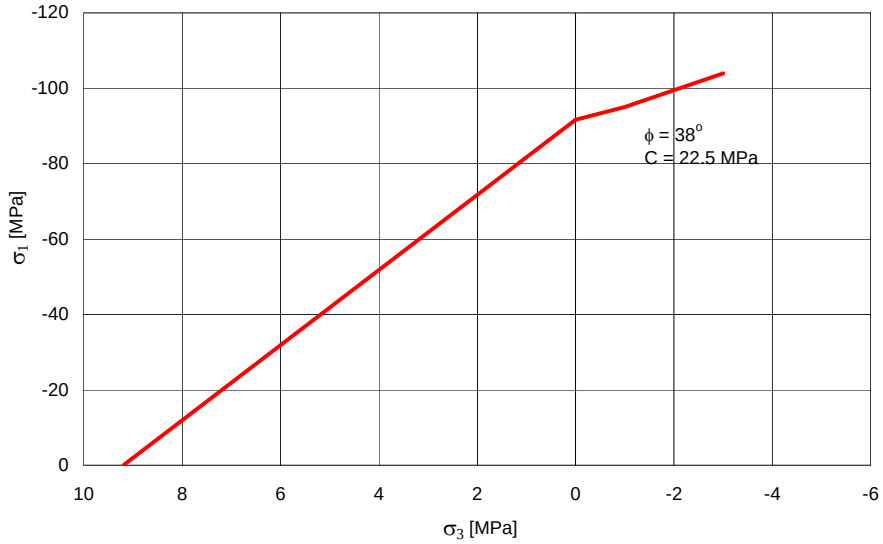

Figure 7. Failure envelope obtained based on the numerical tests on the calibrated Voronoi block model of Cobourg limestone (compression negative)

Because the geometry of the Voronoi blocks is random, the model response (including the calibration tests) will not be identical between different realizations of the block geometry. Although there will be variability in the model response between different block geometry realizations, it is important that variability is relatively small, within 10%-15% of mean. In order to verify that, the calibration tests were repeated for different block geometry realizations using the same calibrated properties. The simulations showed small, acceptable (within 5%) variability in model response.

The calibrated micro-mechanical properties for Cobourg limestone and weak Sherman Fall limestone are listed in Table 6. The properties were assumed to be uniform throughout the model (or the sample). Because the effect of spatially variable properties (e.g., normally distributed joint peak cohesion and tension with a standard deviation between 10% and 30% of the mean) on the mechanical behaviour of the Voronoi block model, which also was investigated, was not significant, it was not considered justifiable to introduce that as an additional complexity into the model.

Table 6. Calibrated micro-mechanical properties

Unit		Cobourg	weak Sherman Fall
joint normal stiffness	k_n (GPa/m)	160.3	47.8
joint shear stiffness	k_s (GPa/m)	80.1	23.9
block bulk modulus	K (GPa)	310.1	92.4
block shear modulus	G (GPa)	233.2	69.5
joint peak cohesion	c_p (MPa)	38.3	12.1
joint peak friction	ϕ_p (°)	35	35
joint peak tensile strength	T_p (MPa)	15.3	4.84
joint residual friction	ϕ_r (°)	15	15

Note: Residual micro-tension and cohesion are assumed to be zero.

From the properties in Table 6, it can be verified that the effective stiffness of Voronoi blocks with an average size of 0.3 m is much greater than joint stiffness, such that the Voronoi blocks behave as if they were infinitely stiff. For example, for the Cobourg limestone:

$$k_e = \frac{K + \frac{4}{3}G}{d} = \frac{310.1 + \frac{4}{3}233.2}{0.3} = 2,070.1\text{GPa/m} \gg 160.3\text{GPa/m}$$

where $K + (4/3)G$ is the confined axial stiffness of an elastic material, and d is the characteristic block dimension. The other extreme, when the joints are much stiffer than the blocks, also was investigated. Because the two model scenarios did not show any significant qualitative difference in material response, the entire analysis was carried out for the case described in detail here, when the blocks were practically rigid.

3.5 Time-Dependent Strength Degradation

One objective of the analysis presented here is to predict the amount of rockfall and degradation of the caverns due to long-term (100,000 years) rock strength degradation caused by stress corrosion of the Cobourg and weak Sherman Fall limestones around the caverns subjected to in-situ stresses.

3.5.1 Static-Fatigue Curves and the Evolution of Damage Due to Strength Degradation

The static-fatigue behaviour of a rock forms the basis of the *UDEC* model for stress corrosion around a cavern. The static-fatigue curves provide the time-to-failure (t_f) of the material at a particular driving-stress ratio (σ/σ_c)[2].

Because no static-fatigue data for the rock units at the repository site exist at this stage of the project, the static-fatigue data for Lac du Bonnet granite at 0, 5 MPa and 10 MPa confinements (Schmidtke and Lajtai, 1985; Lau et al., 2000), shown in Figure 8, were used as the most extensive data currently available on time-dependent strength degradation of rocks. Data sets for each confinement were fit with a straight line, and the line was extrapolated to encompass driving-stress ratios ranging from zero to one. This is a conservative assumption, because the curves (or time-to-failure) most likely approach infinity at a driving-stress ratio greater than zero. In other words, the rocks have finite long-term or true strength. (If the rock was loaded below its true strength, it would not fail, irrespective of duration of loading.) The effect of assuming finite (non-zero) long-term strength of rock mass is investigated and discussed in Section 4.1.2.2.

The two sets of extended curves that were used as input to the *UDEC* analyses based on the Lac du Bonnet data are shown in Figure 8: one set for unconfined conditions (black line) and one set for 5 MPa confinement (blue line). The sensitivity of the model predictions to static-fatigue curves (i.e., using the time-to-failure curves developed based on Yucca Mountain tuff data) is investigated and documented in Section 4.1.2.2.

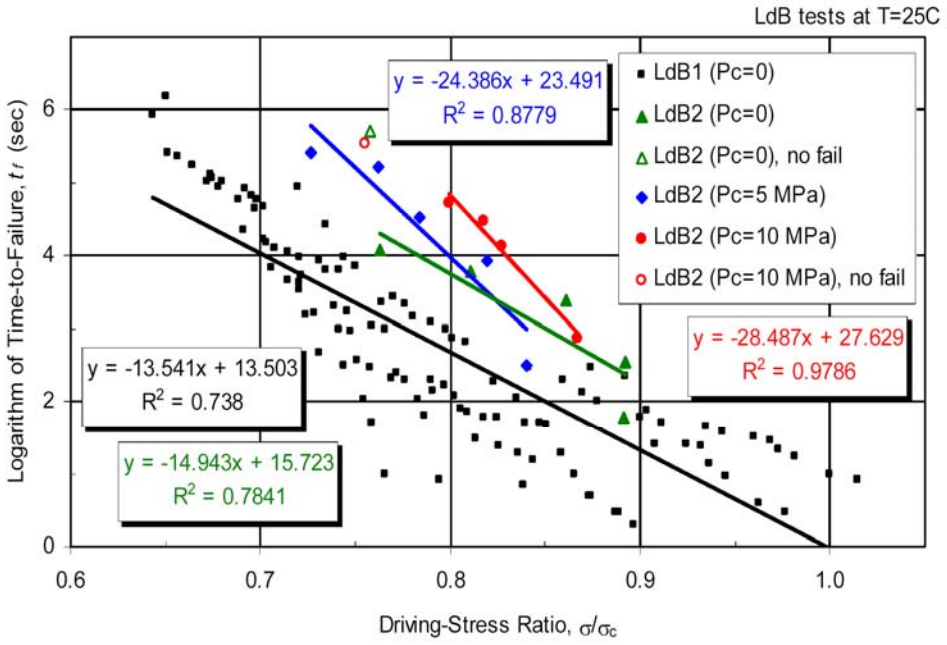

Note: LdB1 data from Schmidtke and Lajtai (1985), LdB2 data from Lau et al. (2000)

Figure 8. Static-fatigue curves used as input to the cavern stability analyses

---

2. *The following notation is employed to describe the results of static-fatigue tests. The applied load in the axial direction and the confining pressure are denoted by σ_1 and P_c, respectively. The axial load at failure during a short-term test is denoted by σ_f. The stress difference maintained during a static-fatigue test conducted at a confining pressure of P_c is $\sigma = \sigma_1 - P_c$. The stress difference at failure during a short-term test is $\sigma_c = \sigma_f - P_c$. To facilitate comparison between different data sets, we generate a static-fatigue curve by plotting the logarithm of time-to-failure, t_f, versus the driving-stress ratio given by $\sigma/\sigma_c = (\sigma_1 - P_c)/(\sigma_f - P_c)$.*

An understanding of the evolution of damage due to strength degradation during a static-fatigue test prior to the failure enables development of a modelling methodology whereby the strength of the material is degraded with time, based upon the local driving-stress ratio. The evolution of damage due to strength degradation for the static-fatigue curve (unconfined Lac du Bonnet granite) was developed using the *PFC* (Itasca, 1999) stress corrosion model (BSC, 2004a) and is shown in Figure 9 for Lac du Bonnet granite.

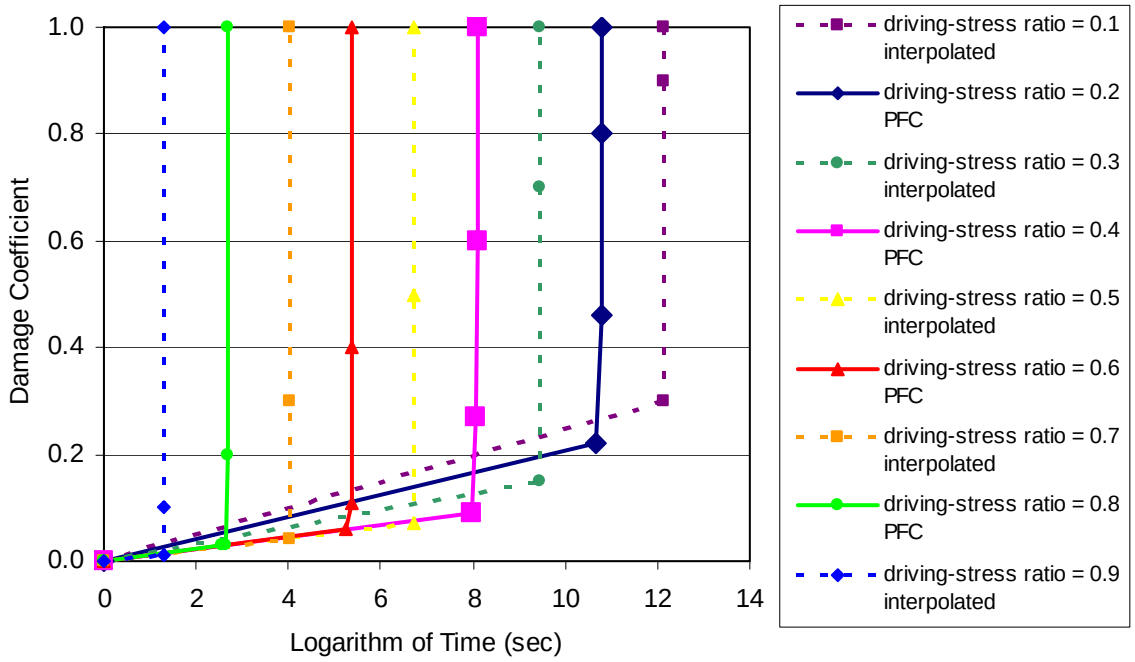

NOTE: Each curve has a vertical asymptote at a time-to-failure for a given driving-stress ratio, which is provided by the LdB (P_c = 0) curve from Figure 8. The evolution of damage up to the vertical asymptote (i.e., the failure time) is provided by the PFC stress corrosion model.

Figure 9. Damage Curves Used as Input to the UDEC LdB Analyses ($P_c = 0$)

Two parameters control the *UDEC* predictions of time-dependent strength degradation and, eventually, the predictions of rockfall: 1) time-to-failure, and 2) damage evolution (rate) before time-to-failure. The evolution of damage before failure can be approximated with a constant damage rate. Time-to-failure as a function of the stress state (i.e., the driving stress) is determined from the static-fatigue lines constructed by interpolation and extrapolation of testing results (obtained on Lac du Bonnet granite). Damage rates at different stress levels are generated using the *PFC* stress corrosion model. There is concern about the level of uncertainty in *PFC* predictions and how the damage rates affect the final result of the model (i.e., the rockfall induced by time-dependent strength degradation). In order to investigate the sensitivity of the model predictions to the damage rate, new damage curves are generated where the damage rates for all driving stress levels are assumed to be the same, equal to the maximum rate predicted by *PFC*. The rockfall predictions due to time-dependent strength reduction, using different damage curves, are compared (BSC, 2004a). It was confirmed that the considered variation of damage rates has no practical effect on predicted rockfall. Time-to-failure is the main factor controlling evolution of the rockfall due to time-dependent strength reduction. Consequently, *UDEC* predictions are not very sensitive to the input from the *PFC* stress corrosion model.

3.5.2 UDEC Stress Corrosion Modelling

The long-term strength degradation caused by stress corrosion of the Cobourg limestone units was implemented in the *UDEC* model by incrementally referencing a series of tables defining evolution of damage due to strength degradation as obtained from the *PFC* stress corrosion model (shown in Figure 8 and Figure 9). Based upon the local driving-stress ratio at the Voronoi block contacts within the *UDEC* model, the strength of the contact in the model is degraded as a function of time. The times considered were 1, 2, 5, 10, 20, 50, 100, 200, 500, 1000, 200, 5000, 10,000, 20,000, 50,000 and 100,000 years.

Time-dependent strength degradation in the *UDEC* model is generalized by a damage coefficient, D, which is in the range between zero and one. The cohesion and tensile strength of the material are assumed to be functions of time:

$$\begin{aligned} c(t) &= c_o D(t) \\ T(t) &= T_o D(t) \end{aligned} \tag{7}$$

where c_0 and T_0 are the initial, short-term cohesion and tensile strength of joints in the *UDEC* model, respectively. The large-scale short-term strength of the *UDEC* synthetic model of the rock mass is proportional to the cohesion and tensile strength of joints, c_0 and T_0, respectively. Consequently, the time-dependent strength of the *UDEC* synthetic model of rock mass will decay proportionally to $D(t)$.

It is assumed that, in the general case,

$$\frac{dD}{dt} = f(\mathrm{F}, D) \tag{8}$$

where F, a function of stress state and material strength, defines the load level (driving stress). For unconfined stress conditions (i.e., $P_c = 0$), function F must be identical to the ratio of the axial load and the unconfined short-term strength: $\mathrm{F}(P_c = 0) \equiv \sigma_1 / \sigma_f$. The load at failure during a short-term test is calculated as follows (Jaeger and Cook, 1979, pp. 95 – 97):

$$\begin{aligned} \sigma_f &= P_c N_\phi + 2c\sqrt{N_\phi} \\ N_\phi &= \frac{1+\sin\phi}{1-\sin\phi} \end{aligned} \tag{9}$$

where c and ϕ are the rock mass cohesion and friction angle, respectively. It is assumed that if time-to-failure for two different stress states were the same, then evolution of damage due to strength degradation for both states as a function of time would be the same, irrespective of the confinement. As discussed in Section 3.5.1, given the time-to-failure, the model predictions are not very sensitive to the assumption about functional form of damage evolution. Based on the existing data (Lau et al., 2000; Schmidtke and Lajtai, 1985), it can be concluded that the confinement affects the slope, $k(P_c) = \Delta(\sigma / \sigma_c) / \Delta \log(t_f)$, of the static-fatigue line. For example, the slopes of the static-fatigue lines for LdB granite (Figure 8) are:

$$k(0) = 0.051/\log(\mathrm{s})$$
$$k(5\,\mathrm{MPa}) = 0.0312501/\log(\mathrm{s}) \tag{10}$$

It was assumed that the dependence of slope k on confinement P_c is linear, as defined by the slopes of the lines for 0 and 5 MPa confining stresses. This assumption is not a consequence of the limitation of the implementation, but a reasonable simplification due to the observation that failure and damage usually takes place at low confinements. The form of function F used in the *UDEC* model is:

$$\mathsf{F} = 1 - \frac{k(0)}{k\left(P_c\right)}\left(1 - \frac{\sigma}{\sigma_c}\right) \tag{11}$$

The damage evolution $D(\mathsf{F};t)$ was generated using *PFC* for values of function F in the range between zero and one, and used as the *UDEC* input data in a tabular form (see Figure 9). Interpolation was carried out for stress states in the model during the simulation, for which function F did not coincide with values for which the tables were provided. (This is reasonable given the linear nature of the data in Figure 9.)

It is convenient for implementation that the damage increment in Equation (8) depends implicitly on stress history. The damage increment depends on accumulated damage, which is a function of the stress history. Although the stress state (at a given point) can have a complex history as a function of time (due to stress redistribution), it is sufficient in the simulation to keep track of accumulated damage only. The calculation of the damage increment in the *UDEC* simulation was carried out in the following manner. For the time increment Δt, it is assumed that the stress state and the stress function, F, at a given point in the model are constant, $\mathsf{F} = \mathsf{F}_i$. The table of damage evolution $D(\mathsf{F};t)$ is selected or interpolated based on tables provided. A point on the damage evolution curve corresponding to accumulated damage D_i is determined, $D_j = D(\mathsf{F}_i;t_j)$. The damage increment is calculated as:

$$\Delta D = D(\mathsf{F}_i;t_j + \Delta t) - D(\mathsf{F}_i;t_j) \tag{12}$$

Time increment(s) for the simulation must be selected. The only criteria for selection are the accuracy of the simulation and calculation time. The stress state is assumed to be constant during the time increment. Preliminary investigations showed that selected time increments did not affect model results significantly.

Damage is calculated and accumulated for joints. The stress state used for calculation of the damage is determined by averaging stresses in the blocks separated by a joint.

4. ANALYSES OF CAVERN STABILITY

All numerical simulations were carried out in a number of stages. In the first stage, the in-situ stresses are initialized in the model before any excavation, and a number of calculational steps are executed in order to ensure that the model is in equilibrium. The initialized in-situ stresses are generally in equilibrium with gravitational loading, but, because of the presence of jointing, some additional stress adjustment is needed for equilibrium to be achieved. In the next step, the cavern is excavated, and the new equilibrium state calculated. The excavation is simulated by instantaneous deletion of the material inside the cavern, but gradually releasing the reactive stresses of the material inside the cavern (from the initial in-situ stress state to a completely stress-free state) to ensure quasi-static evolution of the model from one equilibrium state to another. The equilibrium state of the model after cavern excavation is the initial state for simulation of time-dependent strength degradation and other analyzed loading conditions.

No ground support was considered in the analyses. Performance of ground support for an extremely long time scale is uncertain; therefore, it was conservative not to include it in the analyses. However, although this model predicts some rockfall after 10 years, it probably will not occur that early, because the ground support will still be effective and will keep loose rock from falling on the cavern floor. The ground support will not affect damage and fracturing of the rock mass.

The caverns are represented in the calculations as being completely open. Neglecting the concrete floor and the disposed waste in the model also results in overprediction of the extent of damage and rockfall in the caverns. When and if the rubble accumulates on and around the waste, it will, at some stage, fill the open space between the waste and the cavern walls as a result of bulking, and prevent further rockfall.

4.1 Time-Dependent Strength Degradation

In order to ensure that the model predictions are independent of a particular block geometry realization, the cavern stability is analyzed for three different realizations of block geometry. All three realizations have variable block size, with an average (i.e., block width) of 0.3 m. The ratio between the largest and the smallest block sizes in Cases 1 and 2 is 2, and it is 3 in Case 3. Cases 1 and 2 are two different realizations of the same block size distribution.

The simulations were carried out quasi-statically: the model is damped significantly (much more than actual material damping), and mass scaling is used to speed up model convergence to equilibrium. The model is run to equilibrium for each time increment. The equilibrium criterion is based on the maximum unbalanced force (not on the maximum model velocity) that was selected to ensure that there is no considerable stress change in the model. Consequently, “equilibrium” model states are detected when some blocks are still in free-fall. Clearly, blocks in free-fall are not in equilibrium. However, that is acceptable, because the blocks in free-fall do not affect stresses, deformation and damage in the rest of the model, which is practically in equilibrium. Waiting in the numerical simulations for each loose block to fall on the floor and equilibrate would be extremely time-consuming.

All of the time-dependent strength degradation simulations are carried out assuming completely dry rock conditions. The effect of either water or gas pressure on damage and fracturing of the rock was not accounted for in these calculations.

4.1.1 Results for the Nominal Case

The results of the three sets of simulations (i.e., Cases 1, 2 and 3 for three block geometry realizations), based on Lac du Bonnet granite time-to-failure curves and joint properties discussed in Section 3.1, are shown in Figure 10 through Figure 12. The figures show the configuration of the cavern and damage of the surrounding rock at the characteristic times. Black lines, which are at locations of micro-fractures, illustrate the damage. The results for the three analyzed cases are consistent (but not identical, as expected). The initial damage immediately after excavation is along the bedding planes ~1.5-2 m in the crown and the floor of the cavern. There is no initial damage in the cavern walls. Over time, the damage gradually extends away from the cavern boundary. After 100,000 years, the damage is approximately 4 m deep in the cavern walls. This means that there is still more than 8 m of intact pillar between the caverns. Over 100,000 years, the damage extends to ~6 m above the cavern crown. Some of that damage results in loose blocks, which fall under gravity. The rockfall is expected to start 10 years after excavation. The maximum extent of rockfall (and size of the breakout) 100,000 years after excavation is 2.5 m in the crown (Case 3, shown in Figure 12), assuming no additional loading (e.g., seismic shaking). Because of the proximity of the weak Sherman Fall unit, the extent of damage in the cavern floor (more than 6 m after 100,000 years) is greater than in the crown, where the more competent rock lies.

4.1.2 Sensitivity Analyses of Time-Dependent Cavern Degradation

Predictions of cavern performance and stability for a period of 100,000 years involves significant uncertainty. The results presented in Section 4.1 were derived using the representative input parameters, if they were available. Otherwise, the input parameters, expected to overpredict damage in the rock mass and rockfall, were used. A limited sensitivity analysis, with respect to the most uncertain and the most important input parameters, was carried out, and the results of the analysis are presented in this section.

One possible source of uncertainty in the modelling results is representation of the mechanical behaviour and strength of the bedding planes. The effect of different interpretations of the results of the direct shear tests on the bedding planes, compared to that discussed in Section 3.1, on the prediction of rock mass damage and rockfall, is investigated and the results documented in Section 4.1.2.1. The greatest uncertainty in the model prediction is in understanding of the time-dependent strength degradation of the Cobourg limestone. Rock mass damage and rockfall prediction sensitivity to different assumptions about time-dependent strength degradation are analyzed and the results documented in Section 4.1.2.2.

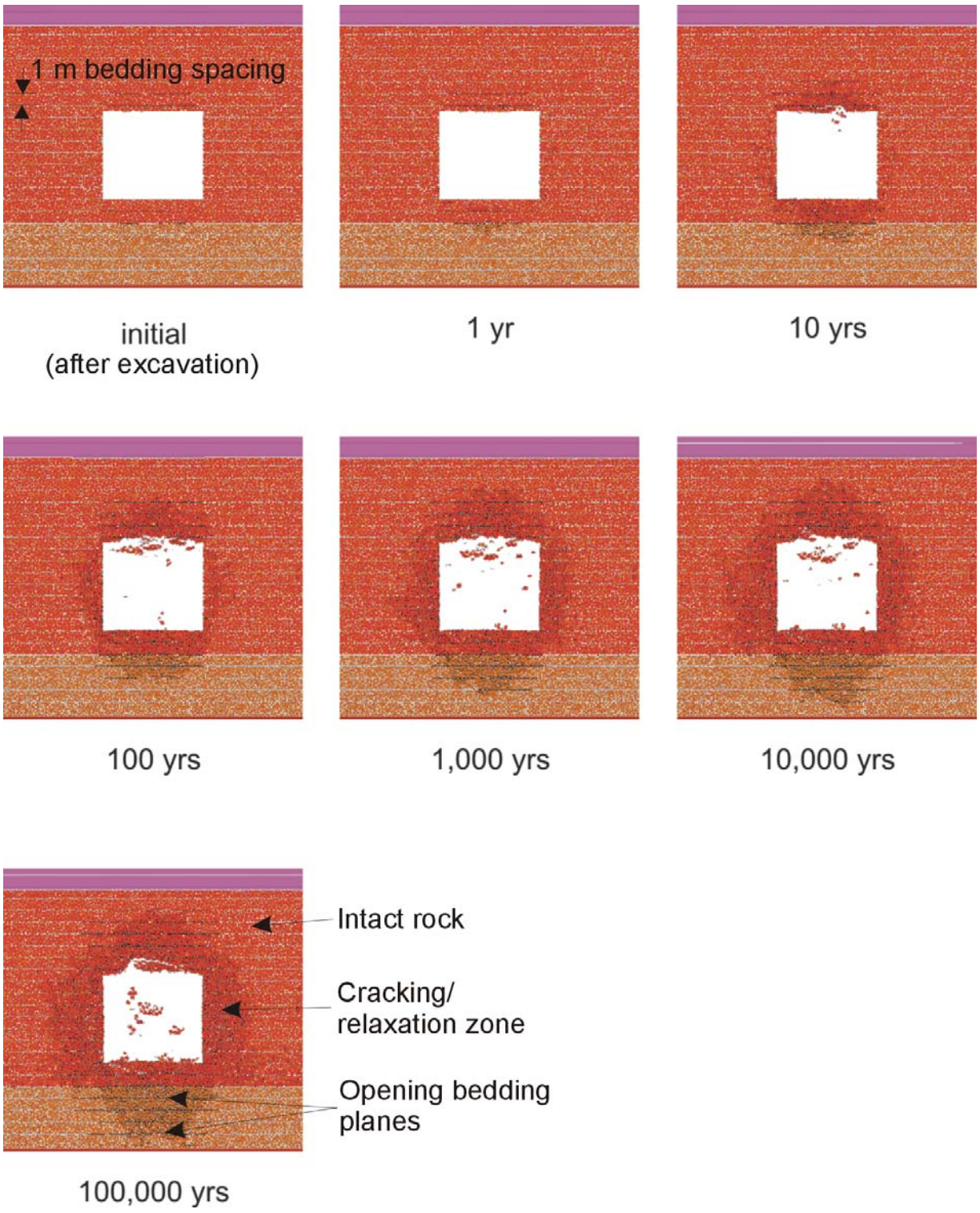

Note *Different colors represent different regions of the model. Cobourg limestone is pink; Cobourg limestone discretized into Voronoi blocks is red; weak Sherman Fall limestone discretized into Voronoi blocks is brown. Black lines represent location of the fractures.*

Figure 10. Numerically estimated evolution of cavern outline and damage: Case 1

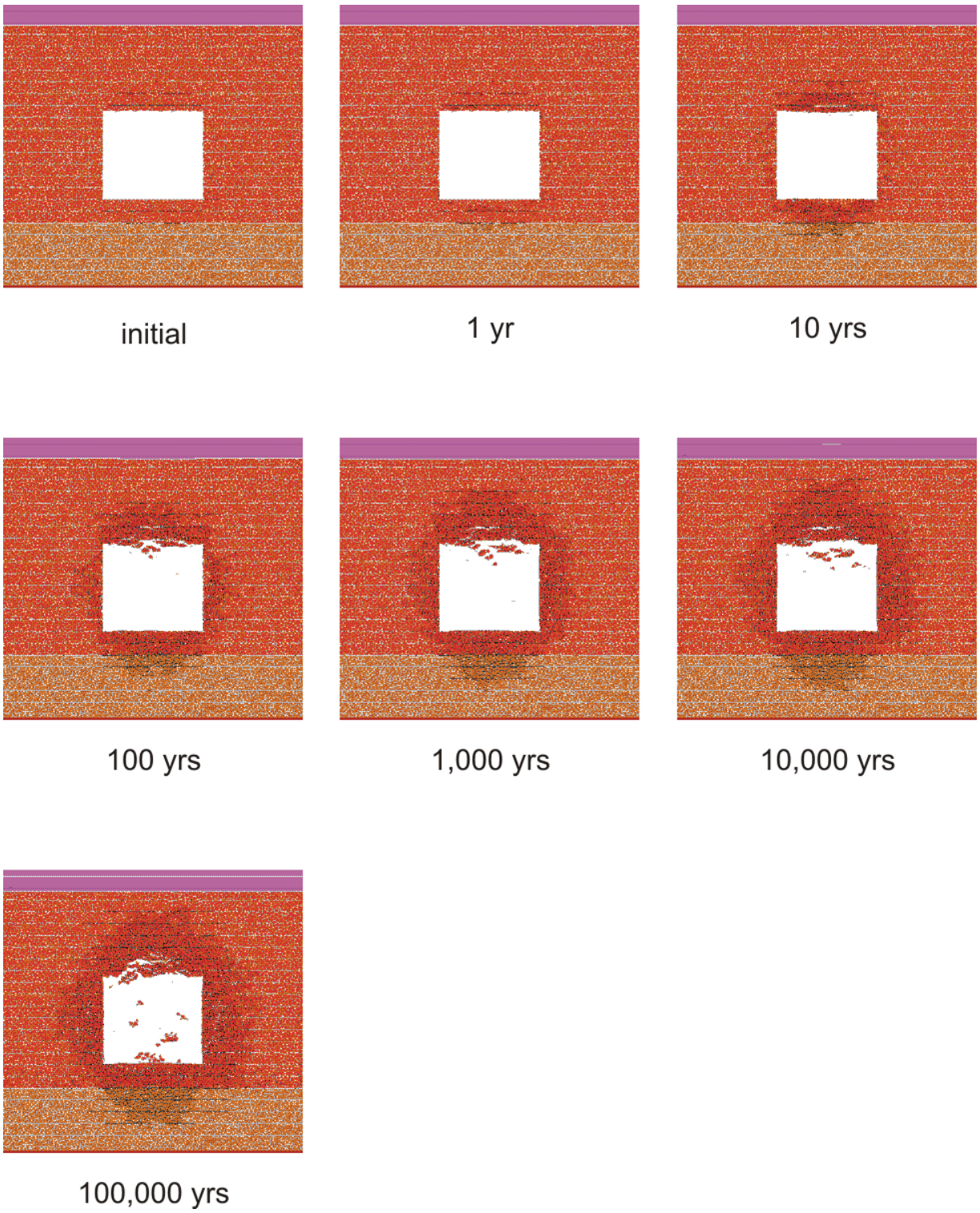

Note: Different colors represent different regions of the model. Cobourg limestone is pink; Cobourg limestone discretized into Voronoi blocks is red; weak Sherman Fall limestone discretized into Voronoi blocks is brown. Black lines represent location of the fractures.

Figure 11. Numerically estimated evolution of cavern outline and damage: Case 2

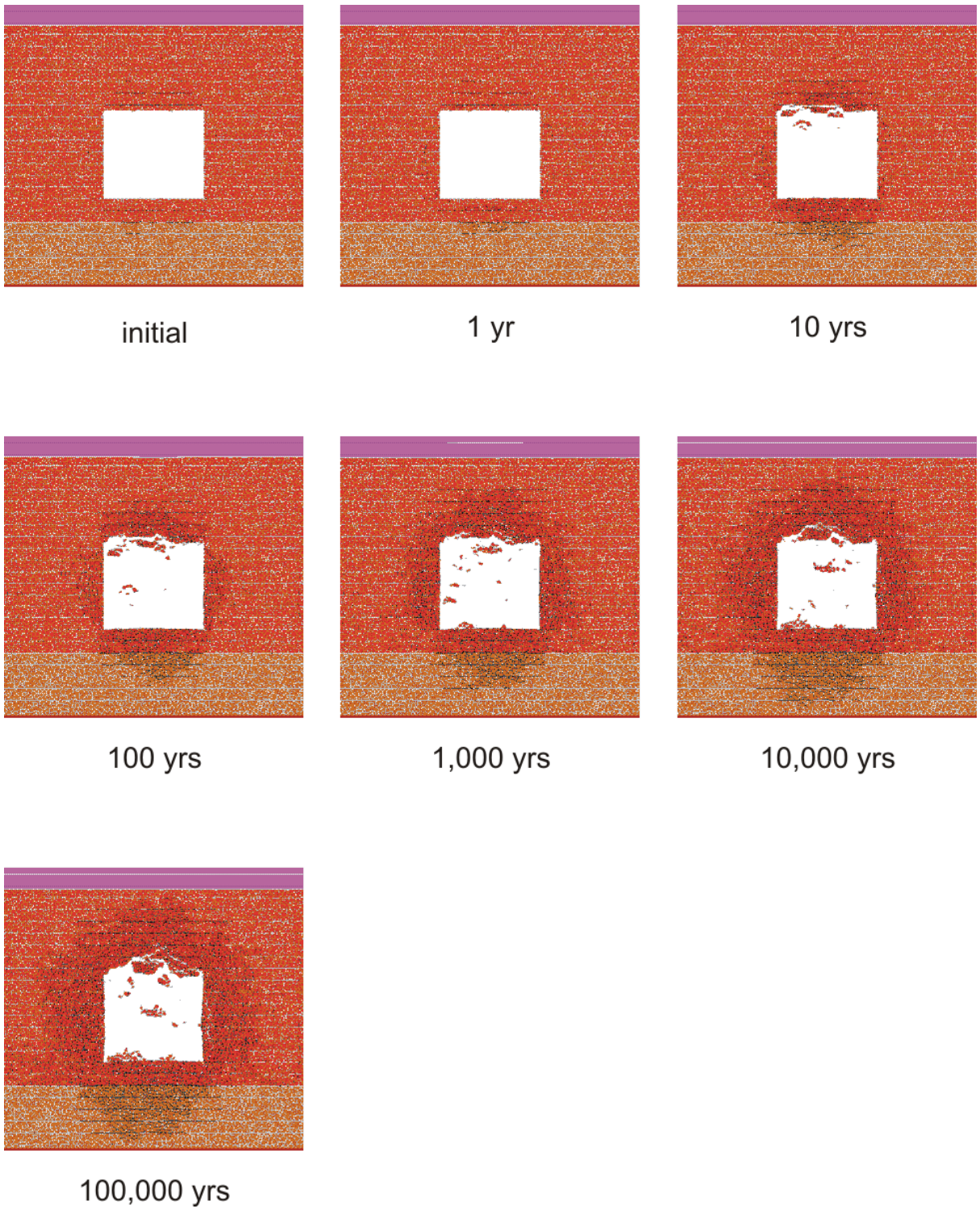

Note: Different colors represent different regions of the model. Cobourg limestone is pink; Cobourg limestone discretized into Voronoi blocks is red; weak Sherman Fall limestone discretized into Voronoi blocks is brown. Black lines represent location of the fractures.

Figure 12. Numerically estimated evolution of cavern outline and damage: Case 3

4.1.2.1 Sensitivity to Bedding Plane Strength

An interpretation of the results of the direct shear tests (Table 3 and Table 4 in Section 3.1) indicates that even the residual failure envelope in a $\sigma_n - \tau$ diagram has a non-zero intercept on the τ -axis, or apparent cohesion (an average of 0.57 MPa). The analyses in Sections 4.1 and 4.2 are carried out using non-zero residual cohesion because the data (Figures D-1 through D-8 from Intera, 2007) consistently align along straight lines with the non-zero intercept. However, sheared discontinuities typically have no cohesion, and the intercept could be an artefact of the fit of a Coulomb slip line to the data. If we postulate that residual cohesion is zero, another interpretation of the shear test data can be obtained. Each residual failure envelope was obtained from one specimen. The normal stress gradually is increased; for each increment of normal stress, the shear stress is increased until the bedding plane slips. There is progressive shearing of the asperities with increase in the normal stress and, consequently, reduction in measured friction angle. The friction angles were calculated at test stages of three additional direct shear tests (McCreath, 2007), carried out on samples from the Cobourg limestone; the averages are listed in Table 7.

Table 7. Apparent bedding plane friction angles calculated from three direct shear tests in the Cobourg limestone

Depth (m)	Stage 1	Stage 2	Stage 3	Stage 4	Average
664.94	52.5°	38.4°	32.7°	31.7°	38.8°
673.06	54.5°	49.7°	46.1°	44.8°	48.8°
684.00	61.3°	48.0°	40.1°	36.1°	46.4°
Average	56.1°				44.6°

Note Stage 1 is for a confining stress of approximately 0.5 MPa; stage 2 for approximately 1 MPa; stage 3 for approximately 1.5 MPa; and stage 4 for approximately 2 MPa.

The friction angle decreases with increase in confinement, with 44.6° being the average from all results. The friction angles obtained at stage 1, before the asperities are sheared off, are the most representative of the bedding plane intact friction angle. Thus, the rounded, average friction angle from stage 1 of three tests (56°) is taken in the sensitivity calculations to be the intact friction angle. The residual friction angle is taken to be 45°, the rounded overall average from Table 7. Using the friction angles from the residual shear strength tests, stage 1 (Table 7), and the formula in Equation (2), the new cohesion is calculated. The values for each of three shear tests and the average are listed in Table 8. Comparison of the original bedding plane strength parameters (developed in Section 3.1 and used in the analyses described in Section 4.1) and the new parameters is shown in Table 9.

Table 8. Peak cohesion calculated from the direct shear tests (McCreath, 2007) using an alternative interpretation

Depth (m)	Peak shear stress (MPa)	Normal stress (MPa)	ϕ (°)	c (MPa)
664.94	4.01	0.62	52.50	3.19
673.06	3.03	0.64	54.50	2.14
684.00	3.65	0.62	61.30	2.52
			average	2.62

Table 9. Comparison of the original and the new bedding plane strength parameters

	Intact cohesion (MPa)	Residual cohesion (MPa)	Intact friction angle (°)	Residual friction angle (°)
Original interpretation	3.19	0.57	31	31
New interpretation	2.62	0.00	56	45

The evolution of damage and rockfall as a result of time-dependent strength degradation, using new bedding plane strength parameters, is shown in Figure 13. Except for bedding plane strength properties, the new simulation is otherwise identical to Case 1, illustrated in Figure 10. The predictions of cavern outline and rock mass damage evolution for 100,000 years after waste emplacement are not very sensitive to considered variation of bedding plane strength. The results shown in Figure 10 and Figure 13 are the same for practical purposes.

4.1.2.2 Sensitivity to Time-to-Failure Curves

Although rocks have non-zero long-term strength, it is, clearly, very difficult to measure that strength experimentally. There are different hypotheses about long-term rock strength, but none is accepted generally. This is the reason that the analysis documented in Section 4.1 was conducted using the very conservative assumption that the long-term strength of the Cobourg limestone is zero.

However, many authors agree that long-term rock strength is not less than 40%-60% of the short-term UCS. That stress level is in agreement with the crack initiation stress, σ_{ci}, which is the stress level when the first cracking is detected during tests. The agreement between the long-term rock strength and the crack initiation stress is also mechanistically reasonable. If a load does not initiate any cracks in the rock under short-term, static loading conditions (i.e., when the load is lower than the crack initiation stress), the mechanisms of stress corrosion, which operate at crack tips and are the main cause of time-dependent strength degradation, will not be activated. Consequently, there will be no strength degradation.

Based on the UCS measurements (Table 2), the average value of the crack initiation stress for the Cobourg limestone is 0.44 UCS. The time-dependent strength degradation simulations were repeated using the static-fatigue curves for Lac du Bonnet granite (shown in Figure 8); however, instead of extrapolating the trend determined from the laboratory data to the zero driving stress ratio, it was assumed that, for a driving stress ratio less than or equal to 0.4 UCS, the time-to-failure is infinite and the damage accumulation rate is zero. If the results of this simulation, shown in Figure 14, are compared with the results for Case 1 (shown in Figure 10), it is clear that the increase in the long-term strength from zero to 0.4 UCS has a significant effect on the predicted extent of damage and rockfall. The greatest effect is in the cavern walls, where almost no damage is predicted in the new simulations. However, the damage in the crown and the floor is also reduced. The damage region at the end of simulation extends approximately 3.5 m from the cavern crown. Only a 0.5 m-thick slab detaches from the crown resulting in rockfall.

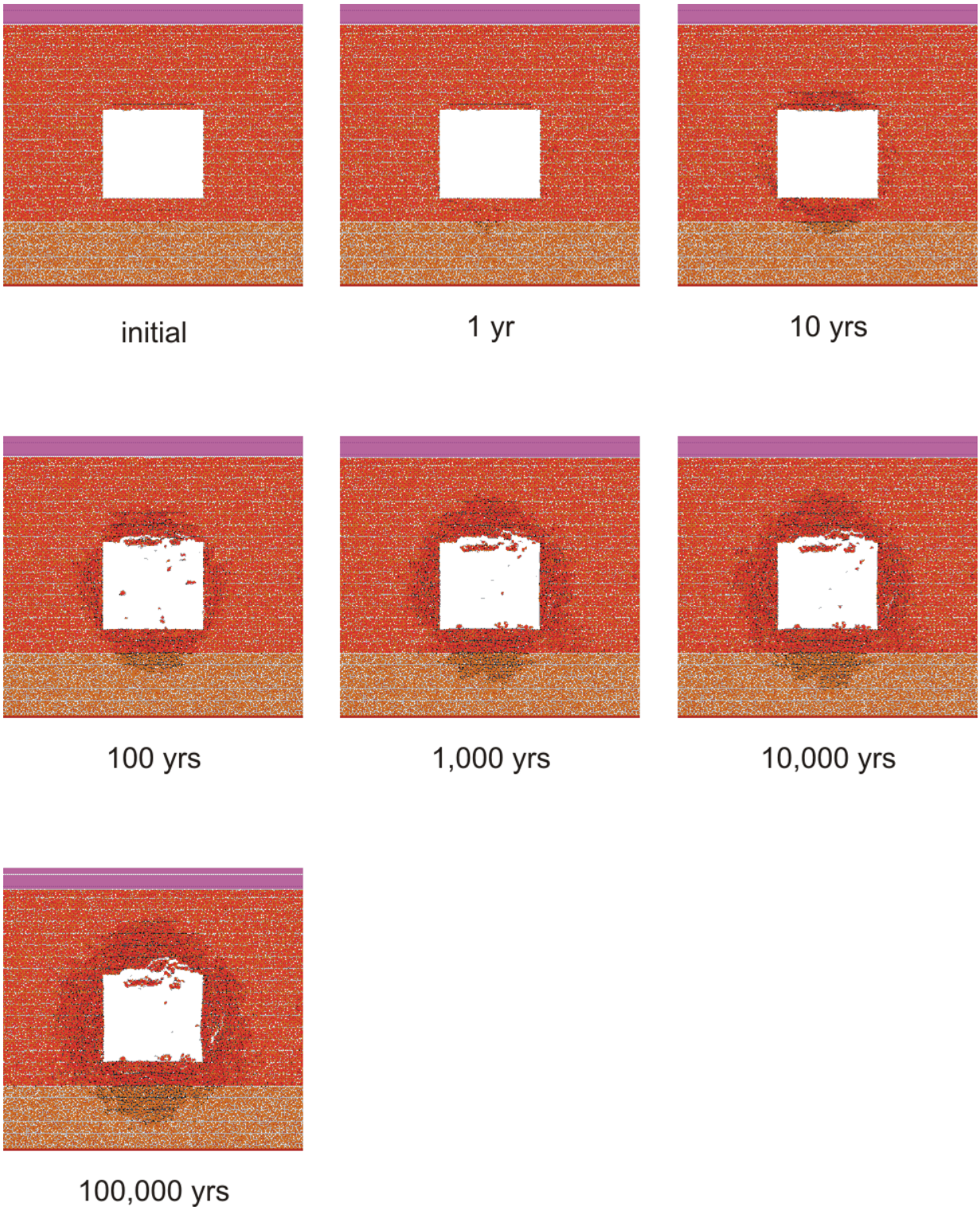

Note: Different colors represent different regions of the model. Cobourg limestone is pink; Cobourg limestone discretized into Voronoi blocks is red; weak Sherman Fall limestone discretized into Voronoi blocks is brown. Black lines represent location of the fractures.

Figure 13. Numerically estimated evolution of cavern outline and damage: Bedding plane strength sensitivity analysis

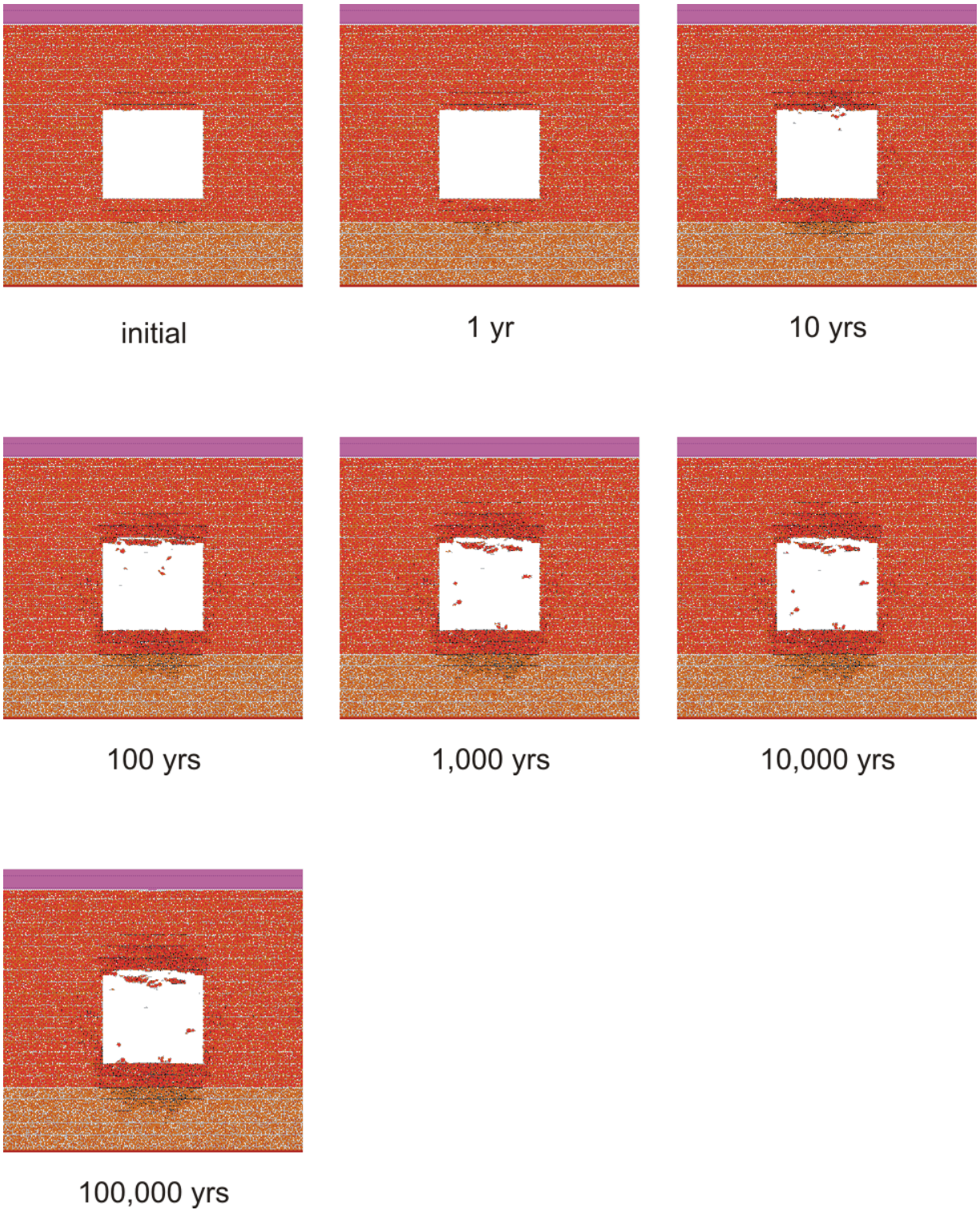

Note: Different colors represent different regions of the model. Cobourg limestone is pink; Cobourg limestone discretized into Voronoi blocks is red; weak Sherman Fall limestone discretized into Voronoi blocks is brown. Black lines represent location of the fractures.

Figure 14. Numerically estimated evolution of cavern outline and damage: Rock mass long-term strength assumed to be 40% of UCS

The contour plot of driving-stress ratio after cavern excavation (Figure 15) can help the understanding of the effect of a long-term strength of 0.4 UCS on time-dependent cavern stability. (For a confined stress condition, when $\sigma_3 < 0$, the driving-stress ratio is reduced to the value that has the same time-to-failure for unconfined conditions.) In the plot, the region of the rock mass for which the driving-stress ratio is less than 0.4 (i.e., less than the long-term strength of rock mass) is purple. Although there are some regions in the cavern walls with a driving-stress ratio greater than 0.4, those regions have relatively small total area and are scattered randomly. Thus, where the long-term strength of rock is greater than 0.4 UCS, some localized fracturing in the cavern wall will occur over time, relaxing the stresses locally. However, that fracturing will not cause major stress redistribution (that would create new stress concentrations that exceed long-term rock strength), and the process of time-dependent strength degradation in the walls will be arrested. The regions in the crown and the floor with a driving-stress ratio greater than 0.4 have greater area and are continuous. Time-dependent strength degradation will result in coalescing of cracks, formation of loose ground, and significant stress redistribution that could lead to continuation of the damage process. However, with long-term strength equal to 0.4 UCS, the fracturing in the crown and floor is less extensive than in the case when the long-term strength is zero.

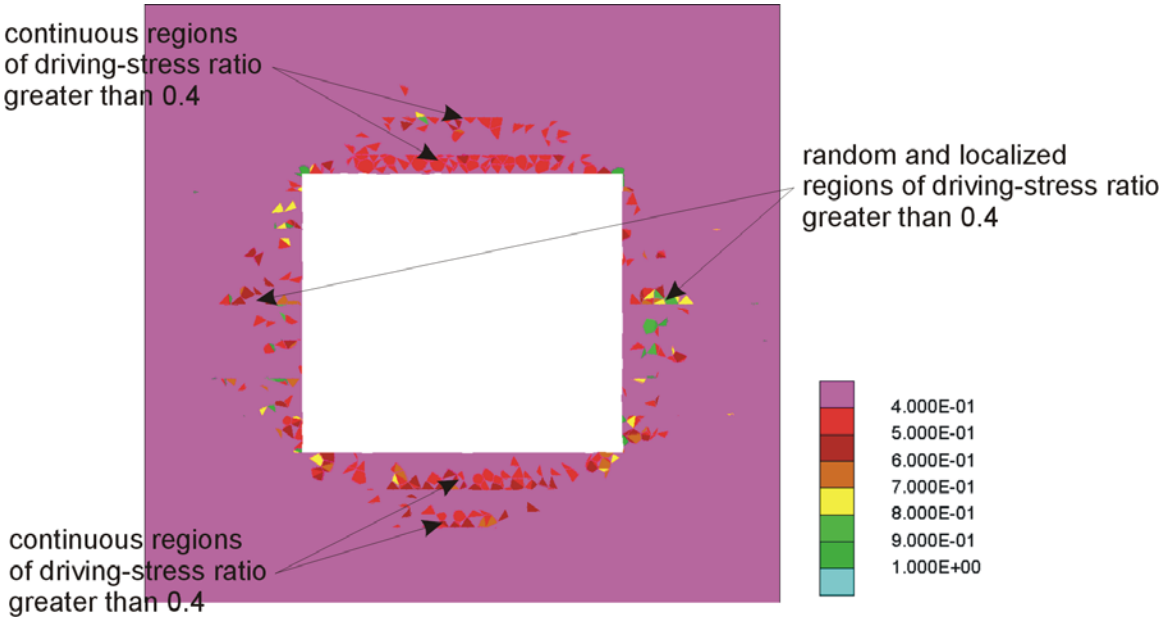

Note: Only the values between 0.4 and 1.0 are contoured. For confined stress conditions (i.e., when $\sigma_3 < 0$), the driving-stress ratio is reduced to the value that has the same time-to-failure for unconfined conditions.

Figure 15. Contours of driving-stress ratio after cavern excavation

Times-to-failure based on static-fatigue tests on Lac du Bonnet granite, also shown in Figure 8, are listed, in Table 10, in different time units for some characteristic driving-stress ratios. The table illustrates that the times-to-failure are relatively very short, leading to conservative predictions of damage in Cobourg limestone and rockfall in the caverns over time. For example, time-to-failure is less than 8 minutes for a driving-stress ratio of 0.8, less than 3 days for a driving stress ratio of 0.6, and less than 4 years for a driving stress ratio of 0.4.

Table 10. Times-to-failure as a function of driving-stress ratio for Lac du Bonnet granite (from Figure 8)

Driving-Stress Ratio	Time to failure (years)	Time to failure (days)	Time to failure (minutes)
0.9	6.57E-06	2.40E-03	3.45E+00
0.8	1.48E-05	5.42E-03	7.80E+00
0.7	3.35E-04	1.22E-01	1.76E+02
0.6	7.58E-03	2.77E+00	3.98E+03
0.5	1.71E-01	6.24E+01	8.99E+04
0.4	3.87E+00	1.41E+03	2.03E+06
0.3	8.75E+01	3.19E+04	4.60E+07

Considering that the limestone is a fine-grained rock compared to the granite, it is expected that times-to-failure of the limestone will be longer. Coarse-grained rocks are more heterogeneous and, consequently, have more heterogeneous stress fields on the micro scale, which make them more susceptible to damage and fracture. Tuff, which is the host formation for the designed deep geological repository of high-level nuclear waste at Yucca Mountain, Nevada, U.S., is also relatively fine-grained rock. Martin et al. (1997) conducted static-fatigue tests on Yucca Mountain tuff. The time-to-failure data and best-fit lines for Lac du Bonnet granite and Yucca Mountain tuff are compared in Figure 16.

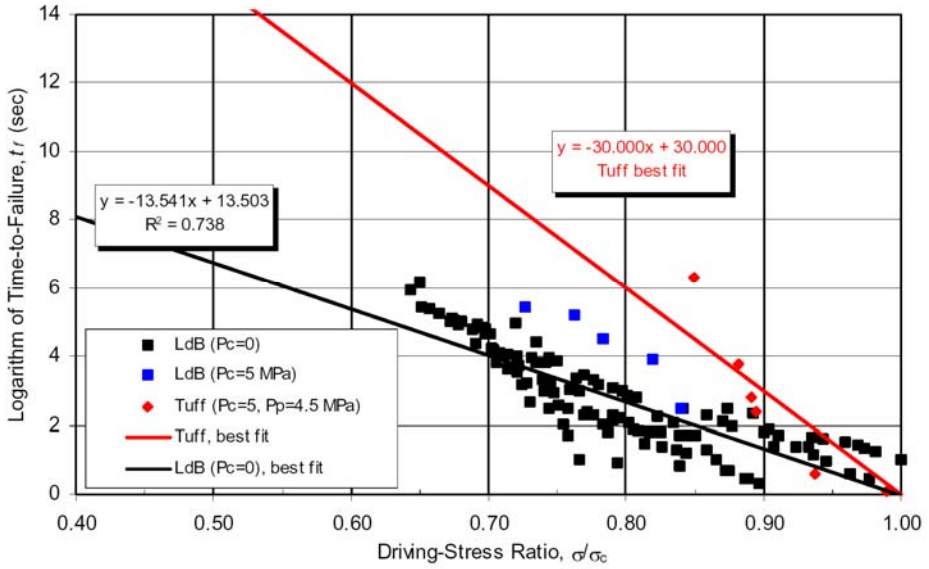

Note: LdB data from Schmidtke and Lajtai (1985) and Lau et al. (2000); tuff data from Martin et al. (1997).

Figure 16. Static-fatigue curves for Luc du Bonnet granite and Yucca Mountain tuff

There are less data available for the Yucca Mountain tuff than for the Lac du Bonnet granite, but they indicate a general trend with much longer times-to-failure. For example, for a driving stress ratio of 0.8, time-to-failure is of the order of 10 days—not 10 minutes, as shown in Table 10 for Luc du Bonnet granite; for a driving stress ratio of 0.6, which is probably approaching the long-

term strength of most of the rocks, time-to-failure is of the order of 30,000 years—not 1 day, as shown in Table 10 for Luc du Bonnet granite. The two fits in Figure 16 represent wide range of time-dependent behaviours.

The results of the simulation of the cavern stability at OPG DGR, using the static-fatigue curve for Yucca Mountain tuff, are shown in Figure 17. Compared to the state after cavern excavation, no significant increase in damage is predicted due to time-dependent strength degradation over 100,000 years. The model does not indicate any rockfall as a result of damage in the Cobourg limestone.

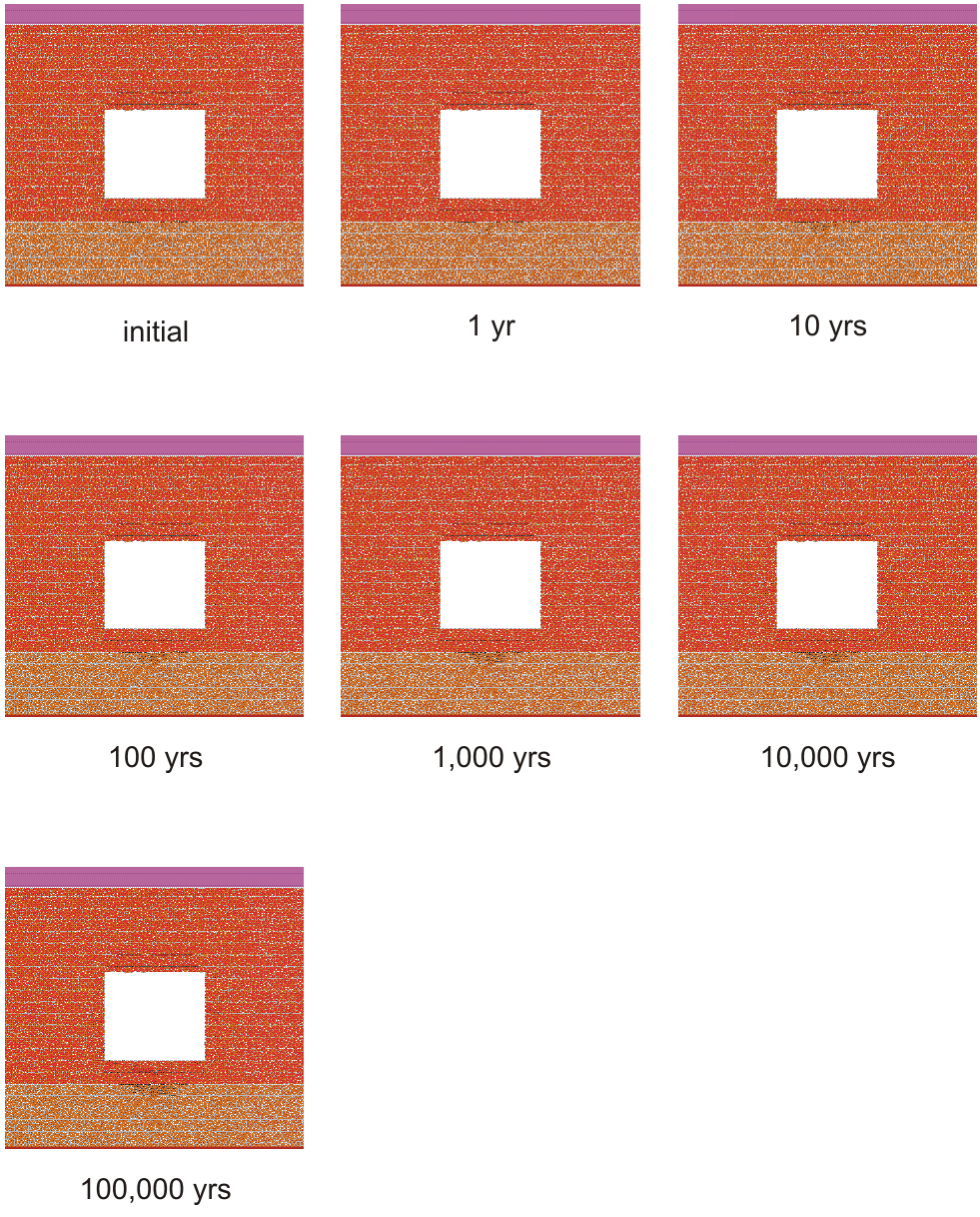

Note: Different colors represent different regions of the model. Cobourg limestone is pink; Cobourg limestone discretized into Voronoi blocks is red; weak Sherman Fall limestone discretized into Voronoi blocks is brown. Black lines represent location of the fractures.

Figure 17. Numerically estimated evolution of cavern outline and damage: Time-to-failure based on static-fatigue tests on tuff from Yucca Mountain (Martin et al., 1997)

4.2 Effect of Gas Pressure

4.2.1 Gas Pressures and Method of Analysis

Corrosion processes of the waste inside the caverns, which is different from the rock stress corrosion discussed in Section 3.5.1, will result in the generation of gases. Because of the low permeability of the Cobourg limestone formation, a significant amount of the gas will remain inside of the caverns, resulting in a gradual build-up of gas pressure. Avis et al. (2007) conducted an analysis of gas pressure evolution in the caverns at the OPG DGR. The mechanical effects on cavern stability of three cases of gas pressure histories, shown in Figure 18, are investigated and the results discussed here. The maximum gas pressures for each case, and the times when they occur, are listed in Table 11.

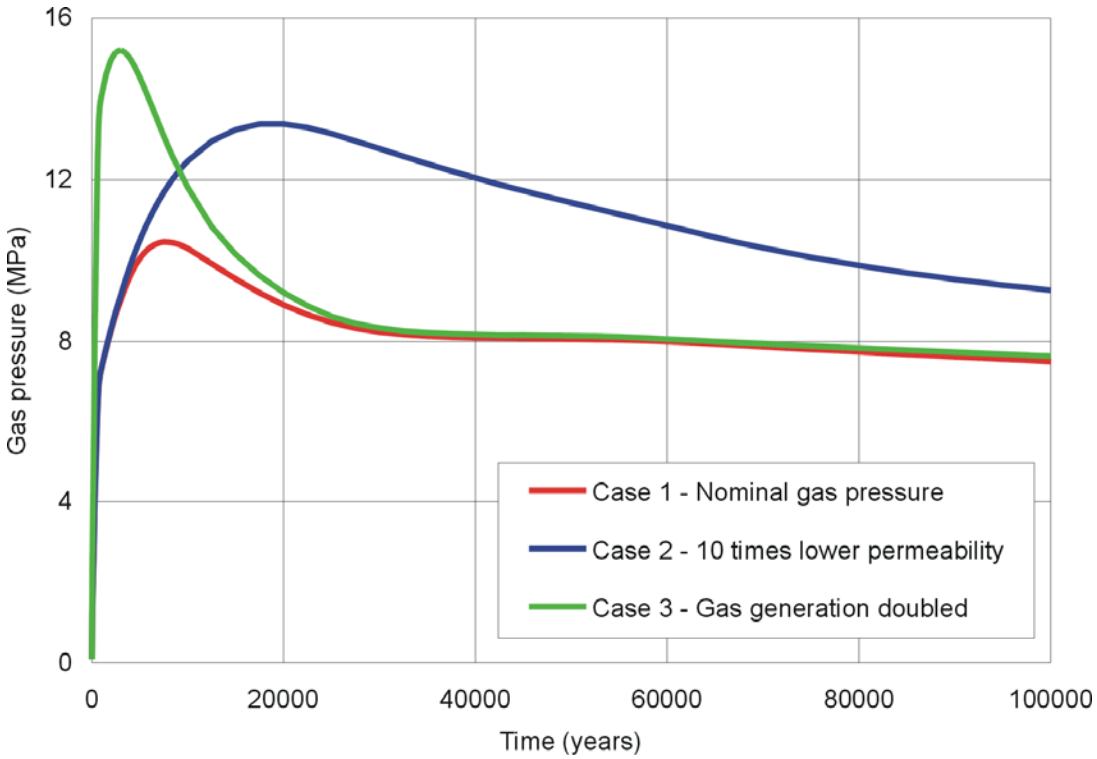

Note: Cases 2 and 3 are variants of Case 1.

Figure 18. Gas pressure histories inside the cavern (Avis et al., 2007)

Table 11. Maximum gas pressures and times when they occur

Case	Time of maximum pressure (years)	Maximum pressure (MPa)
1	7,500	10.46
2	20,000	13.39
3	3,000	15.21

Because the main issue related to gas pressure is containment of the gas inside the caverns and the possibility of gas release as a result of hydrofracturing of the surrounding rock, the model is simplified from that presented in Sections 3.3 and 4.1. Instead of using a Voronoi block model to represent damage and fracturing of the Cobourg limestone, a strain-softening Mohr-Coulomb constitutive continuum model is used. Bedding planes, which are likely locations of hydrofractures because of their favourable orientation relative to the principal stresses (normal to the vertical stress, the minor principal stress) and because they are planes with reduced tensile strength, are included explicitly in the model as discontinuities. The stiffness and strength parameters of the Mohr-Coulomb model as listed in Table 5 are assigned to the Cobourg and weak Sherman Fall limestone. Softening post-peak behaviour is assumed. After the materials reach their peak strength, they soften in such a manner that cohesion reduces to 10% of the peak (intact) cohesion over 0.2% of the plastic shear strain. Further straining does not cause additional reduction of the cohesion (i.e., the residual cohesion is 10% of the peak cohesion). Although the laboratory tests do not provide information about post-peak behaviour, the assumed approximation is reasonable and roughly the same as the post-peak behaviour observed in the response of the Voronoi block model (Figure 5). The friction angle is constant, independent of plastic deformation.

Cohesion and tensile strength also are reduced, following a procedure similar to the one described in Section 3.5.2, to account for time-dependent strength degradation. In order to validate the continuum approach, the problem of time-dependent degradation (without gas or water pressure) is solved using the continuum approximation and compared to the equivalent Voronoi scenario. The predicted extent of the damaged rock mass around the cavern is shown in Figure 19. Those results are in a good agreement with the results of the Voronoi block model, shown in Figure 10 through Figure 12.

The gas pressure histories, as shown in Figure 18, are applied to all cavern walls. Despite the very low permeability of the Cobourg limestone, and because of the long duration of the gas pressure inside the cavern, the gas will flow into the formation and generate pore pressures that will exceed the in-situ water pressure within a considerable distance from the cavern walls. The increased pore pressures of the gas will affect the conditions of fracturing and failure of both intact Cobourg limestone and of the bedding planes within the limestone. The gas saturation and pressure distribution inside the rock also are calculated as part of the model, from which gas pressure histories (Figure 18) are generated (Avis et al., 2007). Gas pressure histories are provided (Avis, 2007) at five elevations above (1 m, 6 m, 10 m, 16 m and 45 m) and below (-1 m, -6 m, -11 m, -20 m and -49 m) the caverns. The repository-scale gas flow model provides variation of the gas pressure in the middle of the repository in the vertical direction only. Considering the very long time scale that is simulated and the relatively close spacing of the caverns, that approximation is reasonable. Instead of importing the pressure histories into the model directly, the gas pressure field and its evolution over time are approximated. Gas pressure was assumed to vary linearly from the value inside the cavern to the in-situ (hydrostatic) water pressure at a 60 m distance from the cavern boundary, as long as the pressure inside the cavern was less than the hydrostatic pressure. When the gas pressure inside the cavern exceeded the hydrostatic pressure, gas pressure was assumed to vary linearly from the value inside the cavern to the in-situ (hydrostatic) water pressure at a 400 m distance from the cavern boundary. The gas pressure field changed only as a function of the magnitude of the gas pressure inside the cavern. The distances of 60 m and 400 m were selected from the condition that the approximations of the pressure fields are good and conservative (i.e., overestimates the gas pressures) for the intended use.

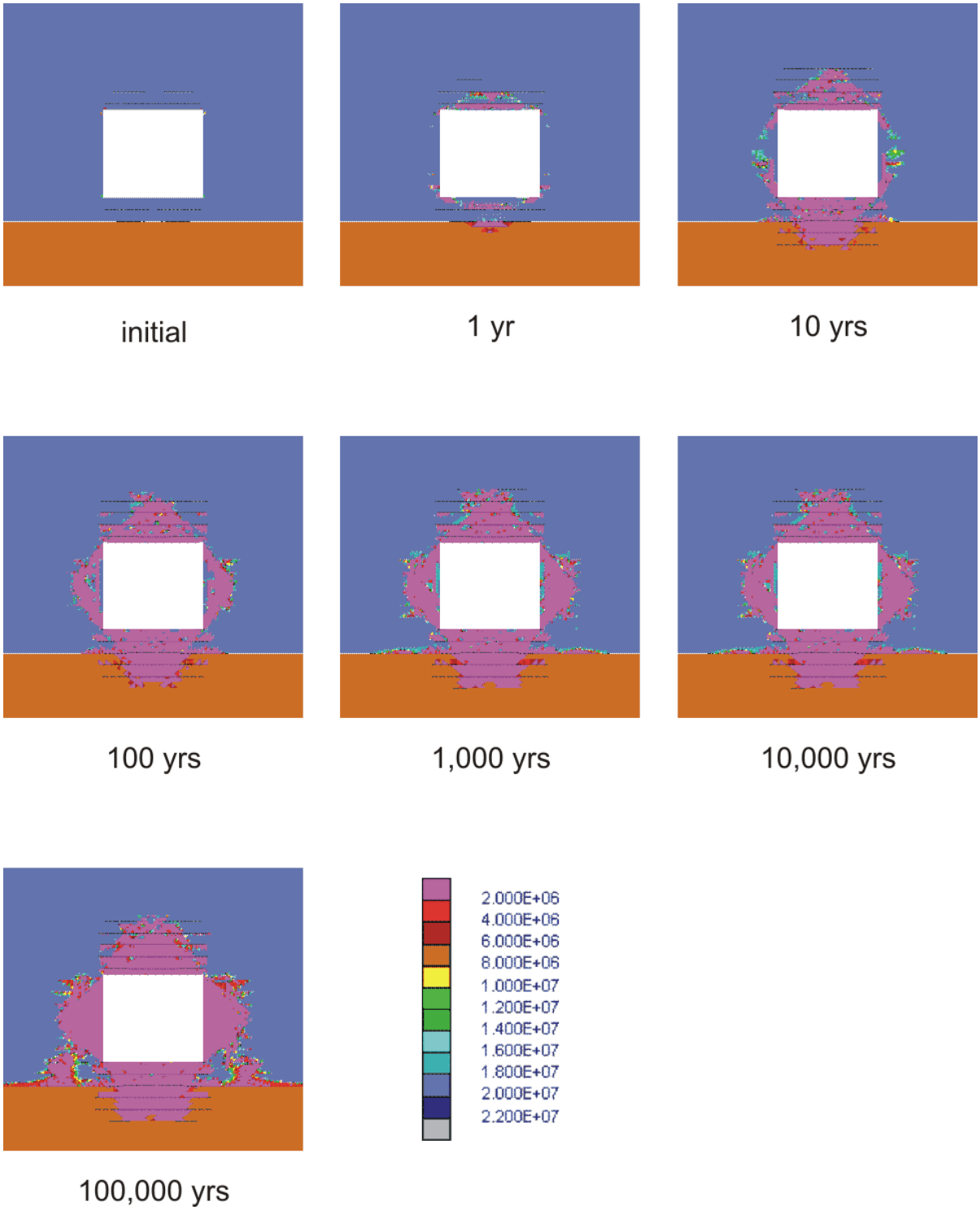

Note: Colors represent the magnitude of cohesion (Pa). As cohesion decreases due to damage, the purple color indicates completely damaged rock. Black lines indicate the locations of fractures along the bedding planes.

Figure 19. Damage around the cavern due to time-dependent rock-strength degradation estimated using continuum representation (Bedding planes are represented as discontinuities.)

The conducted analysis is not a fully coupled hydro-mechanical simulation. The initialized gas pressures in the bedding planes and in the rock affect the deformation and the conditions of failure, but the gas pressures or rock permeability do not change due to rock deformation. (The gas pressure in the rock changes as calculated according to the predefined gas pressure history in the cavern as a result of gas diffusion into the rock of given permeability.) The analysis does not include the simulation of fluid flow along the open fractures, which is a non-conservative simplification. However, because the pore pressure gradient (which is the same in the rock and the bedding planes) around the cavern is relatively small, the pressures in the open fractures are underestimated insignificantly. On the other hand, in the calculations, the pore pressures do not change as a function of matrix or fracture deformation, which can result in a significant underestimation of pore pressures, particularly in the vicinity of the cavern where severe deformation (fracturing) is expected. Overall, the completed analysis is conservative (i.e., overpredicts damage and fracturing) compared to a fully coupled hydro-mechanical simulation.

4.2.2 Results of Gas Pressure Analysis

The damage[3] and fracturing of the rock due to time-dependent strength degradation and three gas pressure histories are analyzed and the results shown in Figure 20 through Figure 22. Comparison of the results obtained for different cases of gas pressure with those without gas pressure indicates that gas pressure increases damage. However, the increase in the extent of damage around the cavern (particularly in the walls and in the crown) is not significant. Gas pressure causes an increase in the damage region above the cavern to, at most, 7 m from the cavern boundary (Case 3 pressure history). The greatest effect of gas pressure is on the damage in the Cobourg limestone along the interface with the weak Sherman Fall limestone. As the damage in the cavern floor extends through the slab of good quality Cobourg limestone in the cavern floor, horizontal stresses concentrated in the slab are released. Consequently, due to large gas pressure, the effective horizontal stresses become tensile, and result in damage and inelastic deformation. It is not expected that the damage along the interface would affect the stability of the caverns or the pillars between the caverns because the damaged region is confined.

Gas pressure does not cause the additional opening of bedding planes (particularly those in the cavern wall) in gas pressure Cases 1 and 2. The bedding planes in the cavern wall will be opened by Case 3 gas pressure (when the maximum is reached) to, at most, 2-3 m from the cavern wall. (Black lines in the cavern wall shown in Figure 22 indicate the bedding planes that were opened at some time during the gas pressure history.) Because the peak gas pressure (15.21 MPa for Case 3) is less than the vertical stress at the repository level (18.31 MPa), even though the fractures are initiated in the cavern wall, they cannot propagate far.

The preferential direction of hydrofracturing will be horizontal, along bedding planes. The potential for opening of bedding planes due to gas pressure also is investigated for the bounding case, when there is no time-dependent rock strength degradation. This analysis was carried out for extreme Case 3 gas pressure history only. Because the condition for horizontal fracture propagation is most favourable at the cavern at the edge of repository (having the least vertical stress concentration in the cavern wall), the analysis was carried out for two cavern configurations: in the middle of the repository, and at the edge of the repository. To represent the conditions at the edge of the repository, the left vertical model boundary (Figure 1) was moved sufficiently away (approximately five cavern spans) from the cavern wall. The results of

3. *Damage here means percentage of loss of cohesion and tensile strength. Thus, damage greater than zero does not necessarily mean failure of the rock.*

these calculations are shown in Figure 23 and Figure 24. When there is no time-dependent strength degradation, the fractures along the bedding planes localize in the floor and at the crown of the cavern. At the edge of the repository, as expected, the fractures propagate farther, approximately 16 m. Again, because the gas pressure is less than the minor principal stress (vertical stress), the fractures cannot propagate far.

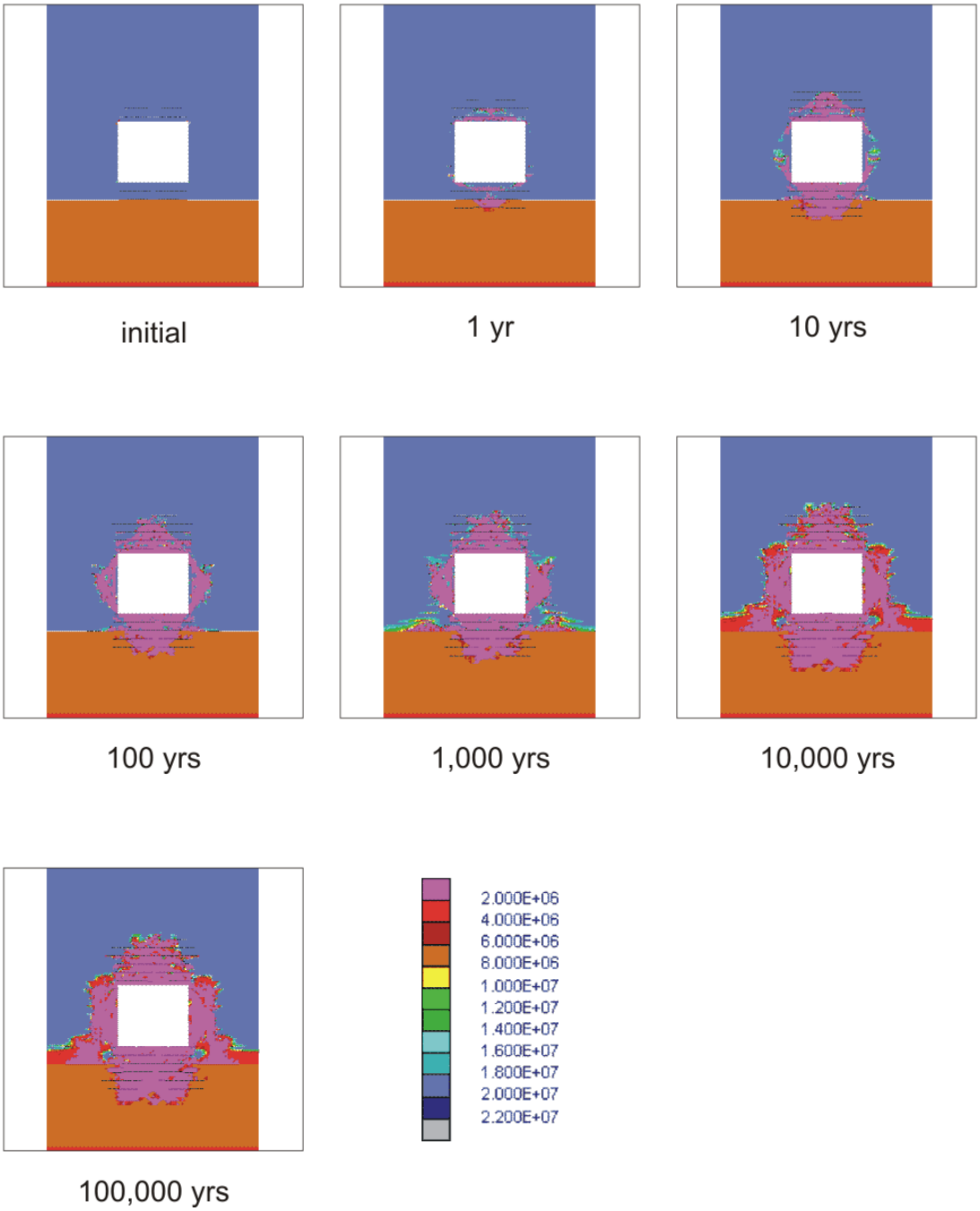

Note: Colors represent the magnitude of cohesion (Pa). As cohesion decreases due to damage, the purple color indicates completely damaged rock. Black lines indicate the locations of fractures along the bedding planes.

Figure 20. Damage around the cavern due to time-dependent rock strength degradation and gas pressure history Case 1, estimated using continuum representation

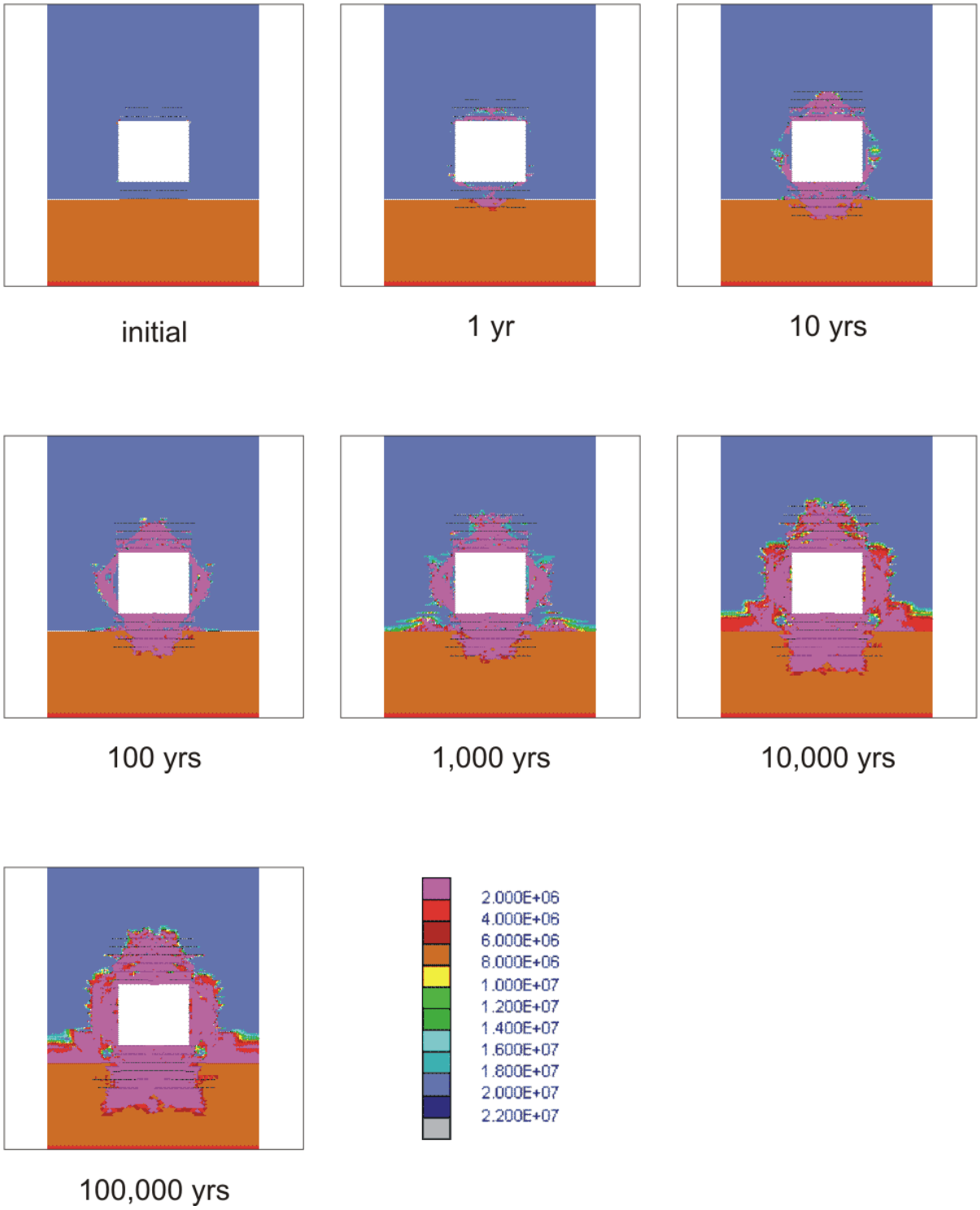

Note: Colors represent the magnitude of cohesion (Pa). As cohesion decreases due to damage, the purple color indicates completely damaged rock. Black lines indicate the locations of fractures along the bedding planes.

Figure 21. Damage around the cavern due to time-dependent rock strength degradation and gas pressure history Case 2, estimated using continuum representation

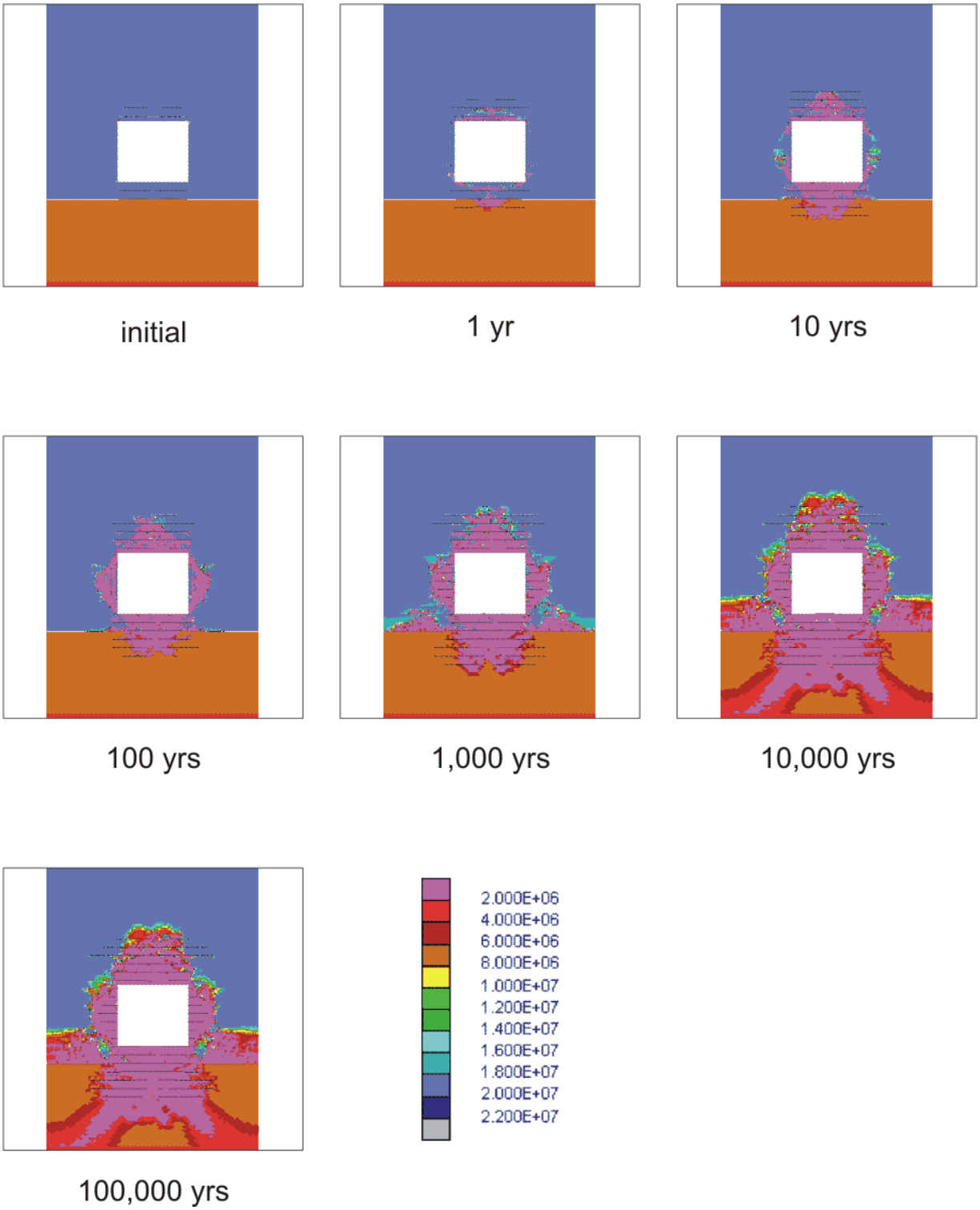

Note: Colors represent the magnitude of cohesion (Pa). As cohesion decreases due to damage, the purple color indicates completely damaged rock. Black lines indicate the locations of fractures along the bedding planes.

Figure 22. Damage around the cavern due to time-dependent rock strength degradation and gas pressure history Case 3, estimated using continuum representation

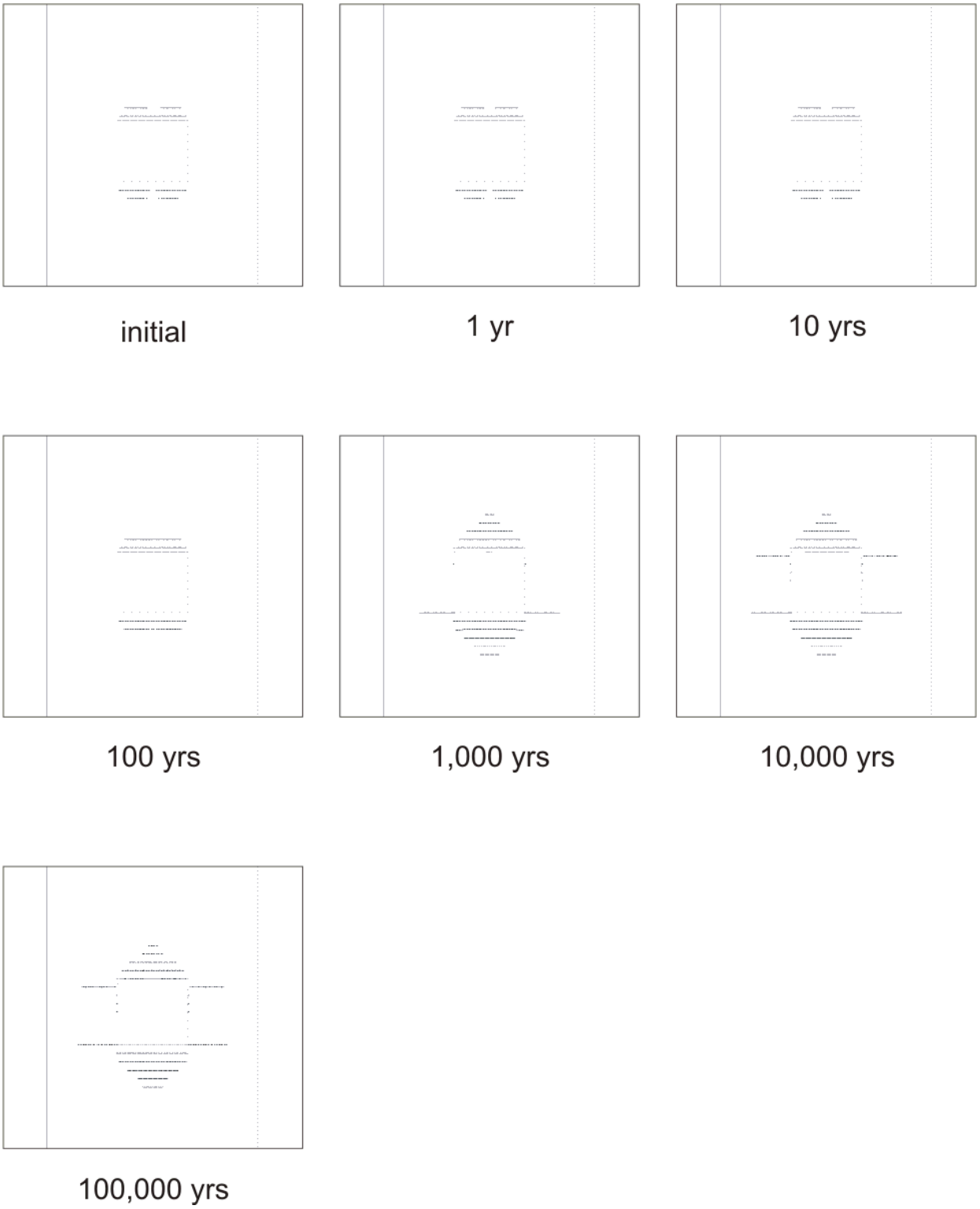

Note: Black lines indicate the locations of fractures along the bedding planes.

Figure 23. Opening of the bedding planes around a cavern in the middle of the repository due to gas pressure history Case 3

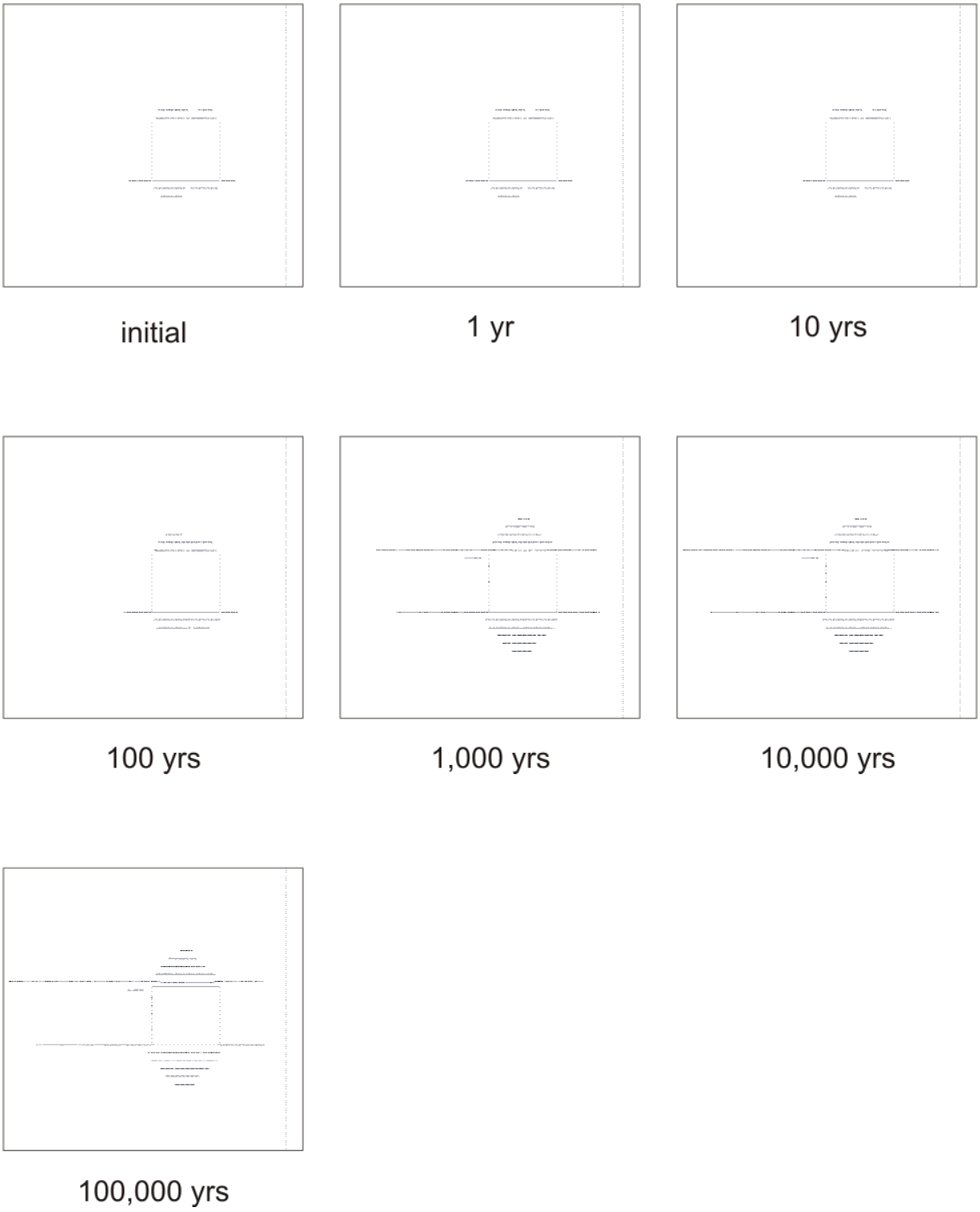

Note: Black lines indicate the locations of fractures along the bedding planes.

Figure 24. Opening of the bedding planes around a cavern at the edge of the repository due to gas pressure history Case 3

4.3 Effects of Seismic Ground Shaking

4.3.1 Seismic Ground Motions

Six ground motions were generated by seismic hazard analysis (Atkinson, 2007). Three ground motions, for the scenario event of **M**7 at a distance of 50 km, match the target uniform hazard spectra (UHS) at a 10^{-5} annual probability in the frequency range of less than 2 Hz; the other three ground motions, for the scenario event of **M**5.5 at a distance of 15 km, match the UHS in the range of frequencies greater than 2 Hz. The accelerograms for seismic ground motions for **M**5.5 at 15 km (the first scenario event) and **M**7 at 50 km (the second scenario event) are shown in Figure 25 and Figure 26, respectively. For later reference, the ground motions from the first scenario event are denoted as Ground Motions 1 through 3 (Figure 25); the ground motions from the second scenario event are denoted as Ground Motions 4 through 6 (Figure 26). Different seismic event scenarios also are listed in Table 12

Table 12. Seismic event scenarios

Scenario	Magnitude	Distance	Frequency range where it matches UHS	Ground motions
1	**M**5.5	15 km	>2 Hz	1,2,3
2	**M**7	50 km	<2 Hz	4,5,6

The duration of the ground motions from the first event scenario is approximately 3 s. The peak ground accelerations (PGAs) are in the range between 0.2 g and 0.3 g. The ground motions from the second event scenario last longer, between 12 s and 15 s, but the PGAs are lower than in the first set, generally in the range between 0.1 g and 0.2 g. The velocity histories, obtained by integration of the accelerograms, are shown in Figure 27 and Figure 28for the first and second set of the ground motions, respectively.

Each ground motion represents a single horizontal component of the motion of the ground surface. To analyze cavern stability at the OPG DGR during seismic ground motions, it is necessary to provide time histories in three orthogonal directions at the base of the model, which is at a 725 m depth below the ground surface (e.g., Figure 1). The base of the model is selected to be at the depth of 725 m, which is sufficiently far from the repository horizon (i.e., outside the range of possible inelastic deformation), but does not coincide with any geological discontinuity. It is not necessary that the model base (i.e., the bottom boundary) coincide with any geological boundary or interface. The incoming ground motions at the model base are determined accounting for the elevation of the base and the geology above and below the base. Derivation of the ground motions at the base of the model from the surface ground motions (deconvolution) is discussed in the following section. Because of the cavern's elongated shape (i.e., the length is much greater than any dimension in the cross section), and because the horizontal component of the ground motion in the direction of the long cavern's axis will have insignificant effect on cavern stability, a two-dimensional geometrical approximation is used. Consequently, only two components of ground motion are required: one horizontal (perpendicular to the cavern axis) and one vertical.

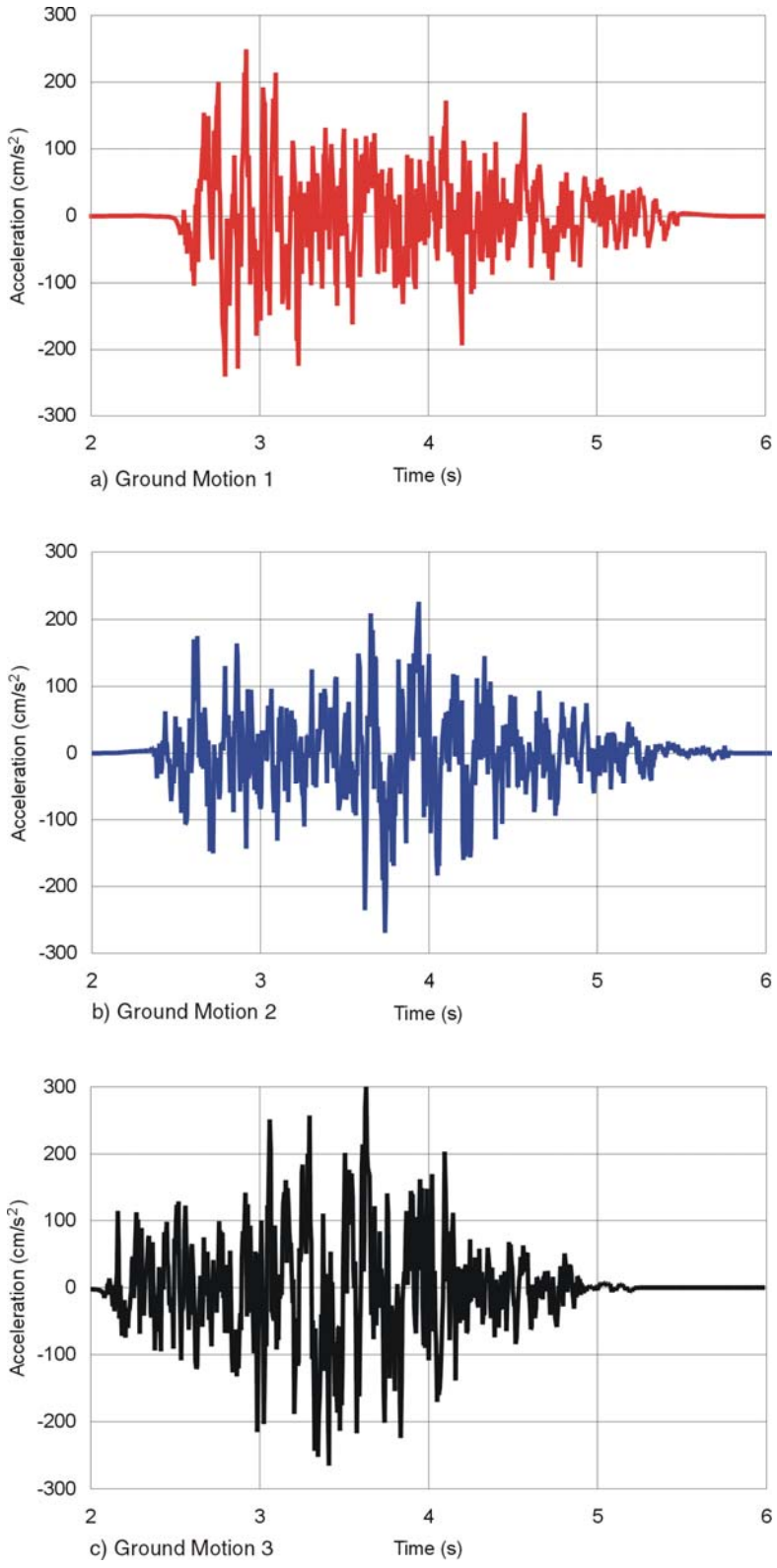

Figure 25. Generated accelerograms (horizontal component) for M5.5 at 15 km (Figure 9, Atkinson, 2007)

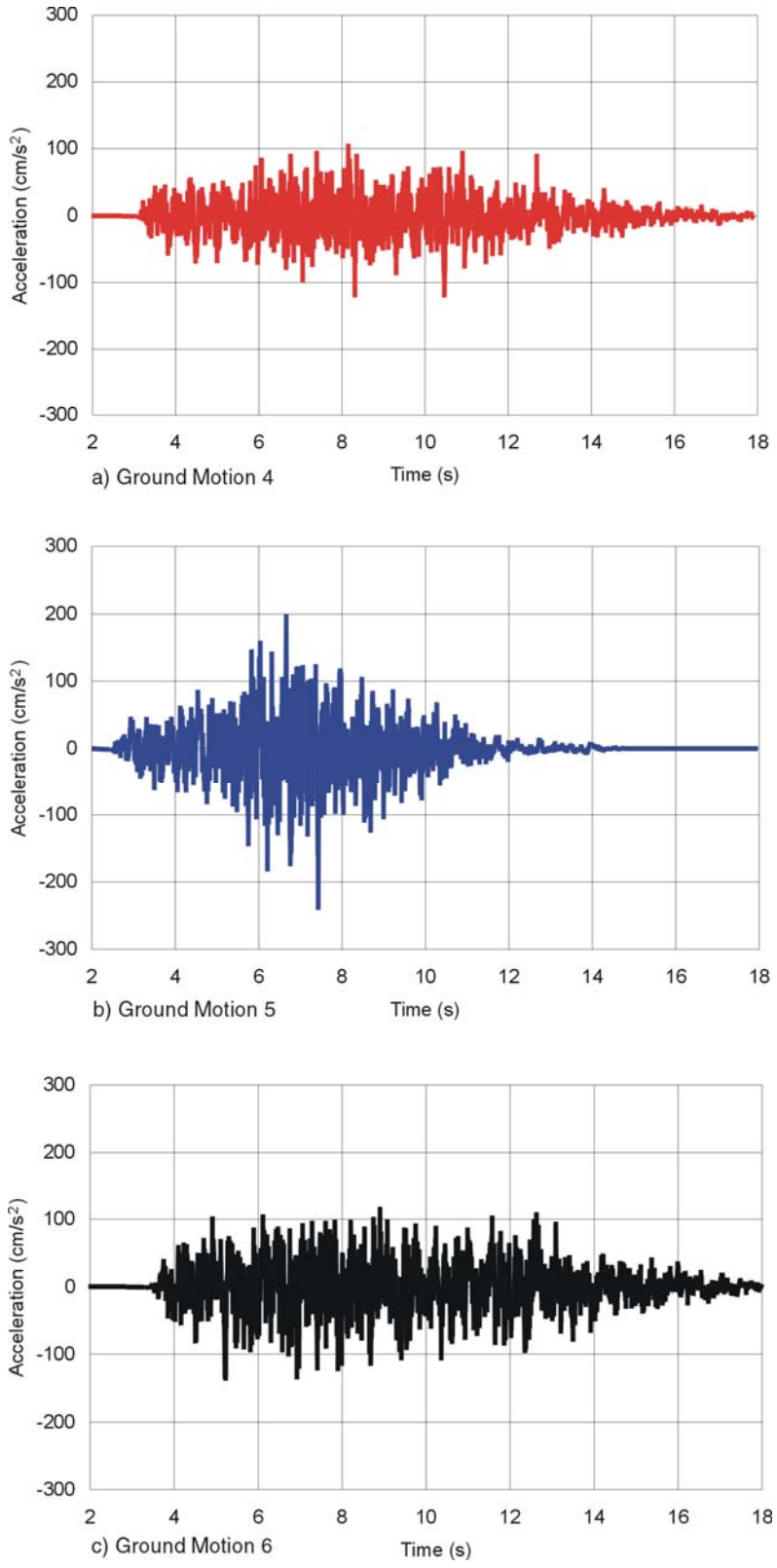

Figure 26. Generated accelerograms (horizontal component) for M7 at 50 km (Figure 10, Atkinson, 2007)

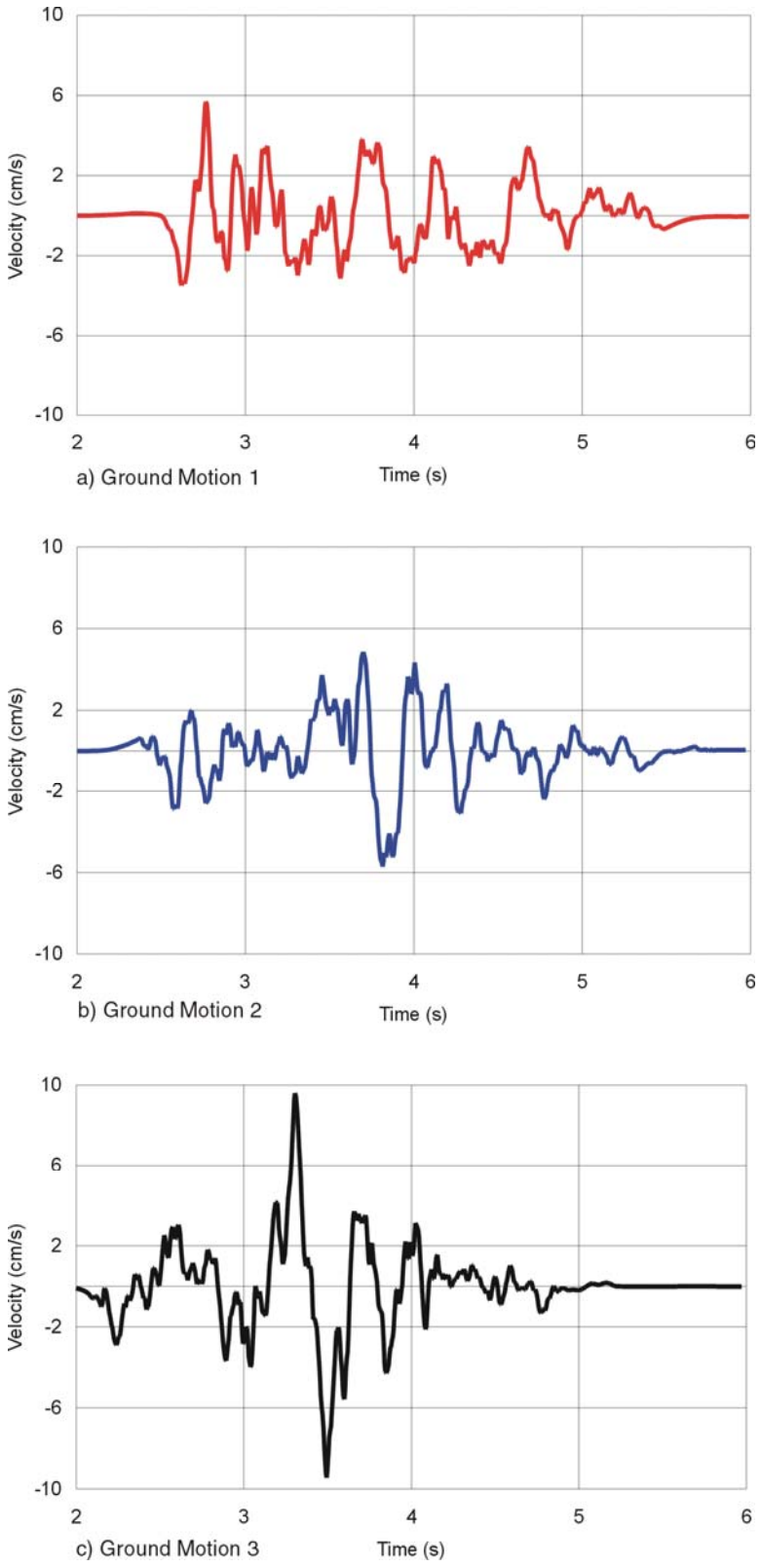

Figure 27. Ground surface velocity histories for M5.5 at 15 km calculated from the accelerograms in Figure 25

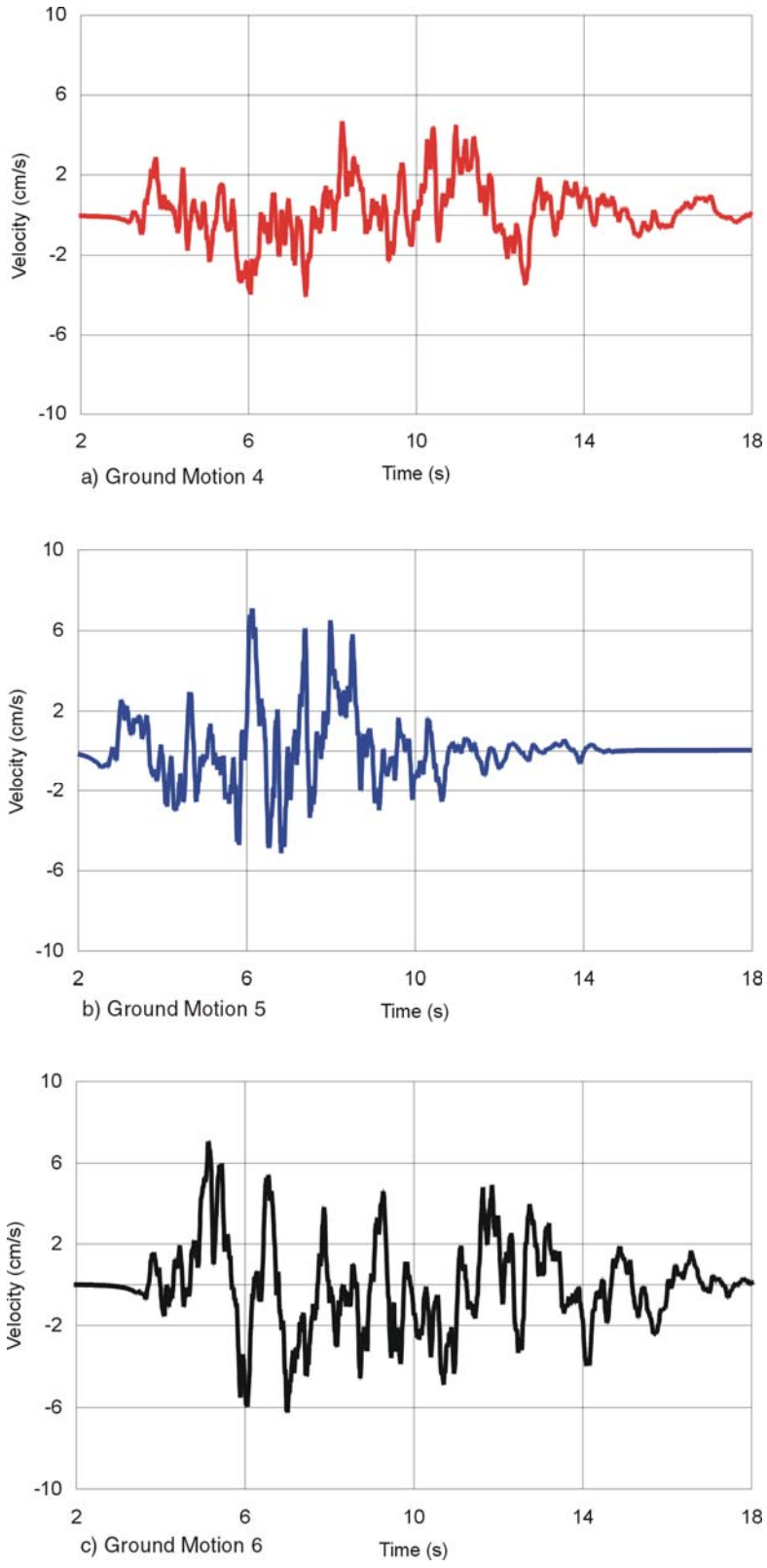

Figure 28. Ground surface velocity histories for M7 at 50 km calculated from the accelerograms in Figure 26

4.3.1.1 Deconvolution

The ground motions at the base of the model, consistent with surface ground motions, are obtained by deconvolution of the surface ground motions (Figure 25 and Figure 26). Deconvolution is carried out using the numerical code SHAKE91 (Idriss and Sun, 1992), which is based on equivalent linear analysis. The geological profile used in deconvolution is shown in Figure 29. Considering the relatively large wavelengths of interest in the analysis and the level of certainty in the geological profile (as determined from DGR-1 and DGR-2), the detail of information shown in Figure 29 is considered sufficient. The model parameters required for this analysis are shear modulus and density (or shear wave velocity), and curves that show the dependence of shear modulus and damping ratio to shear strain. Considering that such information was not available when the analysis was conducted, that relatively strong rock is present throughout the profile and that maximum strains are small (generally of the order of 0.1% or less), it was assumed that the shear modulus and damping ratio do not change as a function of shear strain. A constant damping ratio of 2% is used irrespective of the maximum strains. For example, laboratory tests on the tuff, which is also a brittle rock, show generally less than 2% of damping for strains less than 0.1% (Figure 6.2-139 in BSC, 2004b).

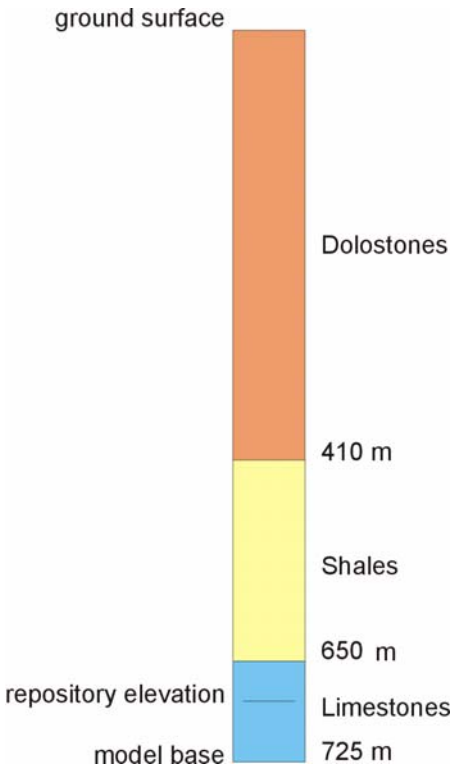

Figure 29. Profile used for deconvolution of velocities from the ground surface to the base of the model

Elastic wave velocities are estimated from the velocity tests carried out on the samples taken from DGR-1 and DGR-2 (Tables A-3 and A-4 from Intera, 2007). Sample velocities are classified to different units in the profile shown in Figure 29 based on their depth, and average values are listed in Table 13. The average wave velocities and corresponding average elastic constants are also summarized in Table 14.

Table 13. Elastic wave velocities measured on samples from DGR-1 and DGR-2 (Tables A-3 and A-4 from Intera, 2007) classified and averaged for the units in the profile shown in Figure 29

Unit	P-wave velocity C_p (km/s)	S-wave velocity C_s (km/s)
Dolostones 0 – 410 m	5.97	2.91
	5.28	2.78
	5.72	2.96
	3.86	2.46
	3.56	2.00
	4.29	2.21
	4.23	2.40
	4.04	1.98
	3.14	1.97
	4.20	1.99
	4.93	2.49
	5.55	2.71
	5.51	2.84
average	**4.64**	**2.44**
Shales 410 m – 650 m	2.54	1.05
	4.83	2.65
	3.87	2.03
	1.94	0.92
	4.16	2.33
	4.25	2.34
	3.94	2.29
	4.85	3.21
	4.48	2.39
	5.66	3.30
	3.99	1.95
	3.29	1.93
	3.34	1.85
	3.18	1.70
	1.95	0.67
average	**3.75**	**2.04**
Limestones 650 m – 725 m	4.53	2.65
	3.59	1.55
	5.94	3.15
	5.70	3.13
	5.43	2.81
	5.35	2.75
	4.95	2.65
	5.41	2.99
	5.46	2.95
	4.79	2.64
	4.59	2.62
	4.25	2.38
	5.51	2.70
	5.95	2.91
	5.30	2.85
	3.49	1.80
	4.38	2.07
	2.73	1.59
	4.43	2.72
average	**4.83**	**2.57**

Note: Although the test results are lumped to the units identified in Figure 29, they could have been obtained on samples from different geological units. For example, some of the results classified as dolostones (0-410 m) are from the intervening shales or anhydrates.

Table 14. Average wave velocities and dynamic elastic constants for the units from profile shown in Figure 29

	C_s (m/s)	C_p (m/s)	G (GPa)	K (GPa)	E (GPa)	ν
Dolostones	2440	4640	16.07	58.13	42.08	0.31
Shales	2040	3750	11.24	37.97	28.99	0.29
Limestones	2570	4830	17.83	62.99	46.46	0.30

The elastic constants are derived from the wave velocities using the following relations:

$$K = \rho\left(C_p{}^2 - \frac{4}{3}C_s{}^2\right)$$
$$G = \rho C_s{}^2 \quad (13)$$

where K and G are bulk and shear moduli, respectively; and C_p and C_s are P- and S-wave[4] velocities, respectively. The Young's modulus, E, and Poisson's ratio, ν, are calculated from bulk and shear moduli using standard relations from the linear theory of elasticity. Measurements of wave velocities on small samples (75 mm in diameter) in the laboratory are not necessarily representative of the large-scale, in-situ wave velocity, which is required for this analysis. However, because measurements on small-scale samples overestimate rock mass velocity, while unconfined laboratory conditions underestimate velocity under an in-situ stress state, it is assumed that the two effects balance each other; hence, the values from Table 14 were used in deconvolution.

In order to verify and validate deconvolution, the incoming, deconvoluted Ground Motion 3 at the base of the model is propagated through the profile shown in Figure 29. The one-dimensional wave propagation is simulated using the numerical code *FLAC* (Itasca, 2005). The horizontal history of the ground surface generated in the *FLAC* simulation is compared with the ground surface velocity used as the input to deconvolution (i.e., the velocity we started with, Ground Motion 3 from Figure 27) in Figure 30. Considering that the Rayleigh damping used in these *FLAC* simulations overdamps frequencies greater than 6 Hz (i.e., those frequencies are damped more than 2%), the comparison is good, which confirms that the deconvolution was carried out properly.

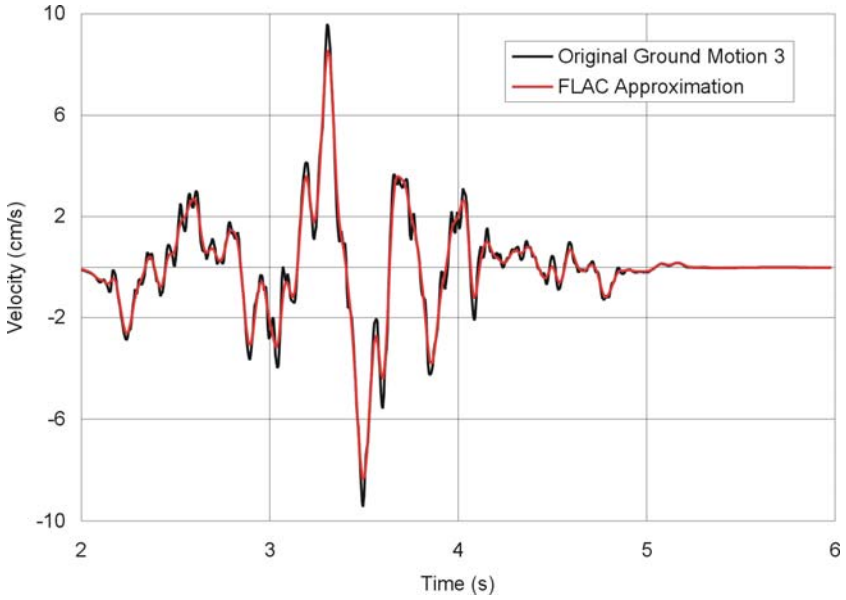

Figure 30. Comparison of the ground-surface velocity history calculated using FLAC for the deconvoluted incoming ground motion at the model base with the original time history for Ground Motion 3

4. P-wave is the compressional wave; S-wave is the shear wave.

The deconvoluted velocity histories (within the rock mass—i.e., including the reflections from the ground surface and the interfaces) at a 725 m depth are shown in Figure 31 and Figure 32. Comparing the velocities at the ground surface (Figure 27 and Figure 28) with those at the model base (Figure 31 and Figure 32) indicates that, as expected, the velocities at the base are between 50% and 100% of the velocities on the ground surface. There is a ratio of two between velocities on the ground surface and velocities at depths greater than the depth of surface amplification, which is approximately 25% of the wavelength, when there is no material damping. The ratio obtained here is less because of the assumed 2% material damping and relatively small repository depth compared to the dominant wavelengths of the analyzed ground motions (i.e., the repository is within the region of the surface amplification).

4.3.1.2 Simulated Ground Motions

The velocity histories used in the cavern stability analysis are shown in Figure 33 and Figure 34. Only one set of ground motions was analyzed for each scenario event. Because the PGV is an earthquake intensity measure that best correlates with tunnel damage[5], the horizontal components (for each scenario event) were selected as the velocity histories with the greatest peak ground velocity (PGV) from the set of three histories generated for each scenario event. Thus, for the event **M**5.5 at 15 km, Ground Motion 3 (Figure 31) was used as the horizontal component of the motion. Similarly, for the event **M**7 at 50 km, Ground Motion 5 (Figure 32) was used as the horizontal component of the motion.

The vertical ground motions were not generated as part of the seismic hazard analysis. In order to analyze cavern stability using the set of seismic ground motions that include both horizontal and vertical components, the vertical components were selected from the available horizontal ground motions. The vertical components (for each scenario event) were selected as the velocity history with second greatest PGV from the set of three histories generated for each scenario event. Thus, for the event **M**5.5 at 15 km, Ground Motion 2 (Figure 31) was used as the vertical component of the motion, and Ground Motion 6 (Figure 32) was used as the vertical component of the motion for the event **M**7 at 50 km. The empirical relations between the intensities of the vertical and horizontal components of the ground motion for eastern North America indicate that the ratio should be between 0.67 and 1. For conservatism, the vertical component was not rescaled in these analyses. The vertical velocity histories are translated in time sufficiently to ensure that the P-wave arrives earlier than the S-wave.

5. *Considering the wave speed of the order of 2 km/s and that most of the energy is in the frequency range of less than 10 Hz, the wavelengths will be greater than 200 m. Because the cavern characteristic dimension in cross-section is much less than the wavelength, the tunnels will behave during seismic ground motion as if subjected to a sequence of static stress states. Because the magnitude of seismically induced stresses is proportional to the velocity, the PGV is the seismic intensity measure that best correlates to seismically induced damage around tunnels.*

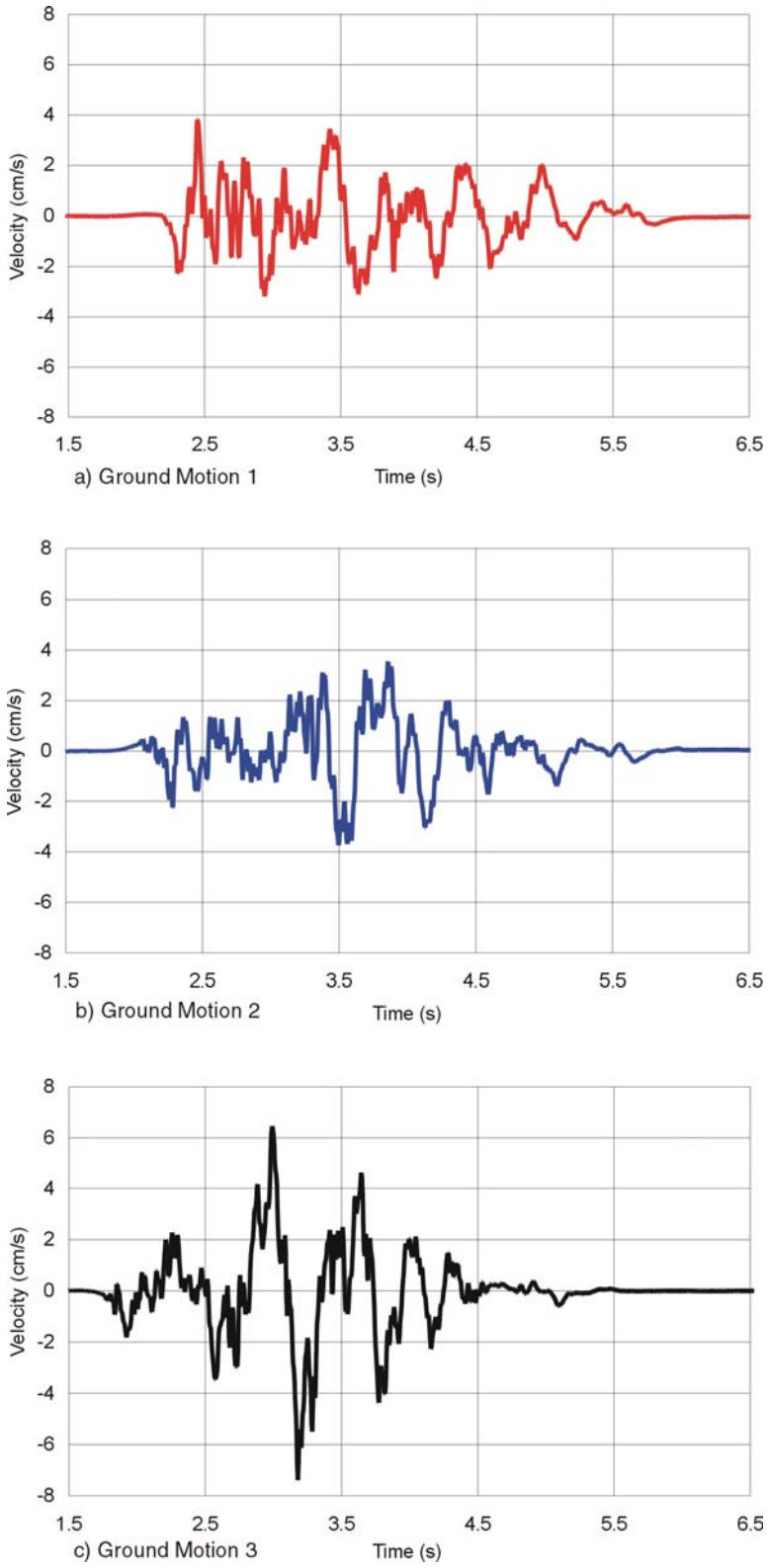

Figure 31. Velocity histories at the model base (725 m depth) for M5.5 at 15 km obtained by deconvolution of the ground surface histories (Figure 25 and Figure 27)

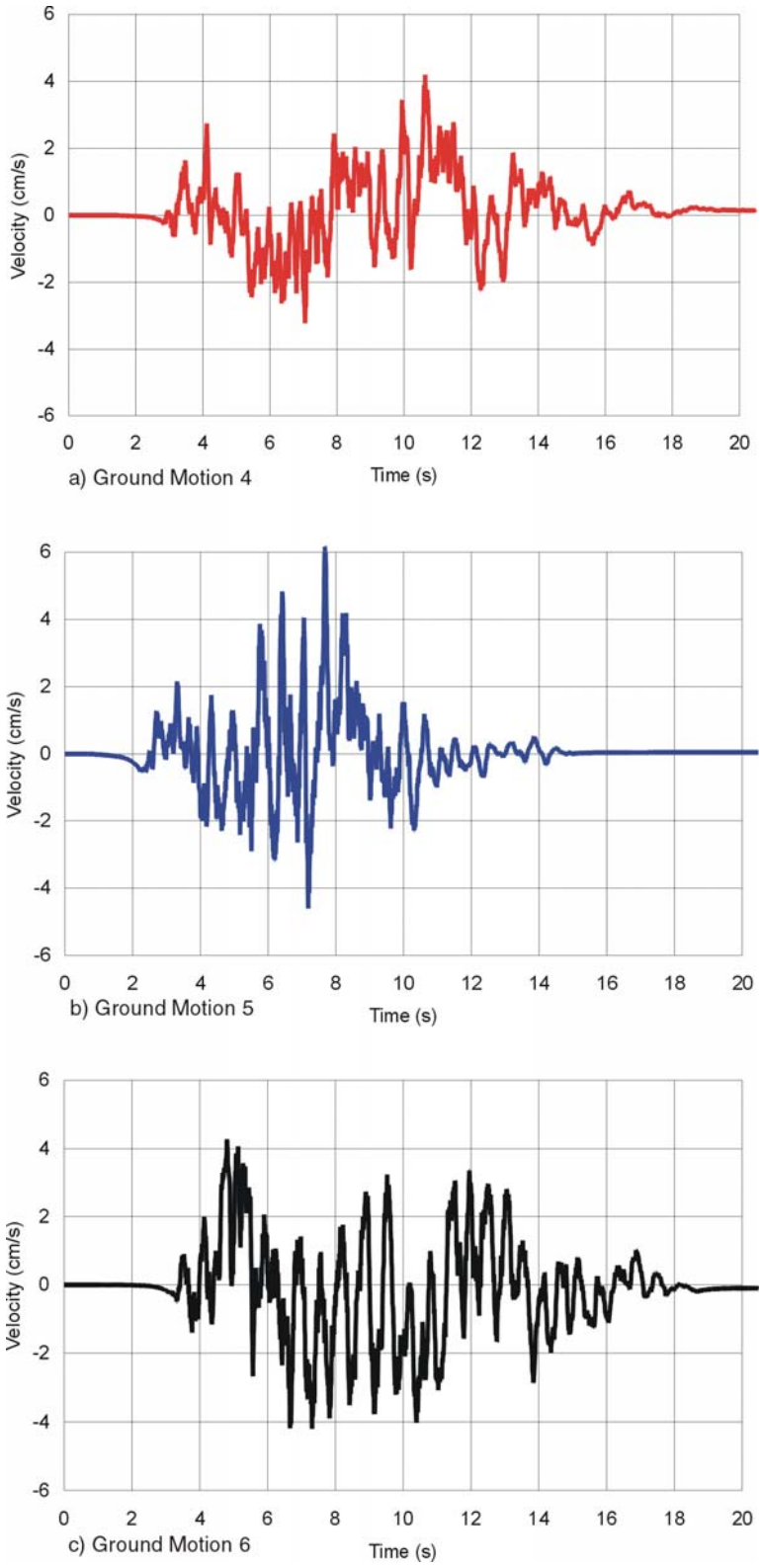

Figure 32. Velocity histories at the model base (725 m depth) for M7 at 50 km obtained by deconvolution of the ground surface histories (Figure 26 and Figure 28)

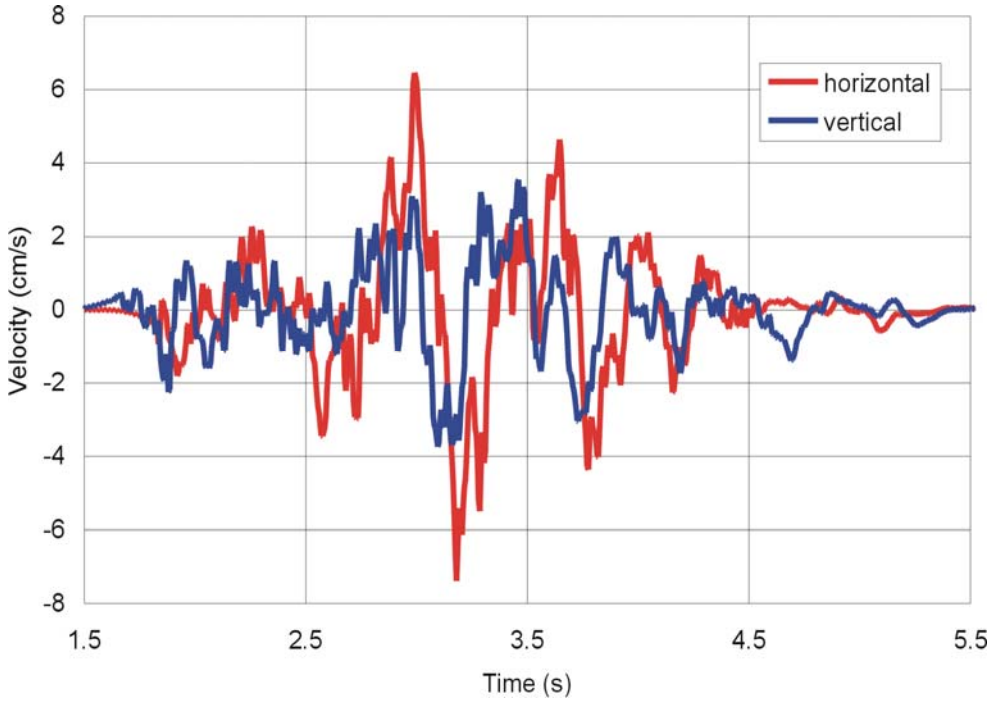

Figure 33. Horizontal and vertical components of seismic ground motion at the base of the model representative of M5.5 at 15 km used for cavern stability analysis

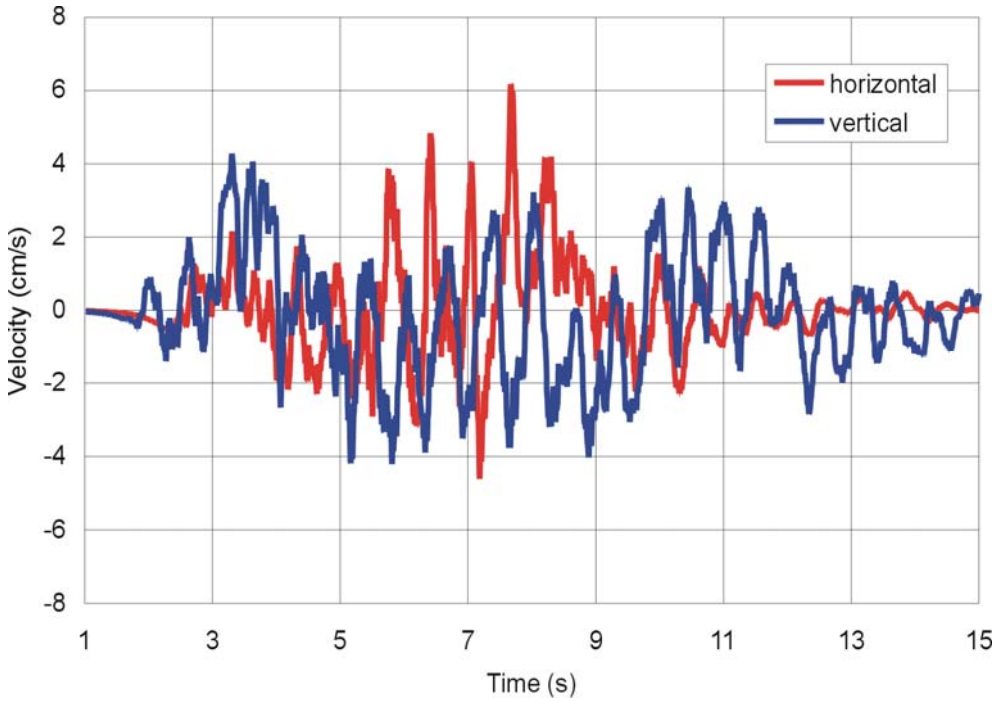

Figure 34. Horizontal and vertical components of seismic ground motion at the base of the model representative of M7 at 50 km used for cavern stability analysis

4.3.2 Geometry and Boundary Conditions for Dynamic Analysis

Different model geometry and boundary conditions than those described in Section 2.1 are used for the dynamic analysis. The geometry of the model used for the dynamic analysis of caverns subjected to seismic shaking is shown in Figure 35. The model is extended laterally to include one more cavern on each side of the cavern of interest. Only rock around the middle cavern in the model is discretized with the Voronoi blocks. Two surrounding caverns are included only to provide correct stress conditions for the middle cavern, because stress and displacement symmetry conditions along the vertical plane half-way between the caverns are not preserved during seismic ground shaking. At the bottom and the top of the model, the viscous boundaries are applied in both normal and tangential directions. Those boundary conditions prevent outgoing elastic waves from being reflected from the artificial model boundaries (included to make the model size finite) back into the model (as it would happen in the case of velocity or stress boundary conditions). Although the model does not extend to the ground surface and viscous boundary conditions were used on the top model boundary, the effect of the ground surface is accounted for because the ground motions applied at the base of the model, shown in Figure 33 and Figure 34, already include reflections from the ground surface. The seismic ground motion actually is applied as a stress boundary condition, because the viscous boundary conditions used at the model bottom are not compatible with fixed boundaries (or boundaries along which velocities are prescribed). The following relation is used to calculate the stresses equivalent to velocities:

$$\begin{aligned} \tau_{vh} &= 2\rho C_s v_h \\ \sigma_v &= 2\rho C_p v_v \end{aligned} \tag{14}$$

where τ_{vh} is the shear stress at the bottom boundary of the model, σ_v is the vertical stress, ρ is the density, C_s and C_p are S- and P-wave velocities, respectively, and v_h and v_v are horizontal and vertical velocities, respectively. Equations (14) are similar to a relation between velocities and the stresses for plane waves in an infinite medium. The factor of two is a correction added because of the viscous boundaries that dissipate half of the applied energy. The free-field boundaries, shown (in Figure 35) as vertical bars parallel with the model vertical boundaries, represent the stresses and deformation of the truncated semi-infinite domains on the left and right sides of the model. The free fields perform simple one-dimensional wave propagation. Viscous boundary conditions also are placed between the main model domain and the free fields.

The geological materials (e.g., soils and rocks) dissipate energy during cycling at all levels of shear strain. On the other hand, the constitutive models dissipate energy only when the strains exceed the yielding strain. Energy dissipation during cycling at relatively low strain amplitudes is accounted for through material damping, which, in the case of geological materials, is hysteretic, or frequency independent, and typically in the range between 2% and 5% of the critical damping[6]. The superposition of mass- and stiffness-proportional damping, called Rayleigh damping, provides hysteretic, frequency-independent damping over a certain frequency range. The problem with the Rayleigh damping is that it imposes severe restrictions on the stable calculation timestep, making it more than 10 times shorter for typical damping ratios than in the case without Rayleigh damping. To avoid the excessively long simulation times and ensure that calculations are conservative, the simulations were carried out using very little damping, approximately 0.3% of the critical damping.

---

6. Although the magnitude of damping depends on the material properties and on the shear strain amplitude, a typical estimated constant damping ratio is used throughout simulation, irrespective of strain amplitudes.

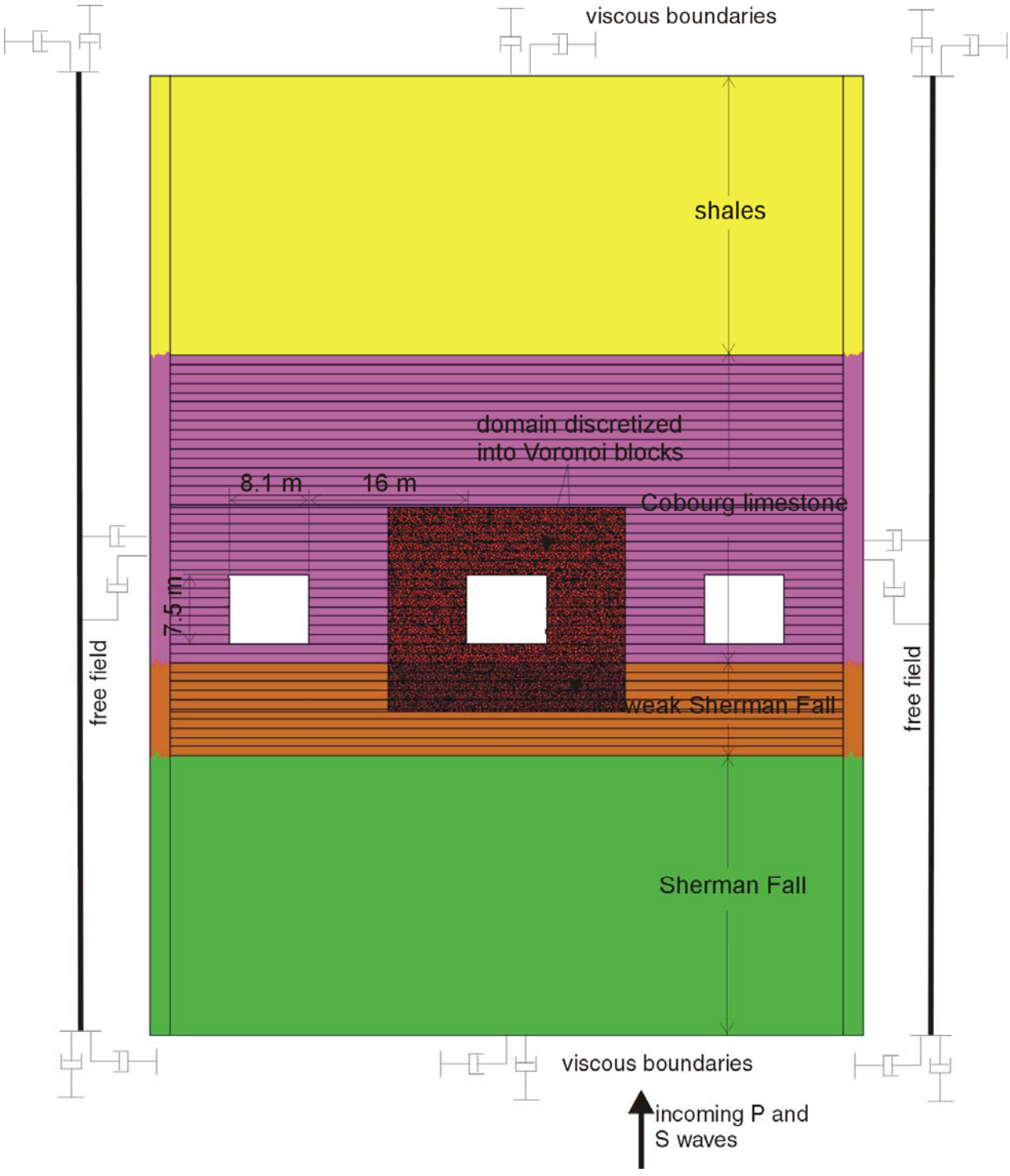

Note: Colors correspond to different model materials (as denoted in Figure 4)

Figure 35. Geometry and boundary conditions of the model used in dynamic analysis

4.3.3 Case Studies of Tunnel Performance During Earthquakes

Dowding and Rozen (1978) studied 71 cases of the extent of tunnel damage during earthquakes. They summarized their results in two charts showing the dependence of damage to peak ground acceleration (PGA) and PGV. The latter correlation is reproduced in Figure 36. They classify the extent of damage in three categories: no damage, minor damage, and damage. The chart indicates that no damage is expected in the tunnels for PGVs less than 20 cm/s. Because the PGVs of all ground motions considered here are less than 10 cm/s (Figure 27 and Figure 28), it is not expected that ground motion will cause damage to the caverns at the OPG DGR.

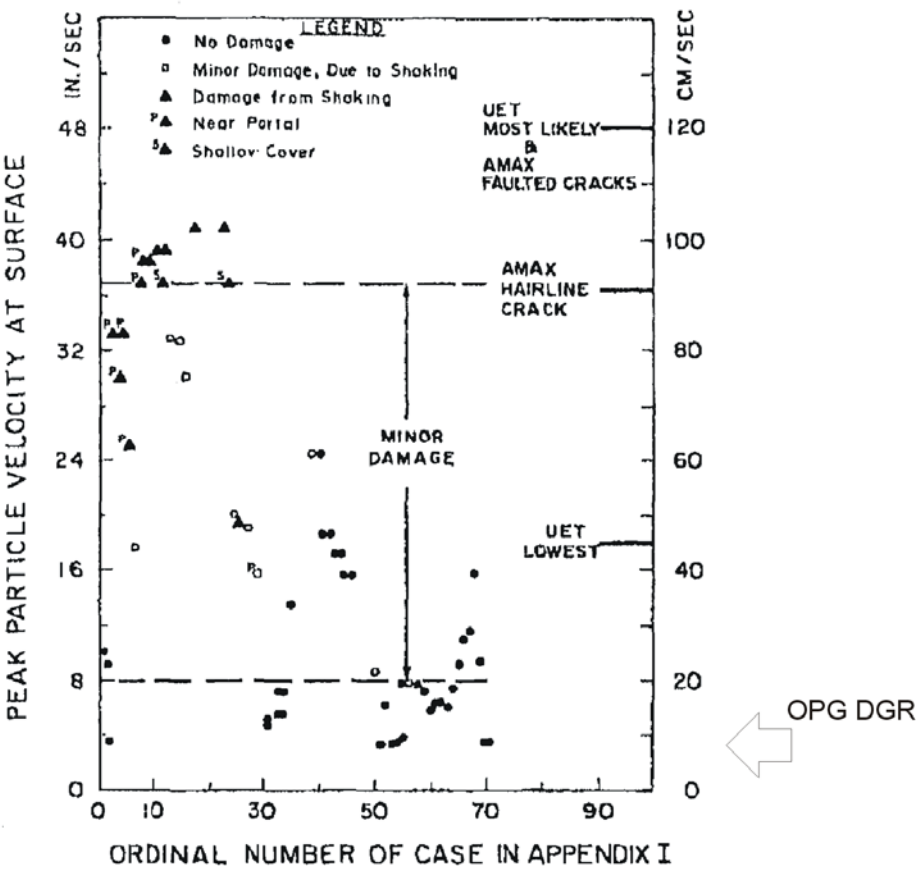

Note: The arrow indicates approximate PGV level at OPG DGR.

Figure 36. Calculated peak particle velocities and associated damage observations: earthquake and explosive shaking (Figure 4 from Dowding and Rozen, 1978)

4.3.4 Results of Dynamic Simulations

The strength of the stressed rock mass around the caverns will degrade with time, resulting in an evolution of damage, the extent of which will increase gradually (Section 4.1). Consequently, the effect of seismic ground shaking on cavern stability possibly could depend on the time after

excavation when the cavern is subjected to seismic shaking. In order to bound possible cavern responses, the analyses of seismic shaking were carried out for two initial states: 1) immediately after cavern excavation, and 2) 100,000 years after excavation. The analysis presented in Section 4.1 has estimated that the rock mass in the latter state has accumulated the damage in 100,000 years, as illustrated in Figure 38a. Each initial state is simulated for two sets of ground motions, shown in Figure 33 and Figure 34, for two event scenarios. The results of the simulations are shown in Figure 37 and Figure 38 for the initial states after cavern excavation and 100,000 years of time-dependent strength degradation.

As expected based on empirical data (Section 4.3.3), the considered ground motions do not cause any additional damage or rockfall if they occur while there is no significant pre-existing damage around excavations, which is certainly the case immediately after excavation. Figure 37a shows cavern configuration and rock damage (fractures shown as red lines) immediately after excavation. There is an indication of fracturing along the bedding planes in the cavern crown and the floor. States after shaking by two different seismic events, shown in Figure 37b and Figure 37c, illustrate no additional damage compared to the initial state.

When there is a significant extent of damaged rock mass around the cavern (Figure 38a), seismic loading shakes down most of the damaged rock from the crown. Already fractured rock mass, in the state of limit equilibrium, is loosened by shaking and falls on the cavern floor under gravity. The breakout propagates 5.5 m from the original cavern crown. Insignificant additional damage is observed in the rock mass, mainly extending damage along the bedding planes in the cavern crown due to cantilevering of some of the slabs after loose rock falls. These analyses might overpredict the extent of the seismically induced rockfall because of the low damping ratio (approximately 0.03%) used, compared to typical damping ratios, which are in the range between 2% and 5%. (Numerical simulation of an earthquake using 2% to 5% of Rayleigh damping would make the calculation timestep 2-3 orders of magnitude shorter than in the simulations reported here and simulation times prohibitively long.)

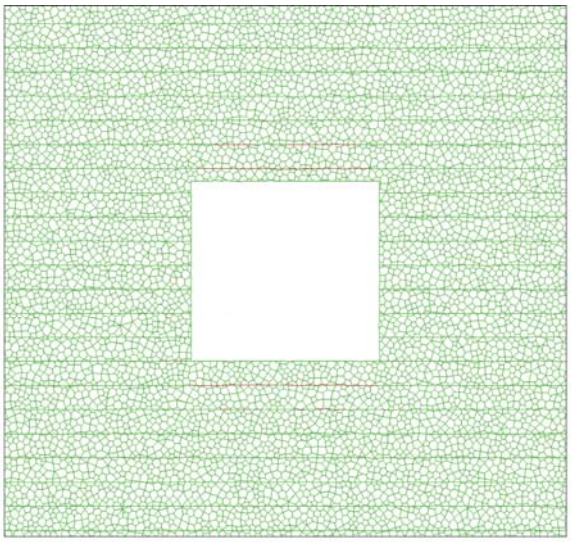

a) initial state after cavern excavation

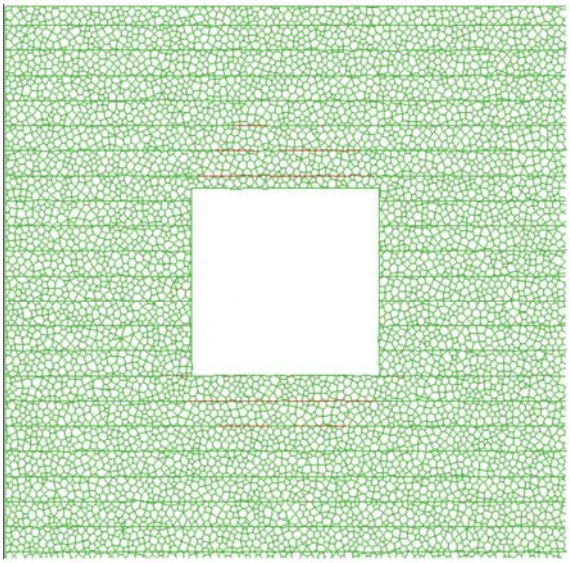

b) ground motion M5.5 at 15 km

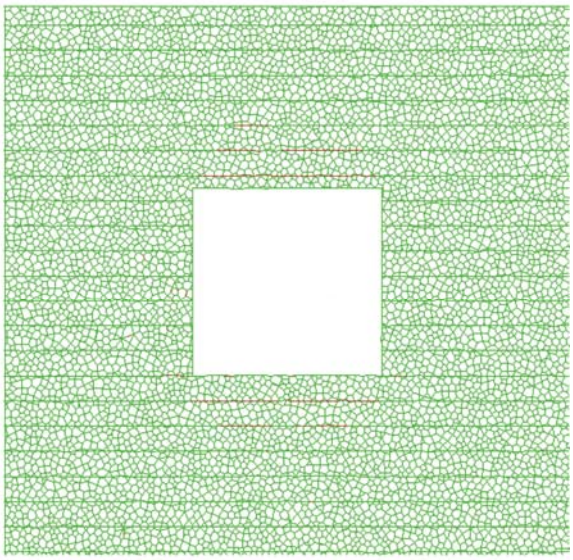

c) ground motion M7 at 50 km

Note: Red lines indicate locations of fractures.

Figure 37. Effects of seismic ground motions immediately after cavern excavation

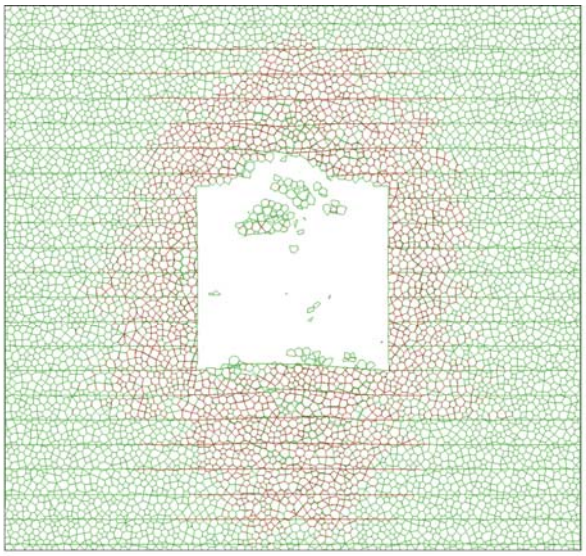

a) initial state after 100,000 years

b) ground motion M5.5 at 15 km

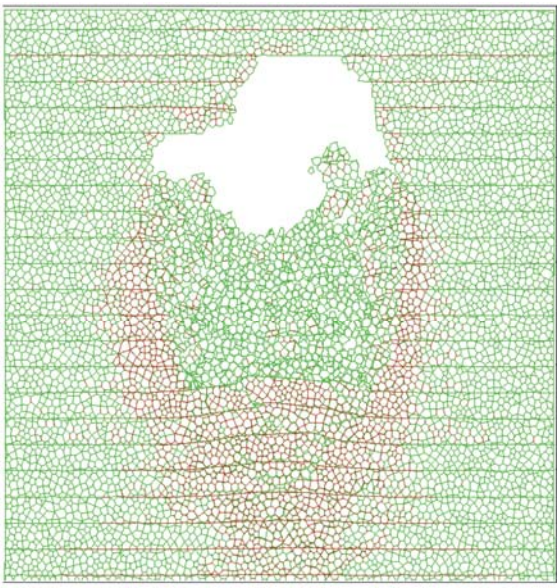

c) ground motion M7 at 50 km

Note: Red lines indicate locations of fractures.

Figure 38. Effects of seismic ground motions after 100,000 years of time-dependent strength degradation

4.4 Effects of Glacial Loads

4.4.1 Evolution of Glacial Loads

The northern portion of North America has been subjected to glacial events over the past million years. These events, which occur periodically, are associated with the development of the ice sheet covering certain portions of the Earth's surface. Over southern Ontario, where the OPG DGR is planned, the maximum ice thickness could have exceeded 2.5 km during the most southerly ice sheet advance (Peltier, 2008). The University of Toronto Glacial Systems Model (UofT GSM), which is a model of continental-scale glaciation events, was used by Peltier (2008) to develop a description of glaciation of the Canadian Shield as a means of assessing the impact that such an event would have on performance of the OPG DGR. Eight possible realizations of glaciation and deglaciation during the last 120,000 years that provide acceptable fits to the observed constraints were developed.

The importance of these models to cavern stability assessment lies in how the formation of the ice sheet will affect loads on the repository—i.e., the stresses in the rock mass at the repository level. The weight of the ice sheet will increase both vertical and horizontal normal stresses. Furthermore, as the ice sheet moves, sliding at a relatively low rate, it will impose additional shear stresses on the ground surface. The current analysis (Peltier, 2008) does not provide the shear stresses. The effect of glacially induced shear stresses on cavern stability will be analyzed in Phase II of the project. The evolution of vertical normal stresses at the repository location over the last 120,000 years for four analyzed realizations, as taken from Figure 13 of Peltier (2008), is shown in Figure 39. The greatest vertical stress (almost 30 MPa) takes place for realization nn9904.

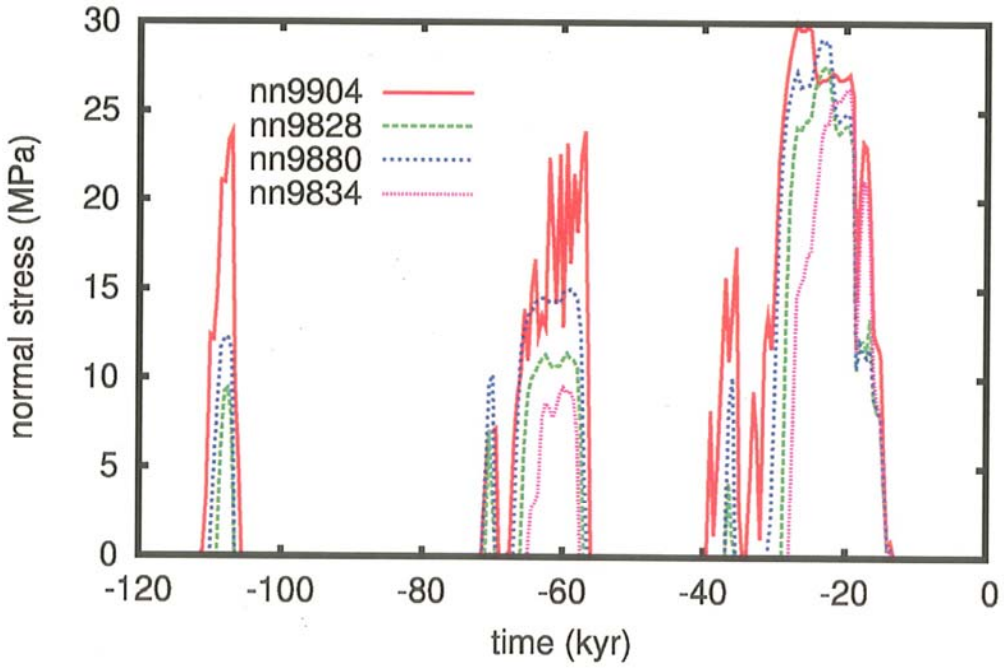

Figure 39. Four analyzed realizations of normal stress due to an ice sheet at the surface of the Earth at the repository site (Peltier, 2008)

The conditions for the next advance of continental scale glaciation will not be favourable for approximately another 60,000 years (Peltier, 2008). However, predictions of possible variations of the ice load during future glaciations are not available. Instead, the repository is analyzed for one of the eight realizations in the previous 120,000 years that resulted in the greatest ice load— i.e., nn9904. (The pressure history for nn9904 is shown in Figure 39.) Because maximum ice load is the critical factor and because the load must vary gradually (i.e., if the maximum pressure of 29.7 MPa[7] were applied instantaneously, it would cause inertial effects in the path-dependent, nonlinear model), only one glacial episode (with the greatest pressure) starting after 60,000 years was simulated. Thus, the entire pressure history as shown in Figure 39 was not simulated. The simulated history of the glacially induced normal stress is shown in Figure 40.

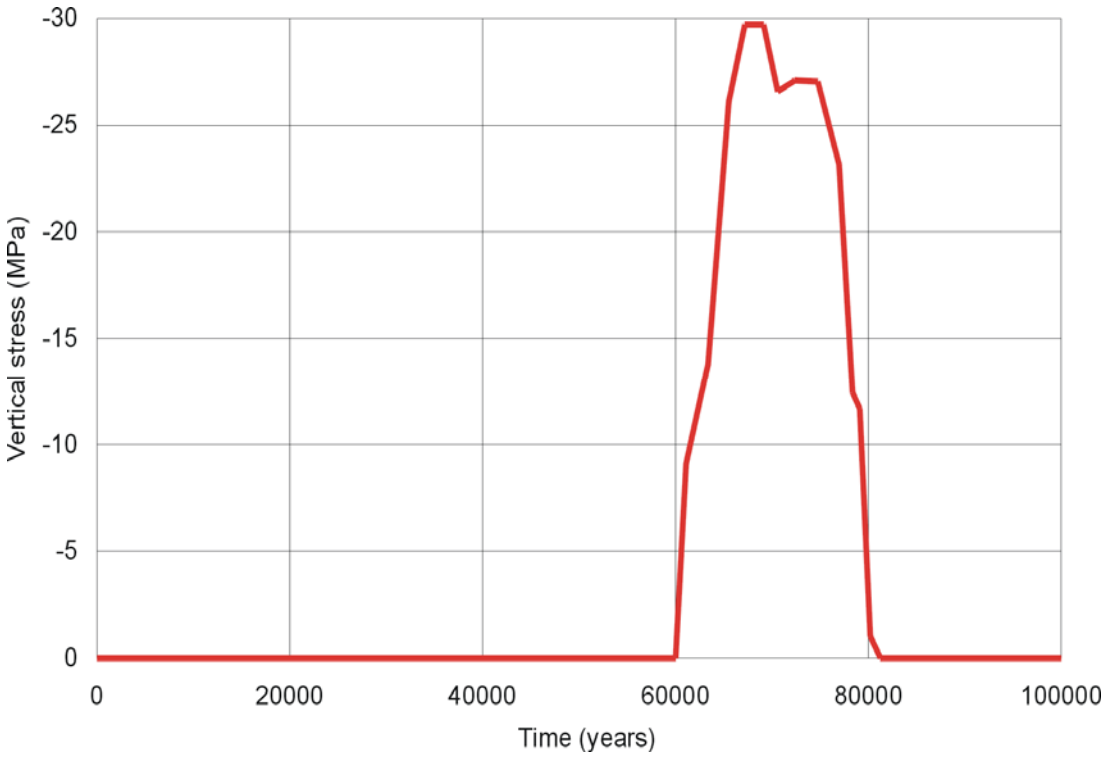

Figure 40. Simulated evolution of ice sheet load in the cavern stability analysis

4.4.2 Results of Glacial Load Simulations

The results of the analysis for the glacial load cycle are shown in Figure 41. The figure includes three states of the model: 1) at the beginning of glacial load cycle (60,000 years), 2) at the time maximum vertical load is achieved (69,130 years), and 3) at the end of the glacial load cycle, when the ice load returns to zero (81,250 years). Two plots are included for each state: the extent of damage (fracturing) on the left, and contours of vertical stress on the right.

7. The magnitude of 29.7 MPa is obtained by scanning Figure 39. Actual digital data were not available.

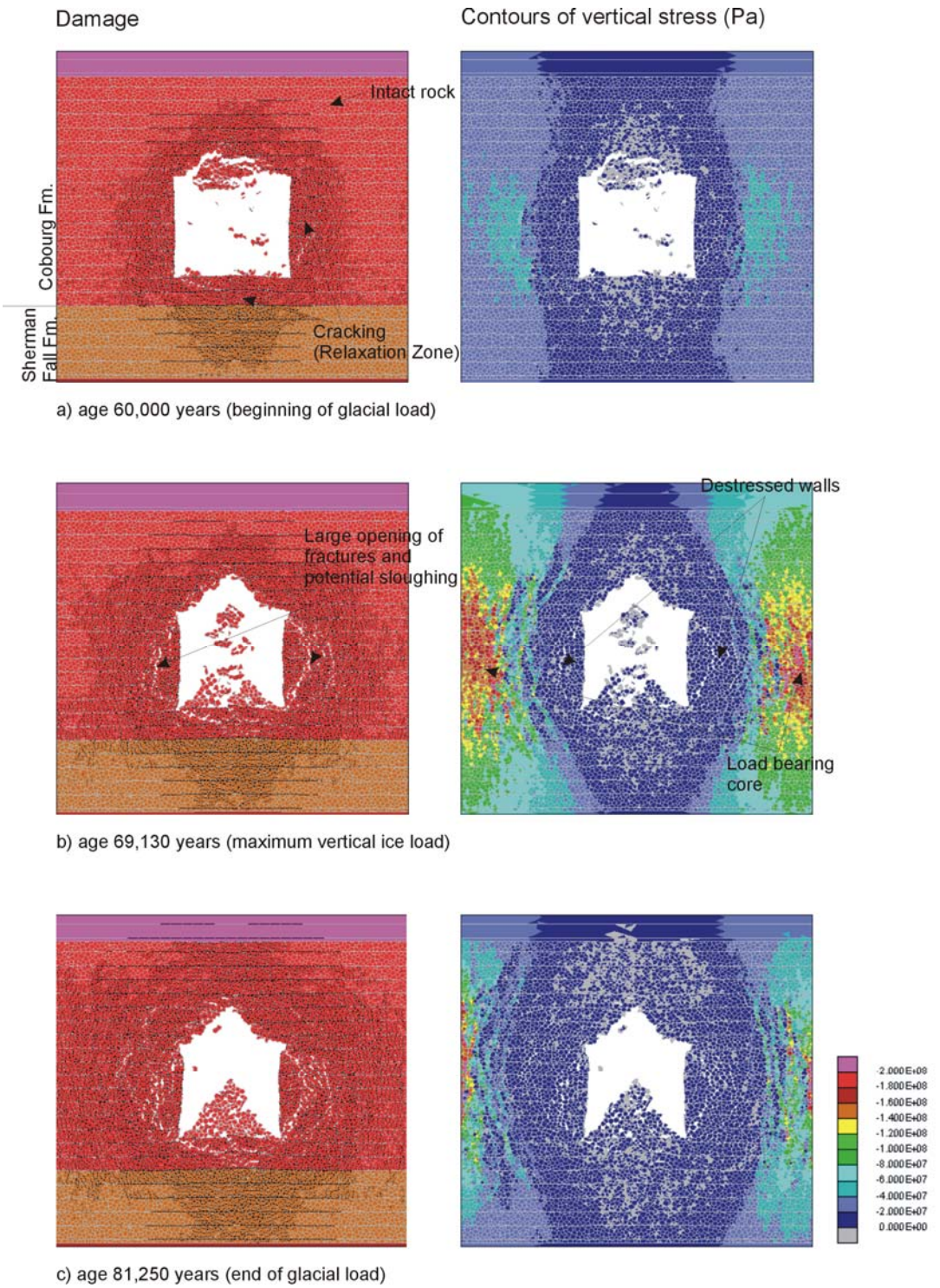

Note: In the damage plots (left column) different colours represent different regions of the material. Cobourg limestone is pink; Cobourg limestone discretized into Voronoi blocks is red; weak Sherman Fall limestone discretized into Voronoi blocks is brown. Black lines represent locations of the fractures. Coloring in the plots shown in the right column is based on contouring of the vertical stress magnitude. The stress magnitude scale (Pa) is provided.

Figure 41. Evolution of damage and vertical stresses (Pa) around a cavern during a glacial cycle

Damage in the rock mass increases with increase in the ice load. As expected, the ice load increases stresses in the pillars between the caverns. When the ice load reaches a maximum of 29.7 MPa, the pillar is fractured throughout its thickness. Large deformations in the cavern wall indicate possible sloughing of loose rock up to 2 m to 3 m in the middle of the pillar height. Vertical stress contours are in agreement with damage and deformation. The 8 m thick pillar core carries stresses in excess of 150 MPa. Confinement in the middle of relatively wide pillars (width-to-height ratio greater than 2.0) is the reason that the pillar core can sustain such stresses. Consequently, the pillar remains stable even when the maximum ice load is achieved. The damage in the crown results in the breakout that extends to approximately 3 m above the crown. The breakout was approximately 1.5 m in the initial stage. However, when the peak vertical stress is reached, the extent of damage in the cavern crown and floor do not increase much compared to the state before the glacial loads were added (Figures Figure 41a and Figure 41b).

As the glacial load decreases to zero, the pillars unload. However, some of the horizontal stresses induced during the loading process and the generally inelastic deformation of the rock mass will remain locked-in even after unloading, resulting in additional damage, particularly in the cavern crown and floor.

Considering the uncertainties of the analysis, these results are put into perspective. The stress in the pillar between the caverns, when the maximum glacial load is achieved, is compared with different empirical failure curves for the hard-rock pillars (Martin and Maybee, 2000). The curves provide the average stress (scaled with intact rock UCS) at which a pillar fails as a function of width-to-height ratio.

The extraction ratio at the OPG DGR is

$$e_r = \frac{8.1}{16.0 + 8.1} = 0.34 \tag{15}$$

Considering that the in-situ vertical stress is 18.3 MPa (Section 2.1) and the maximum glacial stress increase is 29.7 MPa, the average pillar stress, σ_p, is

$$\sigma_p = \frac{\sigma_v}{1 - e_r} = \frac{18.3 + 29.7}{0.66} = 73\,\text{MPa} \tag{16}$$

Thus, the scaled average pillar stress, σ_p / UCS, is

$$\frac{\sigma_p}{UCS} = \frac{73}{110} = 0.66 \tag{17}$$

Based on testing of DGR-2 rock core (Intera, 2007), intact rock UCS, on small-scale sample (75 mm in diameter), is 110 MPa. This value of UCS does not account for time-dependent strength degradation. Because the empirical pillar-strength relations and curves do not include explicitly in-situ rock mass jointing (e.g., using some form of rock mass classification), it was not considered necessary to account for time-dependent damage in this kind of approximate

analysis. However, pillar strength and stress-strain response will change as a function of time and time-dependent strength degradation. Because the cavern height is 7.5 m and pillar width is 16 m, the width-to-height ratio is

$$\frac{w}{h} = \frac{16}{7.5} = 2.1 \tag{18}$$

The empirical curves and the average pillar stress at the OPG DGR when the maximum ice load is reached are shown in Figure 42. Although there is some variability in predictions by different empirical relations, the average pillar stress is above most of the curves, implying pillar failure. Despite the fact that some empirical curves extend to $w/h = 3.0$, the uncertainty in the predictions of the empirical curves for $w/h > 2.0$ is significant, because there are only a few observations of pillar failures when $w/h > 2.0$. The empirical curves probably underestimate the strength of the squat pillars ($w/h > 2.0$), which, in most rocks, exhibit continuously hardening behaviour due to the high level of confinement in the pillar core. Hardening means that even after the pillars yield (or reach the "peak strength"), the pillar stresses continue to increase in response to straining. The tangent stiffness after the pillar yields is usually at least one order of magnitude less than the tangent stiffness before the yield, but the overall pillar response is continuously hardening. Therefore, the model prediction that the pillar will remain stable during the ice load cycle is not really contradicted by the empirical evidence of pillar stability. However, an additional analysis, which is beyond the scope of this project, could provide better understanding of the pillar strength and post-peak behaviour as functions of time-dependent strength degradation, and lower uncertainty in the prediction of pillar response to the largest glacial loads.

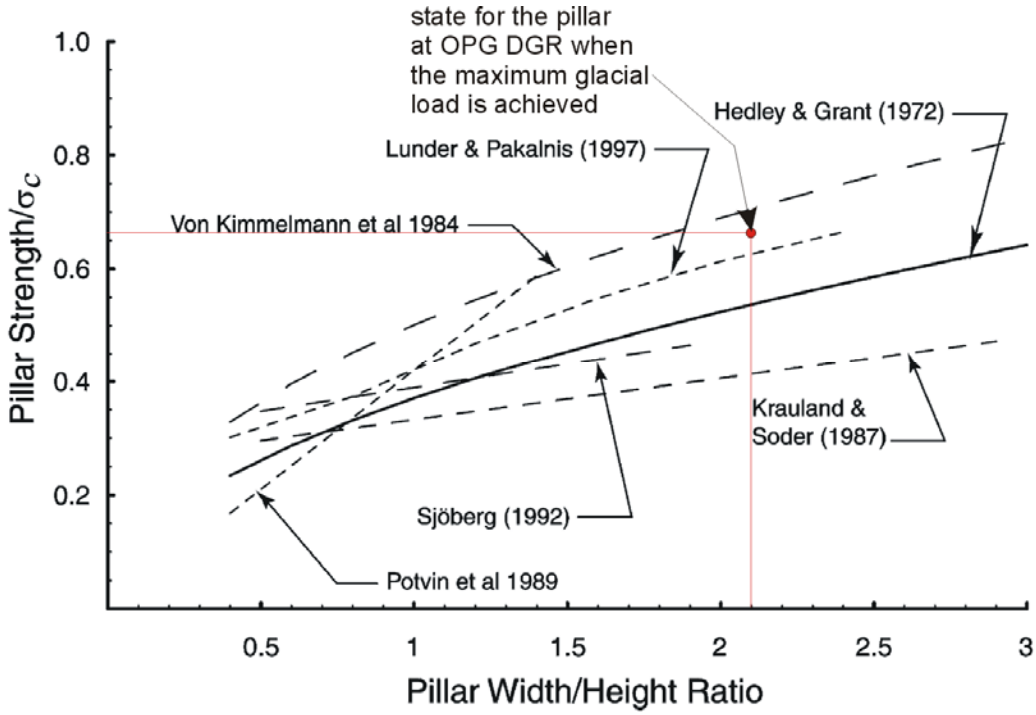

Figure 42. Comparison of empirical pillar strength relations (taken from Figure 2 from Martin and Maybee, 2000) with the pillar stresses when the maximum ice load is achieved

5. CONCLUSION

A preliminary review has been undertaken to investigate the effects of time-dependent strength degradation, gas pressure, seismic and glacial loadings on cavern stability at the OPG DGR using the numerical code UDEC. The analysis was based on the mechanical properties determined from laboratory testing of samples retrieved from the Phase I deep exploratory boreholes, DGR1 and DGR2.

The following are conservative assumptions used in the present analysis.

- DGR cavern is considered to be unsupported with no backfilling.
- All waste packages are excluded from the analysis.
- Data from static fatigue tests of Lac du Bonnet granite (with relatively fast strength decay) were adopted for the long-term strength degradation prediction of the Cobourg limestone.
- No minimum threshold was set for the long-term Cobourg limestone strength. Thus, the rock strength will eventually reduce to zero with time.
- Arbitrary bedding planes of 1 m spacing are assumed in Cobourg limestone, intersected by the tunnel excavation.
- The vertical component of seismic ground motion is assumed to have the same intensity as horizontal components. Data for eastern North America indicate that the intensity of the vertical component of ground motion is 2/3 of the intensity of the horizontal component.
- Only 0.3% of the critical damping was used in the dynamic simulations of seismic ground shaking. Typical material damping in rocks is in the range between 2% and 5%.

Using the Voronoi block model to simulate the micro-cracking and time-dependent behaviour of the rocks, an analysis was undertaken to examine the strength degradation in combination with the influence of gas pressure, seismic and glacial loading on the long-term stability of the DGR cavern. The preliminary long-term stability analysis undertaken in the present study is limited, but it provides an overall assessment of the effects of the considered loading scenarios within a 100,000 year time frame. The conclusions drawn from the analysis are summarized below.

- The results indicate, in the most conservative assumption based on the Lac du Bonnet static fatigue data and the zero long-term strength of Cobourg limestone, that damage due to time dependent strength degradation propagates, at most, to 6 m above the cavern crown, while the greatest extent of damage in the walls is about 4 m. Under static conditions, the damage results in rockfall and breakouts, at most 2.5 m from the cavern boundary.
- Sensitivity of model predictions to the assumption of long-term rock strength was investigated by assuming the long-term strength of Cobourg limestone to be 0.4 UCS. The extent of damage is reduced considerably in the crown and the floor (3.5 m from the cavern crown, with only a 0.5 m thick slab resulting in rockfall), and is almost completely absent in the cavern walls.

- If the Yucca Mountain tuff static-fatigue data are adopted in the analysis, the result shows only very limited damage in the crown and floor, with no damage in the walls and no rockfall at all.

- A further sensitivity analysis was performed to illustrate the effects of various bedding plane strengths on the characteristics of the rock mass. The stable cavern outline and rock mass damage were found to be insensitive to the variation of bedding strength.

- The cavern stability and containment of gas are analyzed for three selected gas pressure histories for a timeframe of 100,000 years. The Cobourg limestone was modelled as a continuum Mohr-Coulomb material intersected by bedding planes that were included explicitly in the analysis. Gas pressure inside the cavern, and gas and water pressures in surrounding rock, increase the extent of damage in the Cobourg limestone, but not drastically compared to the time-dependent strength degradation under dry conditions. The preferential direction of hydrofracturing will be horizontal, along bedding planes. Although horizontal fracture propagation along the bedding partings up to 16 m behind the cavern walls is expected, the gas, in all analyzed cases, will not generate hydrofractures that can result in its release into biosphere.

- The effect of the two seismic event scenarios, which match the target UHS at a 10^{-5} annual probability (**M**5.5 at a 15 km distance matches the UHS below 2 Hz; **M**7 at a 50 km distance matches the UHS above 2 Hz), on the stability of caverns at OPG DGR is analyzed numerically. Because it was expected that the response of the excavation would depend on the magnitude and extent of damage of the surrounding rock mass, the analysis was carried out for two different initial states when the model is subjected to dynamic loading: 1) immediately after cavern excavation, and 2) 100,000 years after excavation, which is the final state of time-dependent strength degradation considered. Those two states provided bounding conditions in terms of the extent of damage in the rock mass.

- The analyses have shown that the response of the excavations to two different seismic events is almost identical. The considered seismic ground motions do not produce any additional damage or rockfall if they occur immediately after excavation. Such a result is in agreement with empirical observations (Dowding and Rosen, 1978) that no damage is observed in the tunnels in which the PGV is less than 20 cm/s. For both event scenarios, the PGV is less than 10 cm/s. However, after damage due to time-dependent strength degradation has accumulated in the surrounding rock mass, a possible seismic event would shake down most of the damaged rock mass from the cavern crown. For the analyzed conditions, the predicted breakout extends approximately 5.5 m above the cavern crown.

- The effect of glacial loads on cavern stability was analyzed by simulating the history of vertical stress with a maximum pressure of 29.7 MPa (which could have occurred due to ice sheet load during the last glacial event). The motion of ice cover over the ground surface also will cause some shearing. However, at this stage of the project, glacially induced shear stresses were not considered. The entire load cycle was simulated, starting from zero ice pressure, to the maximum ice pressure, and back to zero ice pressure. The analysis indicates that the pillar between the caverns remains stable, although the glacial load causes fracturing throughout the pillar width. Sufficient confining stresses mobilize the frictional strength of the pillar core, which carries significant stresses despite being fractured.

- The empirical pillar-strength curves indicate that for the maximum glacial pressures, the average pillar stress is in the failure region of some of the curves. Because there are relatively few cases of pillar failure for width-to-height ratios greater than two (i.e., the empirical curves basically are extrapolated in the range $w/h > 2$), the empirical curves probably underestimate the strength of the squat pillars, which generally exhibit continuously hardening behaviour. Thus, the empirical data do not contradict numerical results, which indicate that the pillar will remain stable throughout the glacial cycle. Further numerical modelling is warranted to determine the pillar behaviour under the condition of multiple glacial loading cycles.

6. REFERENCES

Atkinson, G.M. (2007) Earthquake Time Histories for Bruce, Ontario long-term waste disposal facilities, Technical memorandum prepared for Gartner Lee and Ontario Power Generation

Avis, J., N. Calder, F. King, A. Paulley, G. Towler and M. Xie (2007) Postclosure Safety Assessment (V0): Normal Evolution Scenario Gas Analyses. Quintessa Report No.: QRS-1334A-TR6.

Avis, J. (2007) Excel spreadsheet file "RepositoryGasPressures_R0C.xls".

BSC (2004a) Drift Degradation Analysis. Yucca Mountain Project Report ANL-EBS-MD-000027 REV 03. Las Vegas, Nevada: Bechtel SAIC Company.

BSC (2004b) Development of Earthquake Ground Motion Input for Preclosure Seismic Design and Postclosure Performance Assessment of a Geologic Repository at Yucca Mountain, NV, Yucca Mountain Project Report MDL-MGR-GS-000003 REV 01. Las Vegas, Nevada: Bechtel SAIC Company.

Damjanac, B., M. Board, M. Lin, D. Kicker and J. Leem (2007) Mechanical degradation of emplacement drifts at Yucca Mountain—A modeling case study. Part II: Lithophysal rock, *Int. J. of Rock Mech. & Min. Sci.*, 44, 368-399.

Dowding, C.H. and A. Rozen (1978) Damage to rock tunnels from earthquake shaking. American Society of Civil Engineers, *J. Geotech. Eng. Div*. Vol. 104(2), 175-191.

Hatch (2007) OPG's Deep Geologic Repository for Low and Intermediate Level Waste, Conceptual Design Study (draft)

Hoek, E. and E.T. Brown (1980) *Underground Excavations in Rock*. The Institution of Mining and Metallurgy, London.

Idriss, I.M. and J.I. Sun (1992) User's Manual for SHAKE91. Berkeley: University of California, Davis, Department of Civil & Environmental Engineering, California Center for Geomechanical Modeling.

Intera (2006) Geoscientific Site Characterization Plan, OPG's Deep Geologic Repository for Low and Intermediate Level Waste, Report INTERA 05-220-1, OPG 00216-REP-03902-00002-R00, April, 2006.

Intera (2007) Laboratory Geomechanical Strength Testing of DGR-1 & DGR-2 Core, Technical Memorandum TM-07-03R01. CANMET Mining and Mineral Sciences Laboratories, Natural Resources Canada.

Itasca Consulting Canada, Inc. (2007) Bedrock Formations in DGR-1 and DGR-2, DGR Site Characterization Technical Memorandum, TM-07-05, dated November 8, 2007

Itasca Consulting Group, Inc. (2005) FLAC (Fast Lagrangian Analysis of Continua), Version 5.0.

Itasca Consulting Group, Inc. (1999) PFC2D (Particle Flow Code in 2 Dimensions), Version 2.0.

Itasca Consulting Group, Inc. (2004) UDEC (Universal Distinct Element Code) Version 4.0.

Jaeger, J.C. and N.G.W. Cook (1979) *Fundamentals of Rock Mechanics*. 3rd Edition. New York, New York: Chapman and Hall.

Lau, J.S.O., B. Gorski, B. Conlon and T. Anderson (2000) Long-term Loading Tests on Saturated Granite and Granodiorite. Report No. 06819-REP-01300-10016 R00. Toronto, Ontario, Canada: Ontario Power Generation, Nuclear Waste Management Division.

Martin, C.D. and W.G. Maybee (2000) The strength of hard-rock pillars. *Int. J. of Rock Mech. & Min. Sci.,* 37, 1239-1246.

Martin, R.J., J.S. Noel, P.J. Boyd and R.H. Price (1997) Creep and Static Fatigue of Welded Tuff from Yucca Mountain, Nevada. *Int. J. of Rock Mech. & Min. Sci.,* 34, (3-4), Paper No. 190.

McCreath, D. (2007) Personal Communications.

Peltier, W.R. (2008) Long Term Climate Change Study. Company Report Number OPG 00216-REP-01300-0004-R01. Department of Physics, University of Toronto.

RocScience (2004) RocLab, Version 1.0.

Schmidtke, R.H. and Lajtai, E.Z. (1985) The Long-Term Strength of Lac du Bonnet Granite. *Int. J. of Rock Mech. & Min. Sci.*, 22, (6), 461-465